A COMPACT PARALLEL-PLANE PERPENDICULAR-CURRENT FEED FOR A MODIFIED EQUIANGULAR SPIRAL ANTENNA AND RELATED CIRCUITS

A Dissertation

by

TRAVIS WAYNE EUBANKS

Submitted to the Office of Graduate Studies of
Texas A&M University
in partial fulfillment of the requirements for the degree of

DOCTOR OF PHILOSOPHY

May 2010

Major Subject: Electrical Engineering

A COMPACT PARALLEL-PLANE PERPENDICULAR-CURRENT FEED FOR A MODIFIED EQUIANGULAR SPIRAL ANTENNA AND RELATED CIRCUITS

A Dissertation

by

TRAVIS WAYNE EUBANKS

Submitted to the Office of Graduate Studies of
Texas A&M University
in partial fulfillment of the requirements for the degree of

DOCTOR OF PHILOSOPHY

Approved by:

Chair of Committee,	Kai Chang
Committee Members,	Robert Nevels
	Laszlo Kish
	Raytcho Lazarov
Head of Department,	Costas Georghiades

May 2010

Major Subject: Electrical Engineering

ABSTRACT

A Compact Parallel-plane Perpendicular-current
Feed for a Modified Equiangular Spiral Antenna
and Related Circuits. (May 2010)
Travis Wayne Eubanks, B.S., Texas A&M University
Chair of Advisory Committee: Dr. Kai Chang

This work describes the design and measurement of a compact bidirectional ultra-wideband (UWB) modified equiangular spiral antenna with an integrated feed internally matched to a 50-Ohm microstrip transmission line. A UWB transition from microstrip to double-sided parallel-strip line (DSPSL) soldered to a short (1.14 mm) twin-line transmission line feeds the spiral. The currents on the feed travel in a direction approximately perpendicular to the direction of the currents on the spiral at the points where the feed passes the spiral in close proximity (0.57 mm). Holes were etched from the metal arms of the spiral to reduce the impedance mismatch caused by coupling between the transmission line feed and the spiral.

This work also describes a low-loss back-to-back transition from coaxial line to DSPSL, an in-phase connectorized 3 dB DSPSL power divider made using three of those transitions, a 2:1 in-phase DSPSL power divider, a 3:1 in-phase DSPSL power divider, a radial dipole fed by DSPSL, an array of those dipoles utilizing the various power dividers, and a UWB circular monopole antenna fed by DSPSL. Measured and simulated results show good agreement for the designed antennas and circuits.

To my fiancée, Amanda Marie Stebbins

ACKNOWLEDGMENTS

Thank you, Mr. Li, for your ever-present willingness to help. You contributed greatly to the initial design and fabrication of the compact spiral. Dr. Nevels, your input on the perpendicular-current idea tremendously helped me to solidify my thoughts on the PPPC-fed spiral. Thank you, Dr. Chang, for your continual advice and suggestions for improvements on my research ideas. Dad and Mom, you were always available for me when I needed your encouragement, and you loved me unconditionally even when my work overwhelmed me. Clint, you gave me a great role model to follow with your own life's example. Thank you, Amanda, for all the motivation you gave me to wake up early and for waiting patiently for me while you worked in Australia. Jesus, you were with me when the lab was lonely, and you helped me to create new research ideas and work solutions quickly.

TABLE OF CONTENTS

CHAPTER Page

I INTRODUCTION 1

A. Parallel-plane Perpendicular-current Feed 3
1. Motivation for the PPPC Feed 4
2. Connection Between the Spiral and Feed 8
B. Redesign of the Microstrip-to-DSPSL Transition 13
C. Motivation for a UWB DSPSL Power Divider 16
D. UWB DSPSL Unequal Power Dividers 18
E. Motivation for the DSPSL-fed Radial Dipole Antenna . . . 19
F. DSPSL-fed Radial Dipole Antenna Array 21
G. Motivation for the UWB DSPSL-fed Circular Monopole Antenna 23

II DESIGN* 25

A. Spiral Antenna Design 25
1. General Spiral Equations 26
2. Parallel-plane Considerations 28
3. Perpendicular Currents 31
B. Parallel-strip Line Feed Design 33
1. Contributions of the Theory of Small Reflections . . . 33
2. Calculating the Reflection Coefficient 36
C. Coaxial-to-DSPSL Transition Design 39
D. UWB DSPSL Equal Power Divider Design 43
E. UWB DSPSL Unequal Power Divider Design 46
F. DSPSL-fed Dipole Antennas 50
1. Radial Dipole Antenna 50
2. Bowtie Antenna 52
3. Slotted Radial Dipole Antenna 53
4. Tri-circularly Tapered Dipole Antenna 55
5. VSWR of The Designed Dipoles 56
6. Radiation Pattern of the Designed Dipoles 57
G. DSPSL-fed Radial Dipole Array Design 59
1. Array Factor 61
2. Various Power Weighting Schemes 62

CHAPTER Page

H. UWB DSPSL-fed Circular Monopole Antenna Design . . . 65

III RESULTS 67

A. Final Spiral Antenna Performance 68
1. Impedance Bandwidth 71
2. Radiation Bandwidth 73
3. Signal Distortion 77
B. DSPSL-fed Radial Dipole Array Performance 79
1. Radiation Pattern Versus Frequency 80
2. Weighting Effects on the Impedance Bandwidth 84
3. Weighting Effects on the Side-lobe Level 85
4. Weighting Effects on the Radiation Efficiency 87
C. UWB DSPSL-fed Circular Monopole Antenna Performance 88
1. Impedance Bandwidth 89
2. Radiation Pattern 90
3. Efficiency 91

IV COMPARATIVE ANALYSIS 94

A. Spiral Antenna Comparisons 94
1. Coaxially-fed Equiangular Slot Spiral 94
2. Co-planar Strip Line-fed Equiangular Spiral 98
3. Slot Line-fed Archimedean Spiral 100
4. Coaxially-fed Monofilar Archimedean Spiral 103
5. Tapered Microstrip Line-fed Archimedean Spiral . . . 105
B. Coaxial-to-DSPSL Transition Comparisons 108
1. Microstrip-to-DSPSL Transition 108
2. Microstrip-to-co-planar Strip Line Transition 111
C. UWB DSPSL Power Divider Comparisons 113
1. UWB Microstrip Line Equal Power Wilkinson Divider 114
2. Microstrip Line Unequal Power Wilkinson Divider . . 116
D. Radial Dipole Antenna Comparisons 117
1. Microstrip-to-co-planar Strip Line-fed Circular Dipole 118
2. UWB Microstrip-to-co-planar Strip Line-fed Dipole . . 120
E. Radial Dipole Antenna Array Comparisons 121
1. Linear Four-element Microstrip-to-DSPSL Dipole Array 122
2. DSPSL-fed Planar Yagi-Uda Array 123
3. Dual-polarized Dipole Array 126
F. Circular Monopole Antenna Comparisons 128

CHAPTER Page

1. Co-planar Waveguide-fed Circular Monopole 129
2. Coaxial Line-fed Circular Monopole Disk 131
3. Microstrip Line-fed Circular Monopole Array 132

V SUMMARY AND CONCLUSIONS 135

A. Summary 135
B. Conclusions 135

REFERENCES 138

APPENDIX A 144

VITA 155

LIST OF TABLES

TABLE		Page
I	Unequal Power Divider Parameters	48
II	Radial Dipole Parameters	51
III	Bowtie Parameters	53
IV	Slotted Radial Dipole Parameters	54
V	Tri-circularly-tapered Dipole Parameters	56
VI	No Weight Power Distribution	63
VII	Half Power Distribution	63
VIII	Binomial Power Distribution	64
IX	Mixed Power Distribution	64
X	Spiral Antenna's Maximum Effective Aperture Area	72
XI	Asymmetric and Symmetric Spiral Fidelity Factor Comparison	79
XII	Weighting Effects on the Radial Dipole Array's Side-lobe Level	84
XIII	Gain and Efficiency for the Radial Dipole Array	87
XIV	DSPSL-fed Circular Monopole Antenna's Radiation Efficiency	92

LIST OF FIGURES

FIGURE		Page
1	PPPC feed overhead view.	4
2	Middle spiral antenna layer.	5
3	Bottom spiral antenna layer.	6
4	Top spiral antenna layer.	7
5	Tapered parallel-strip line feed for the modified spiral.	8
6	Twin-line connection between the spiral's substrates.	9
7	Straightening and shortening the spiral's twin-line.	10
8	Twin-line holes in the center of the spiral.	11
9	Complete spiral without holes.	12
10	Complete spiral with holes.	13
11	Top of the coaxial-to-DSPSL back-to-back transition.	14
12	Bottom of the coaxial-to-DSPSL back-to-back transition.	15
13	Top of the UWB DSPSL 3 dB power divider.	16
14	Bottom of the UWB DSPSL 3 dB power divider.	17
15	Top and bottom metal layers of the DSPSL-fed radial dipole antenna, shown from left to right.	20
16	Bottom of the 4x4 DSPSL-fed radial dipole array with no power weighting.	22
17	DSPSL-fed circular monopole antenna's (a) bottom and (b) top sides.	24
18	The four spiral arm boundary curves.	27

FIGURE Page

19 Various spiral arm widths minus etching hole diameters (remaining metal widths) at specific angles produce varying return losses over the 4-7 GHz frequency range. The maximum metal width occurs with no etching hole present. 29

20 The surface currents on a rectangular spiral are forced to travel on the tangent of the circle as they approach the crossing between the spiral and the feed. The tangent to the circle is perpendicular to the feed at the feed's center. 30

21 The top and bottom surface currents on the equiangular spiral sum vectorially to produce a net current perpendicular to the feed's current at the point of crossing between the spiral and the feed. 32

22 The taper $w(y)$ used to create the parallel-plane perpendicular-current feed. 34

23 Characteristic impedance of the parallel strip-line versus distance in the y-direction. 36

24 Magnitude of the reflection coefficient for the perfectly-matched linearly-tapered parallel-strip line. 37

25 Coaxial-to-DSPSL transition top. 38

26 Coaxial-to-DSPSL transition bottom. 39

27 Coaxial-to-DSPSL transition dimensions. 40

28 Throughput and reflected power levels of the coaxial-to-DSPSL transition. 41

29 UWB DSPSL power divider with three coaxial-to-DSPSL transitions. 44

30 Throughput and reflected power levels of the 3 dB in-phase UWB DSPSL power divider. 45

31 Unequal power divider for the 2:1 and 3:1 configurations. 47

32 Through and reflected power levels for the 2:1 and 3:1 power dividers. 49

FIGURE Page

33 DSPSL-fed radial dipole antenna. 51

34 DSPSL-fed bowtie antenna. 52

35 DSPSL-fed slotted radial dipole antenna. 53

36 DSPSL-fed tri-circularly-tapered dipole antenna. 55

37 VSWRs of the various DSPSL-fed dipole antennas. 57

38 Radiated E_θ and E_ϕ versus θ angle for the designed dipoles in the (a) x-z and (b) y-z planes. 58

39 Radiated $|E|$ fields for the designed dipoles in the (a) x-y, (b) x-z, and (c) y-z planes. 59

40 The 4x4 array of radial dipole antennas with unequal and symmetrical power weighting. 60

41 DSPSL-fed circular monopole with dielectric hidden. 65

42 Real and imaginary impedance versus frequency for the antenna (a) without etching holes and (b) with etching holes. 68

43 VSWR plots for spiral antennas with and without etching holes. . . . 69

44 Measured and simulated radiation efficiency of the antenna with etching holes over the 3-12 GHz range. 70

45 Radiation patterns for the spiral antenna with measured gain shown in dBi. (a) 3 GHz and $\phi = 0\,^\circ$. (b) 3 GHz and $\phi = 90\,^\circ$. (c) 6 GHz and $\phi = 0\,^\circ$. (d) 6 GHz and $\phi = 90\,^\circ$. 74

46 Radiation patterns for the spiral antenna with measured gain shown in dBi. (a) 9 GHz and $\phi = 0\,^\circ$. (b) 9 GHz and $\phi = 90\,^\circ$. (c) 12 GHz and $\phi = 0\,^\circ$. (d) 12 GHz and $\phi = 90\,^\circ$. 75

47 The axial ratio for the spiral with etching holes. This antenna exhibits elliptical polarization from 3-12 GHz. 76

FIGURE Page

48 The transmitted signal for both spirals (Trans.), received signal from the asymmetrical spiral (Asym.), and received signal from the symmetrical spiral (Sym.). 78

49 Measured and simulated $|E|$ field versus θ angle in the $\phi = 0°$ plane for the half-power distribution at (a) 2.55 GHz, (b) 2.65 GHz, (c) 2.75 GHz, (d) 2.85 GHz, (e) 2.95 GHz, (f) 3.05 GHz, (g) 3.15 GHz, (h) 3.25 GHz, (i) 3.35 GHz, (j) 3.45 GHz. 81

50 Measured and simulated $|E|$ field versus θ angle for in the $\phi = 90°$ plane for the half-power distribution at (a) 2.55 GHz, (b) 2.65 GHz, (c) 2.75 GHz, (d) 2.85 GHz, (e) 2.95 GHz, (f) 3.05 GHz, (g) 3.15 GHz, (h) 3.25 GHz, (i) 3.35 GHz, (j) 3.45 GHz. 82

51 VSWRs of the 4x4 radial dipole array for four different power weighting schemes. 83

52 Radiated $|E_\theta|$ patterns for the various weighting schemes at 3.05 GHz in the $\phi = 0°$ plane for varying degrees of θ. 85

53 Radiated $|E_\phi|$ patterns for the various weighting schemes at 3.05 GHz in the $\phi = 90°$ plane for varying degrees of θ. 86

54 Measured and simulated VSWR of the DSPSL-fed circular monopole antenna. 88

55 Measured and simulated radiation patterns versus θ angle for E_θ and E_ϕ at (a) $\phi = 0°$ and (b) $\phi = 90°$ at 5.0 GHz. 90

56 Measured and simulated radiation patterns in E_θ and E_ϕ versus θ angle for (a) $\phi = 90°$ and versus ϕ angle for (b) $\theta = 90°$ at 10.0 GHz. 91

57 Dyson's slot spiral antenna fed by three coaxial lines of differing widths. 95

58 The VSWR of Dyson's slot spiral from 0.4 to 10 GHz. 96

59 Radiation patterns in E_θ and E_ϕ for Dyson's slot spiral from 2.8 to 12 GHz. 97

60 Tu's spiral antenna fed perpendicularly by co-planar strip line. 98

FIGURE Page

61 Negative return loss for Tu's spiral. 99

62 Radiation patterns in E_θ and E_ϕ for Tu's spiral at $\phi = 0°$ and $\phi = 90°$. 100

63 Wu's cavity backed side-fed spiral antenna. 101

64 Negative return loss for Wu's spiral. 102

65 Nakano's monofilar perpendicularly-fed spiral antenna. 103

66 Real and imaginary impedance for Nakano's spiral near its center frequency. 104

67 Right-hand circularly polarized (E_R) and left-hand circularly polarized (E_L) radiation patterns for Nakano's spiral at f_0. 105

68 Top and bottom of Huff's planar spiral antenna and the spiral's VSWR.106

69 Kim's back-to-back microstrip-to-DSPSL transition. 108

70 Transmitted and reflected power levels for Kim's back-to-back microstrip-to-DSPSL transition. 109

71 Tu's microstrip-to-co-planar strip line transition. 112

72 Transmitted and reflected power levels for Tu's back-to-back microstrip-to-co-planar strip line transition. 113

73 Wong's microstrip line-fed UWB equal power Wilkinson divider. . . . 114

74 Transmitted and reflected power levels for Wong's Wilkinson divider. 115

75 Lim's microstrip line-fed unequal power Wilkinson divider. 116

76 Transmitted and reflected power levels for Lim's Wilkinson divider. . 117

77 Karlsson's microstrip-to-strip line-fed circular dipole. 118

78 Measured and simulated VSWR of Karlsson's circular dipole. 119

79 Low's microstrip-to-strip line-fed dipole. 120

80 Measured and simulated S_{11} of Low's dipole. 121

FIGURE Page

81 Evtioushkine's linear four-element microstrip-to-DSPSL dipole array. 122

82 Merli's DSPSL-fed planar Yagi-Uda array. 123

83 Measured and simulated reflected power levels for Merli's Yagi-Uda array. 124

84 Co- and cross-polarization radiation measurements for Merli's Yagi-Uda array at 10.3 GHz. 125

85 Hees' dual-polarized dipole array in (a) CST Microwave Studio and (b) realization. 126

86 Measured and simulated reflected power levels for Hees' array in the vertical and horizontal polarization orientations. 127

87 Measured gain of Hees' dual-polarized dipole array. 128

88 Yu's co-planar waveguide-fed circular monopole antenna. 129

89 VSWR of Yu's co-planar waveguide-fed circular monopole antenna. . 130

90 Chaw's coaxial line-fed circular monopole disk. 131

91 Reflected power levels for Chaw's circular monopole with and without the curved slot. 132

92 Ihsan's microstrip line-fed circular monopole array. 133

93 Simulated gain versus angle ϕ for Ihsan's array at 5 and 9 GHz. . . . 134

CHAPTER I

INTRODUCTION

John Dyson showed in the mid-1950's that equiangular spiral antennas have characteristics associated with infinite structures that allow the antennas to radiate bidirectionally with 98% efficiency, having 20:1 impedance and radiation bandwidths [1]. Knowing that spiral antennas exhibit such broadband behavior with high efficiency, RF engineers have since continued to create ways to feed these antennas that preserve (as much as possible) the radiation and impedance bandwidths from [1], while adapting the antennas to specific applications [2–7].

Since the planar spiral antenna with multiple arms has arm terminations closest together near the center of the spiral, some designers choose to feed the spiral from the center at a 90° angle to the spiral's surface [2, 5–7] so that the radiation from the spiral is least affected by the feed network. This three-dimensional feed usually has an absorbing or reflecting cavity behind it to support the feed line mechanically and to force the spiral to radiate unidirectionally. Two-dimensional feeds in planes parallel to the spiral feed the antenna by either connecting the feed line to the arm terminations on the perimeter of the spiral [4] or by feeding the spiral with a transmission line that follows the metal layer directly beneath the spiral to the center feed point [1, 3]. This dissertation presents a unique and novel parallel-plane perpendicular-current (PPPC) feed for a modified equiangular spiral antenna. The PPPC feed is two-dimensional and compact.

In addition, this work describes a new low-loss transition from coaxial line to DSPSL, which is useful for feeding the modified spiral antenna. A low-loss in-phase

---

The journal model is *IEEE Transactions on Antennas and Propagation.*

3 dB power divider was built using three of these transitions connected to a tapered DSPSL T-junction in order to demonstrate that an array of UWB elements could be created using such a DSPSL power division feed network. In the case of such a network, the power divider would have lower loss than what was measured because the measured power divider includes the losses associated with the transitions from DSPSL to the SMA coaxial connectors.

The 3 dB in-phase DSPSL power divider was modified to create 2:1 and 3:1 power dividers to be used in an antenna array with unequal power weighting for reduced side-lobe levels. Then a radial dipole antenna element was designed to be fed by a 4x4 corporate-H array, and the array was built and measured. The side-lobe level (SLL) of the array was optimized using the designed power dividers such that the array had minimal SLLs in both the x-z and y-z planes, moderate efficiency (and gain), and minimal return loss.

Initially, the intent was to design a low-loss spiral array fed by DSPSL lines with the designed power dividers. However, it was discovered that the microstrip-to-DSPSL transition in the PPPC fed spiral affects the impedance of the spiral in a way that prevents it from being simply replaced with the lower loss transition without re-tuning the spiral's exponential constants for a UWB 2:1 VSWR impedance bandwidth. Due to the time-consuming nature of tuning the spiral's parameters for a good impedance match and the mechanical labor required to fabricate each three-layer compact spiral, the spiral array fed by DSPSL lines is left for future research.

A circular monopole antenna was designed as an alternate array element which may be equally suited for DSPSL array design using the described power dividers and low-loss coaxial-DSPSL transition. This antenna exhibits UWB impedance and radiation bandwidths, but unlike the PPPC fed spiral, it only requires two metal layers instead of three, relieving some of the mechanical burden required to create

the antenna. Since the simulation of this UWB antenna in an array also required more time than was available, the circular monopole array is also left for future research.

A. Parallel-plane Perpendicular-current Feed

This feed receives its name for two reasons. The feed lies in a plane parallel to the spiral's surface, and the currents traveling down this feed line are approximately perpendicular to the currents on the spiral's arms where the feed line passes underneath. Placing the feed in a plane parallel to the spiral minimizes the overall volume of the structure. Forcing the currents to cross each other at near perpendicular angles minimizes the interactions of fields from the spiral with fields from the transmission line. With minimized interactions between radiation and transmission line fields, the antenna radiates most efficiently with a minimal return loss.

Fig. 1 shows the three metal layers for this structure from an overhead view, which are aligned vertically (using the alignment holes in the upper corners and thin rectangular border for guidance) prior to final assembly. In Fig. 1, the substrates between the metal layers were removed to show their alignment. The black sections of Fig. 1 (except for the cartesian coordinate reference) represent the copper metal layers of this structure.

Although inevitably the feed line will prevent radiation from the spiral in certain locations due to the proximity of the feed to the radiating areas between the spiral's arms, this antenna structure shows good radiation patterns over the UWB range. The feed line in the $\phi = 90^\circ$ direction forces the spiral's radiation to be lowest along that line. The spiral's radiation was measured along the $\phi = 0^\circ$ and $\phi = 90^\circ$ lines to show the maximal and minimal gain of the spiral.

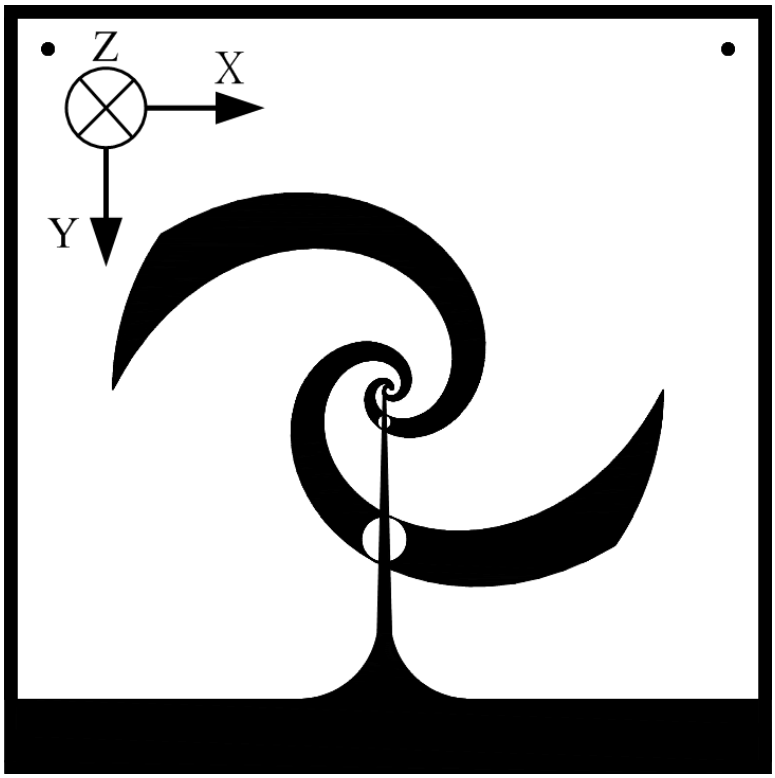

Fig. 1. PPPC feed overhead view.

1. Motivation for the PPPC Feed

Upcoming ultra-wideband (UWB) applications inspired the design of the PPPC feed. The PPPC feed satisfies the desire to have a low volume equiangular spiral with an integrated and balanced feed network. A UWB balun transforms the unbalanced microstrip line input into a balanced parallel-strip line feed for the antenna, as described in [8].

Fig. 2 shows the middle antenna layer, which consists of the tapered microstrip line (region 3 to region 2) and the parallel-strip feed line (region 2 to region 1) that

connects a microstrip input to the left spiral arm (as seen from the center of the spiral in Fig. 1). A twin-line transmission line guides the fields on this line from region 1 to the center of the spiral through vertical (negative z-direction) parallel via holes.

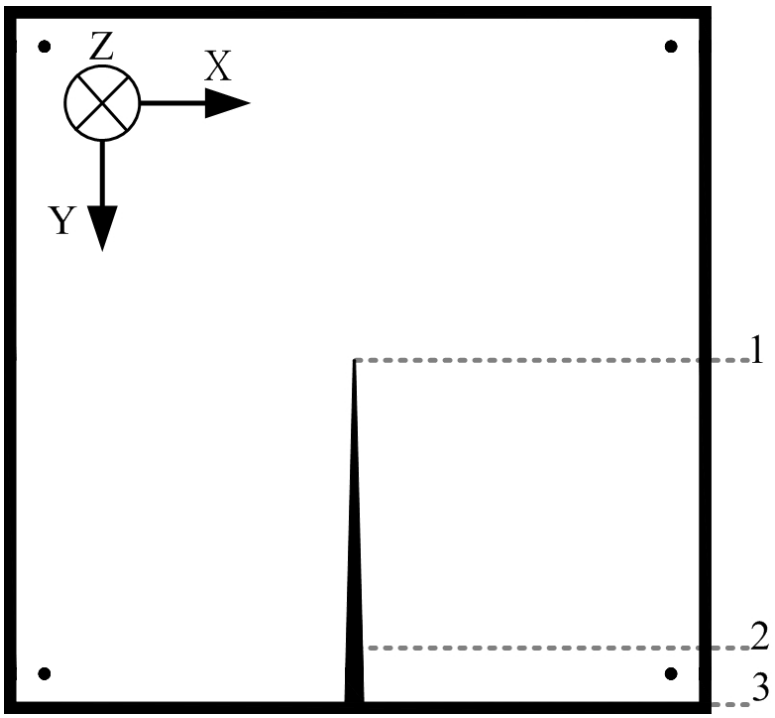

Fig. 2. Middle spiral antenna layer.

Fig. 3 shows the bottom antenna layer, which converts the microstrip ground into a parallel-strip ground through a circular taper at region 2. Region 3 to 2 is microstrip ground, and region 2 to 1 is tapered parallel-strip ground. The parallel-strip line that results from stacking the middle and bottom layers has the same taper rate for both

layers. The twin-line transmission line also connects to the bottom metal layer at region 1 to feed the right spiral arm (as seen from the center of the spiral in Fig. 1). The circular curve at region 1 on the tapered parallel-strip ground (Fig. 3) aids the twin line transmission line by positioning its connection directly beneath the right arm of the spiral. This allows the width of the twin-line transmission line to remain fixed as it connects the transmission line to the spiral arms.

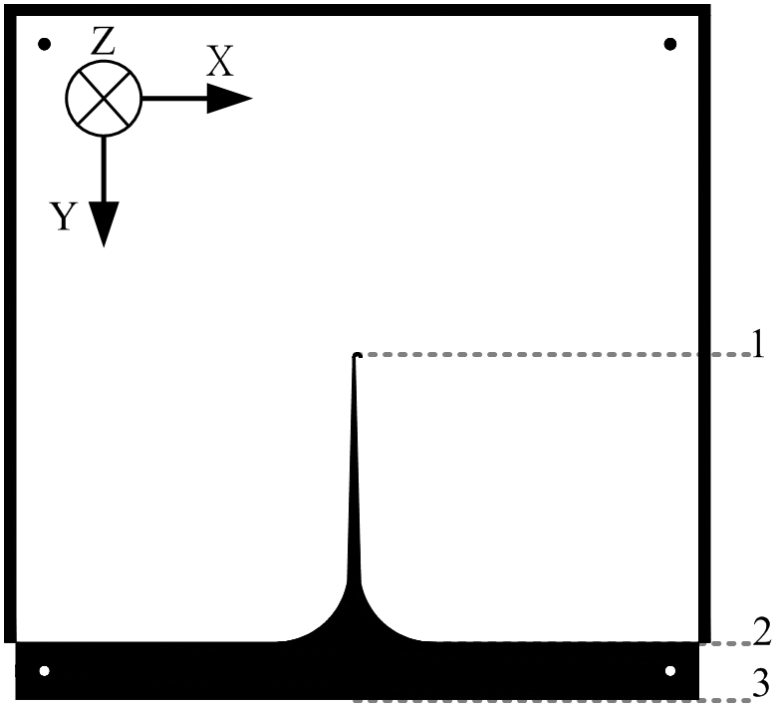

Fig. 3. Bottom spiral antenna layer.

Since the equiangular spiral can be designed to operate over the entire UWB

range (3.1-10.6 GHz) [1], this antenna may operate in the UWB range if the intermediate transmission line section is designed appropriately (region 2 to region 1 in Figs. 2-3). Fig. 4 shows the metal layer consisting of the equiangular spiral alone. Measured and simulated results show that the PPPC feed minimally affects the spiral's radiation and impedance bandwidths.

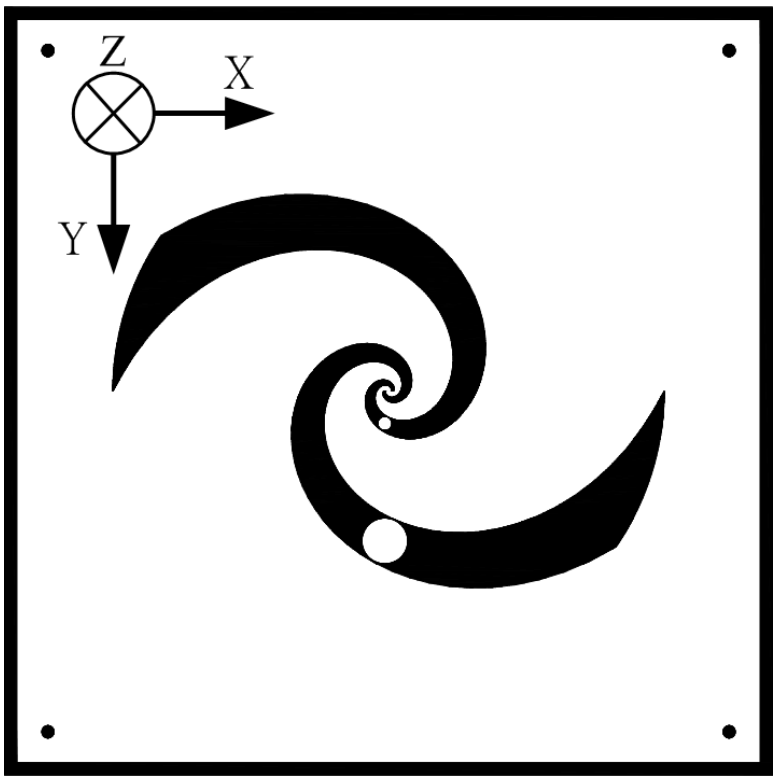

Fig. 4. Top spiral antenna layer.

2. Connection Between the Spiral and Feed

The theory of small reflections shows that a tapered transmission line can impedance match a source to a load over a broadband frequency range. Applying this concept to the parallel-strip feed allowed it to impedance match the spiral antenna to the 50 Ω microstrip input and to prepare the feed for mechanical connection to the spiral's feed points. Fig. 5 illustrates this tapered parallel-strip line.

Fig. 5. Tapered parallel-strip line feed for the modified spiral.

After the taper reduced the width of the 50 Ω line to the width of the spiral antenna's arms at region 1 in Figs. 2-3, a short (1.14 mm) twin line mechanically and electrically connected the parallel-strip feed to the spiral through vertical via-holes.

Fig. 6 shows the twin-line between the two substrates and the bottom side of the spiral's substrate.

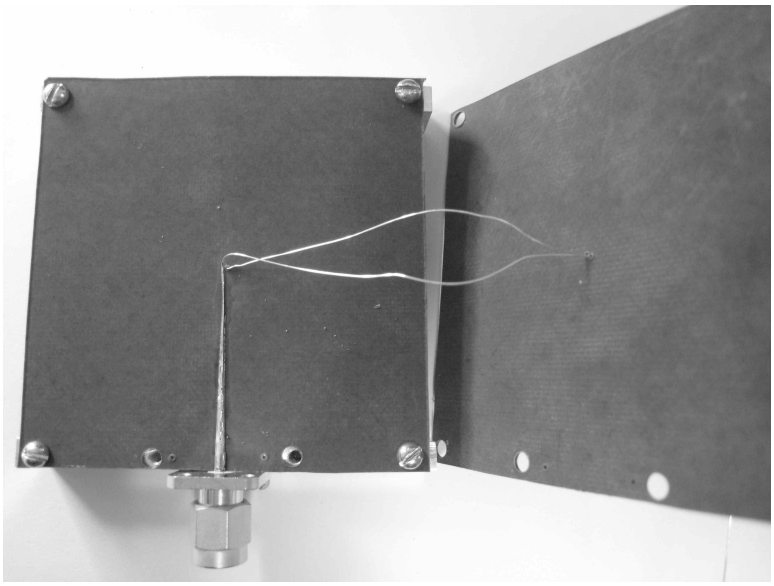

Fig. 6. Twin-line connection between the spiral's substrates.

Solder serves as both the mechanical and electrical connection of the twin-line transmission line to the parallel-strip feed and the spiral antenna. As such, the twin-line connection to the parallel-strip feed starts at the narrow end of the circular taper near region 2 in Fig. 3 and ends at the center of the spiral in Fig. 4. The short portion of the twin-line that stands alone from the parallel-strip line starts at region 1 in Figs. 2-3 and extends from the bottom of the second substrate up to the top of the substrate holding the spiral antenna, shown in Fig. 4.

Under a microscope, fine needles were used to cut holes 0.4 mm apart into the substrates at the points where the twin-line would connect the spiral directly to the parallel-strip feed. After mechanically (and electrically) connecting to the parallel-strip feed and ground to the twin-line, the twin-line passed through the small holes to connect to the spiral arms. Fig. 7 shows the straightening of the twin-line transmission line as the spiral layer and the parallel-strip line layers were pushed together.

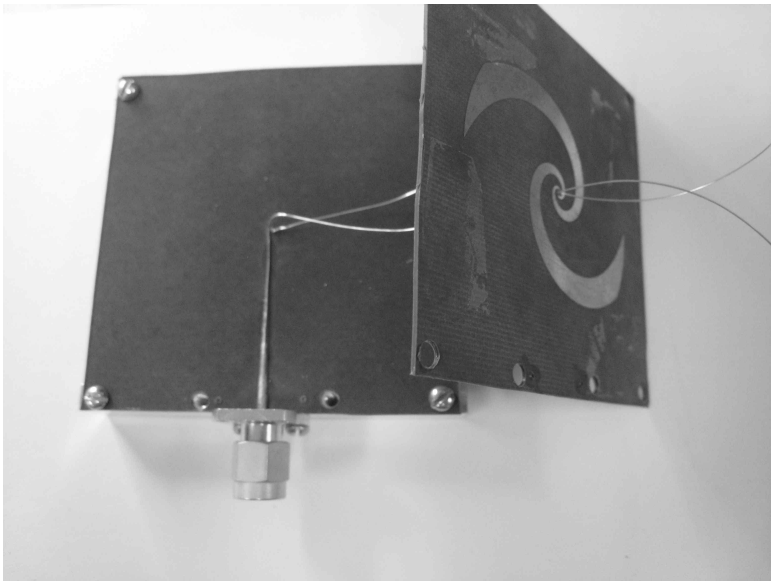

Fig. 7. Straightening and shortening the spiral's twin-line.

After the twin-line passed through these holes, the substrate holding the spiral could move flush against the substrate holding the UWB balun while straightening the twin-line between the substrates (since the twin-line passed through vertical holes

inside the substrates). These small holes are shown in Fig. 8. Once flush against the balun's substrate, the spiral and the twin-line were soldered together, and clippers were used removed the extra twin-line.

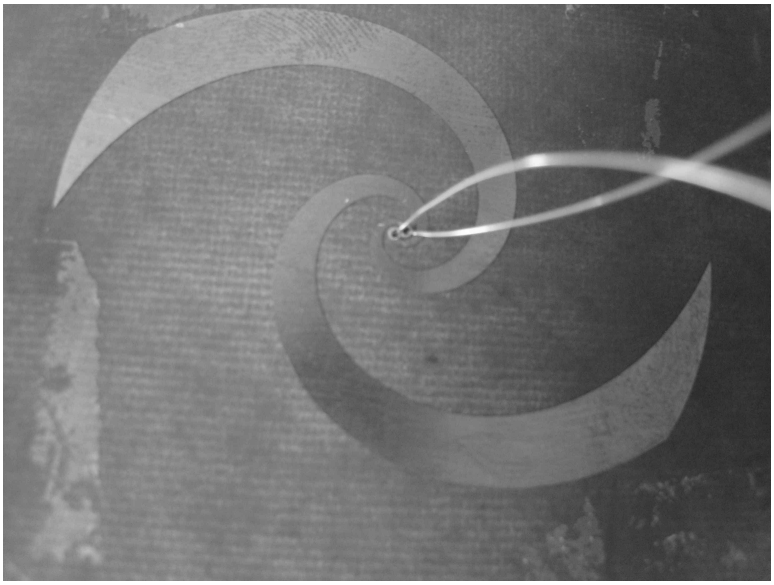

Fig. 8. Twin-line holes in the center of the spiral.

Fig. 9 shows the spiral without holes. This spiral has the same middle and bottom metallization layers as the spiral with holes. The radiation pattern of this antenna and the antenna with holes look exactly the same, but the impedance match of this antenna is slightly worse than the antenna with holes. Since the currents on this antenna are not quite perpendicular to the currents on the feed, and the fields on the feed see more interaction with the metal layer of the spiral without holes, it is

expected that the spiral without holes would have a worse return loss than the spiral with holes.

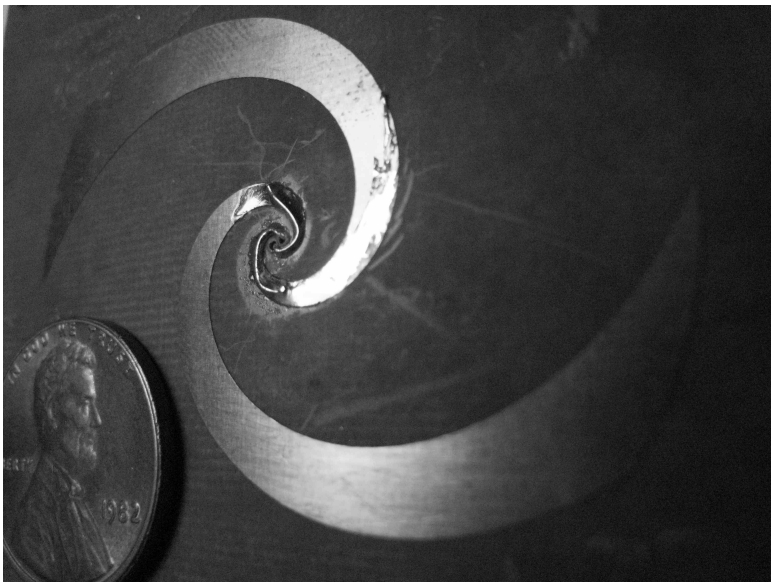

Fig. 9. Complete spiral without holes.

Fig. 10 shows the complete spiral with holes. Since the spiral with holes did actually show a better impedance match over the UWB band than the spiral without holes, the hypothesis that the holes would improve the impedance bandwidth was verified. The etching acid dissolved more copper on the spiral than was necessary, so the missing copper was replaced with 30 AWG wire near the holes.

Measured and simulated results for both antennas show good agreement overall, but the simulated and measured results for the antenna with holes showed slight

disagreement in the VSWR data. Since the loss of the antenna with holes was sufficiently low to maintain a 2:1 VSWR bandwidth in the entire UWB band, no extra efforts were made to produce better agreement between the measured and simulated VSWRs for the antenna with holes.

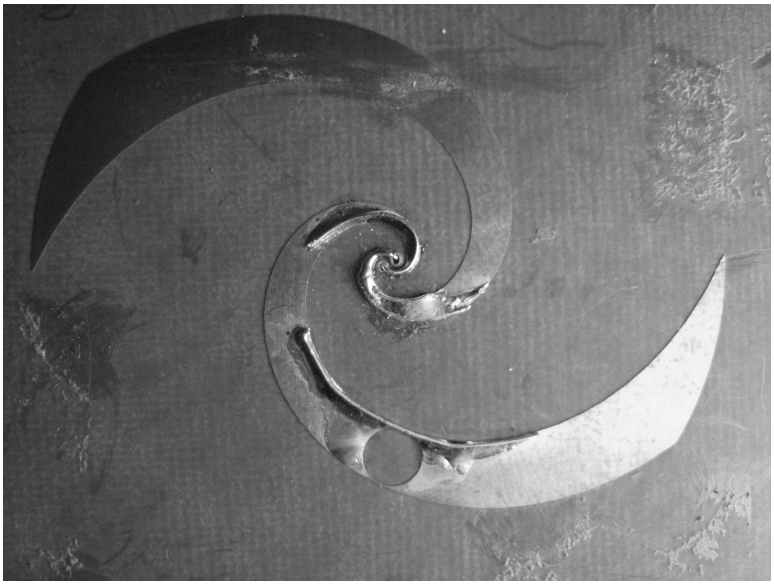

Fig. 10. Complete spiral with holes.

B. Redesign of the Microstrip-to-DSPSL Transition

The DSPSL transitions and circuits demonstrated in [8] inspired the aforementioned planar UWB antenna design. After building and measuring the designed antenna, the author decided to re-design the microstrip-to-DSPSL transition described in [8] in

order to reduce the losses associated with the transition. These losses were reduced by adding a transitory section from coaxial transmission line to microstrip line, lengthening the transition section, and increasing the radius of the circular chamfer on the ground plane.

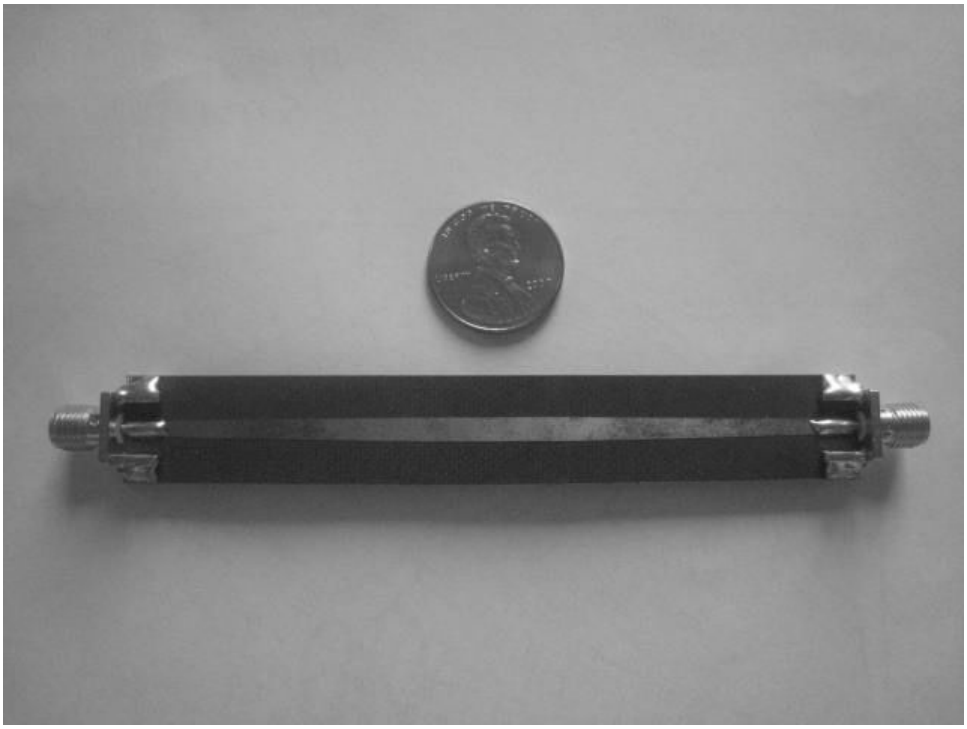

Fig. 11. Top of the coaxial-to-DSPSL back-to-back transition.

Fig. 11 shows the top of the coaxial-to-DSPSL back-to-back transition with both SMA end mount connectors attached. The top of the transition shows the coaxial center conductors soldered to the top of the quasi-microstrip line, which is then

tapered to a 50 Ω DSPSL width. The total length of the back-to-back transition is 100 mm, and the transition from coaxial-to-DSPSL is 40 mm long.

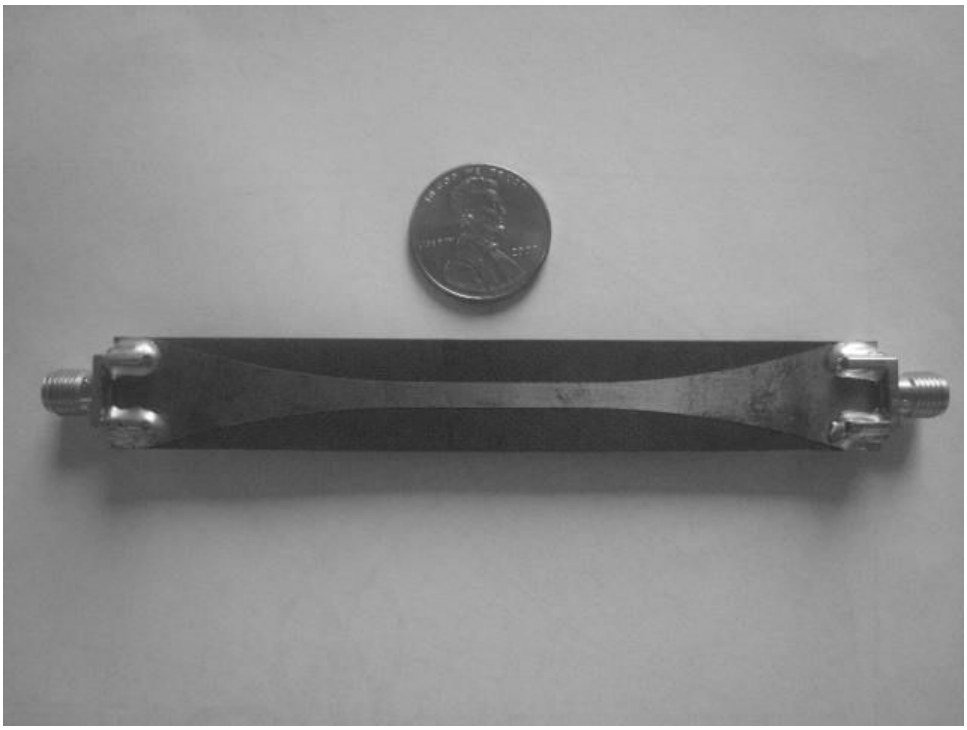

Fig. 12. Bottom of the coaxial-to-DSPSL back-to-back transition.

The bottom of the coaxial-to-DSPSL back-to-back transition is shown in Fig. 12. The bottom of the transition shows the microstrip ground near the coaxial connectors, the four solder connections from the coaxial connectors to the microstrip ground, and the DSPSL in the center of the transition. The ground is circularly tapered from microstrip to DSPSL.

C. Motivation for a UWB DSPSL Power Divider

In order to create a UWB DSPSL-fed antenna array, it is necessary to use a UWB DSPSL power divider as a base element in the feed network. The author designed a UWB DSPSL 3 dB power divider to allow the divider to directly feed the hypothetical array's antenna elements.

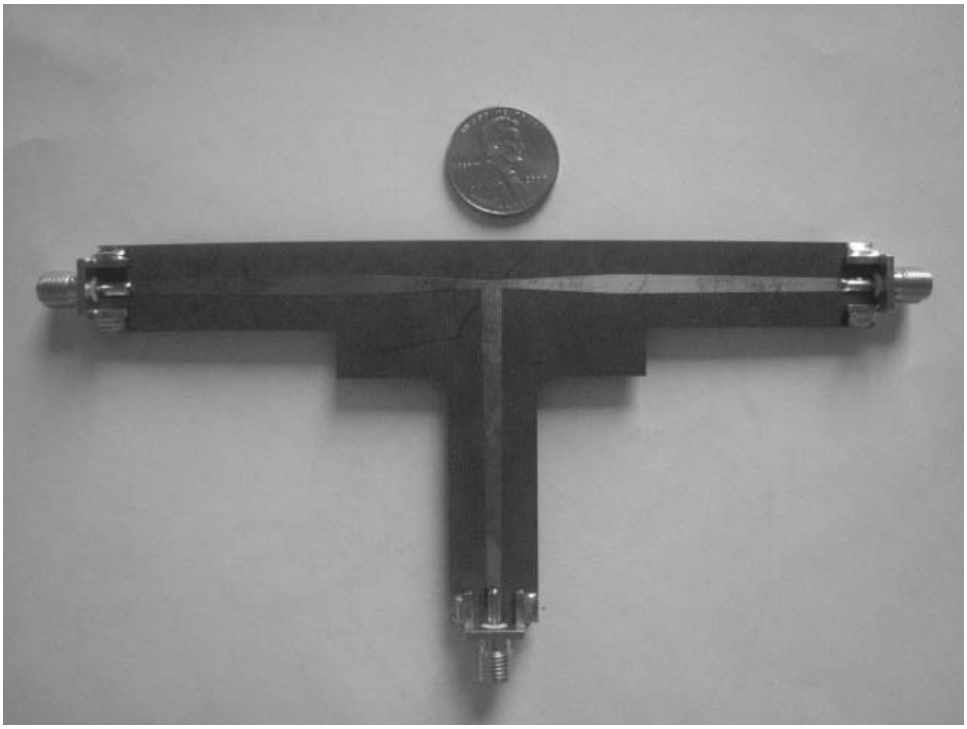

Fig. 13. Top of the UWB DSPSL 3 dB power divider.

For the sake of measurement and versatility, the author built the power divider

with the redesigned coaxial-to-DSPSL transition shown in Figs. 11-12 attached on all three ports. This configuration verifies the performance of the low-loss transition, and it allows the power divider to be quickly connected or disconnected to other circuitry.

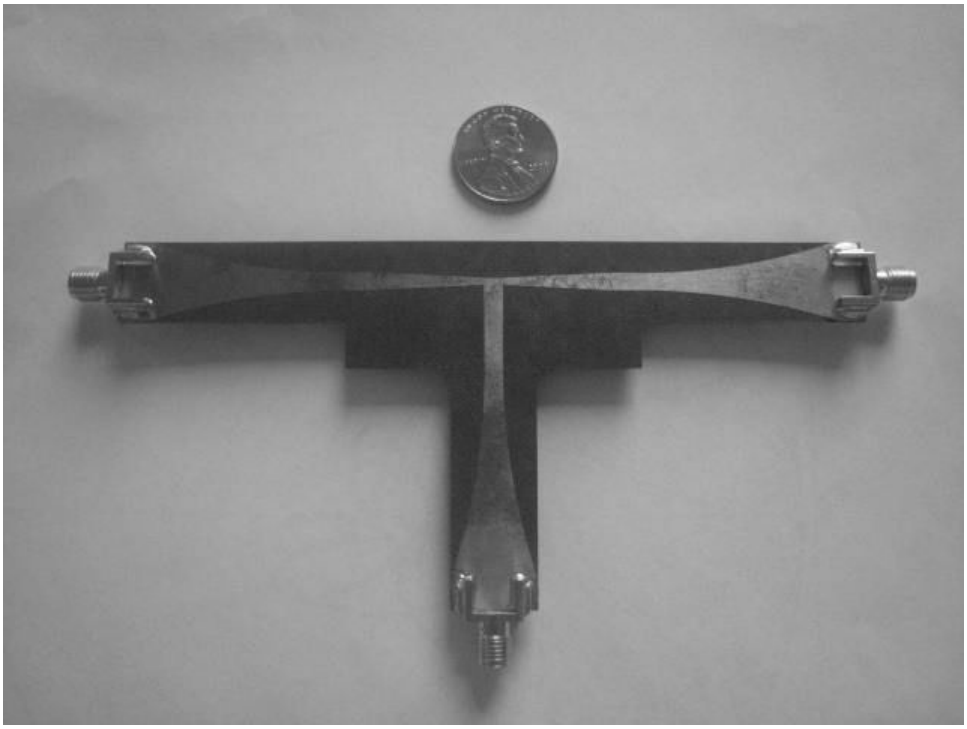

Fig. 14. Bottom of the UWB DSPSL 3 dB power divider.

The designed power divider is shown in Figs. 13-14. This power divider could easily be replicated and rotated to form an equal power weighted array of UWB antennas. Creating a steerable, unequally weighted phased array with such a divider may be possible over a broad impedance bandwidth if modifications are made to the

divider and proper phasing is chosen between the elements.

D. UWB DSPSL Unequal Power Dividers

Dolph analytically showed that the optimal relationship between side-lobe level (SLL) and beam width in a linear array occurs for a Tchebyscheff polynomial current distribution among the antenna elements [9]. He explained that this current distribution has a greater radiation efficiency, smaller current ratio, and lesser beam width than the binomial current distribution, which has a zero SLL. He also explained that the Tchebyscheff polynomial current distribution has a minimally flat SLL that can be chosen to suit a given application. The uniform current distribution has maximal gain, but its -12 dB SLL is too high for many applications [9].

In theory the SLL of an array of linearly combined antennas can be chosen by specifying the currents at the elements to create the desired array factor, but in practice the power levels of elements in that array are specified through the design of the feed network's power dividers. In order to appropriately weight an array fed by double-sided parallel-strip line (DSPSL) [8], unequal power dividers are required to minimize the SLL of the array.

Since each unequal UWB DSPSL power divider has a different set of requirements necessary to impedance match the divider to the DSPSL while maintaining the desired power ratios, only half-power and third-power UWB dividers are designed in this work. The half-power divider provides one output with half of the power provided to a second output, so it is referred to as a 2:1 divider throughout this work. Similarly, the third-power UWB divider provides one output with one-third of the power provided to a second output, so it is referred to as a 3:1 divider through this work.

These power dividers were created based on the the 3 dB UWB DSPSL divider's

design. The power ratios of the unequal DSPSL dividers were tuned by increasing the width of one output line near the center of the 3 dB divider while decreasing the width of the other output line at the center of the 3 dB divider. In this way, the divider remained matched to a 50 Ω characteristic impedance at its output ports, while the power sent to each port varied. In order to achieve a 2:1 VSWR bandwidth across the FCC defined UWB bandwidth (3.1-10.6 GHz), the width of the input line at the center of the 3 dB divider was also modified.

Instead of creating power dividers with Tchebyscheff ratios to attempt to satisfy Dolph's conditions, these power dividers were created to demonstrate their common ratios in a new setting for unequal power division. Since the power dividers determine the power at the elements instead of the element currents, the Tchebyscheff polynomial ratios do not exactly relate to the dividers' ratios anyway. By using the more common 2:1 and 3:1 ratios, binomial and half power-weighting schemes can be constructed and compared.

Dr. Berndie Strassner showed experimentally (un-documented) that he was able to achieve -30 dB SLLs in a corporate-H-fed 4x4 unidirectional microstrip patch array using half-power division between the antenna elements. Uniform, half, binomial, and a combination of the two non-uniform power-weighting schemes were applied to a 4x4 bidirectional array of DSPSL-fed elements. The SLLs of the DSPSL-fed arrays were then compared with Dr. Strassner's results for the 4x4 microstrip patch array.

E. Motivation for the DSPSL-fed Radial Dipole Antenna

Payne showed in [10] that the bandwidth and efficiency of shortened dipoles may be improved by adding radial elements to the ends of the dipoles. By shortening the length of a $\lambda/2$ dipole, that dipole may be used in a two-dimensional antenna array

with $\lambda/2$ element spacing in both directions.

The DSPSL is suitable for feeding differential antennas because the DSPSL uses two equal-width metal strips on opposing sides of a substrate. These strips can be matched simultaneously to the input impedance of a differentially-fed antenna without requiring a phase-compensating balun.

The top and bottom metal layers of the radial dipole element are shown in Fig. 15. The radial dipole has the same metal layer on its top as it does the bottom, but the metal layers are mirrored about the central DSPSL axis, such that the top and bottom metal layers are not overlapping.

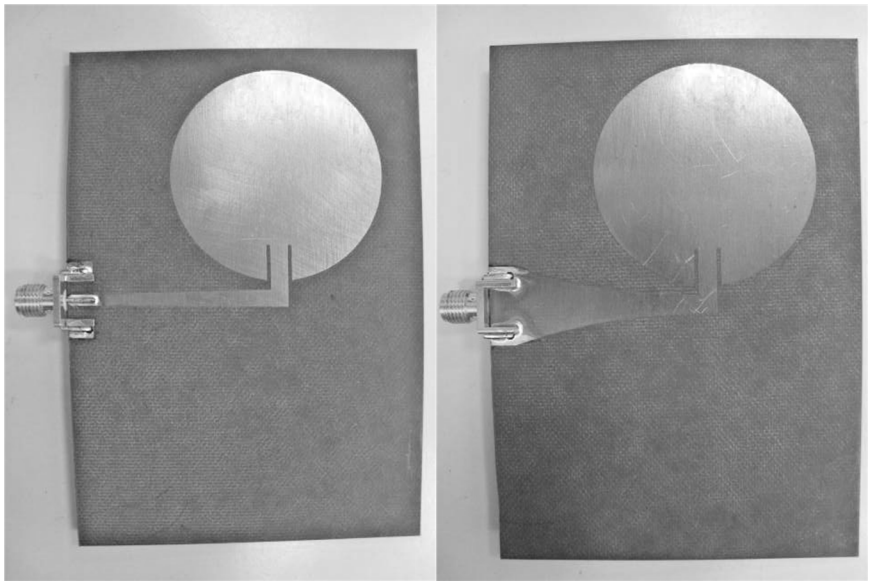

Fig. 15. Top and bottom metal layers of the DSPSL-fed radial dipole antenna, shown from left to right.

One example of a DSPSL-fed dipole is given in [11], where the authors have excited the DSPSL dipole with a coaxial probe feed. In that example, an unusually high 2:1 VSWR impedance bandwidth of 38.3% is reported, but in a similar experiment [12], the measured results show a 2:1 VSWR impedance bandwidth of only 9.6%. Compared with Li's data from [12], the results in this work make a 12.8% improvement in impedance bandwidth.

F. DSPSL-fed Radial Dipole Antenna Array

The shortened DSPSL-fed radial dipole was designed to allow a two-dimensional array of these dipole antenna elements to be fed by DSPSL with $\lambda/2$ spacing. Since the DSPSL is identical on both the top and bottom layers, the 4x4 antenna array is also identical on both the top and bottom layers.

The only differences between the top and bottom layers are found in the transition from coaxial to DSPSL that feeds the array and in the mirroring of the dipole elements between the two layers. The transition first converts from coaxial line to microstrip line and then converts from microstrip line to DSPSL in order to have a minimized return loss. Since microstrip transmission line is not identical between its ground and microstrip layers, the feed is also not identical between the top and bottom layers. In order to have dipole radiation, the dipole elements are symmetrically mirrored from the top to the bottom layer such that the metallization layers do not lie directly above each other.

The bottom of the 4x4 DSPSL-fed radial dipole array with no power weighting is shown in Fig. 16. This figure shows the corporate-H arrangement of radial dipole elements at a 3.00 GHz $\lambda/2$ element spacing on 31-mil RT/duroid 5870 substrate. The spacing between the elements is symmetrical in two-dimensions.

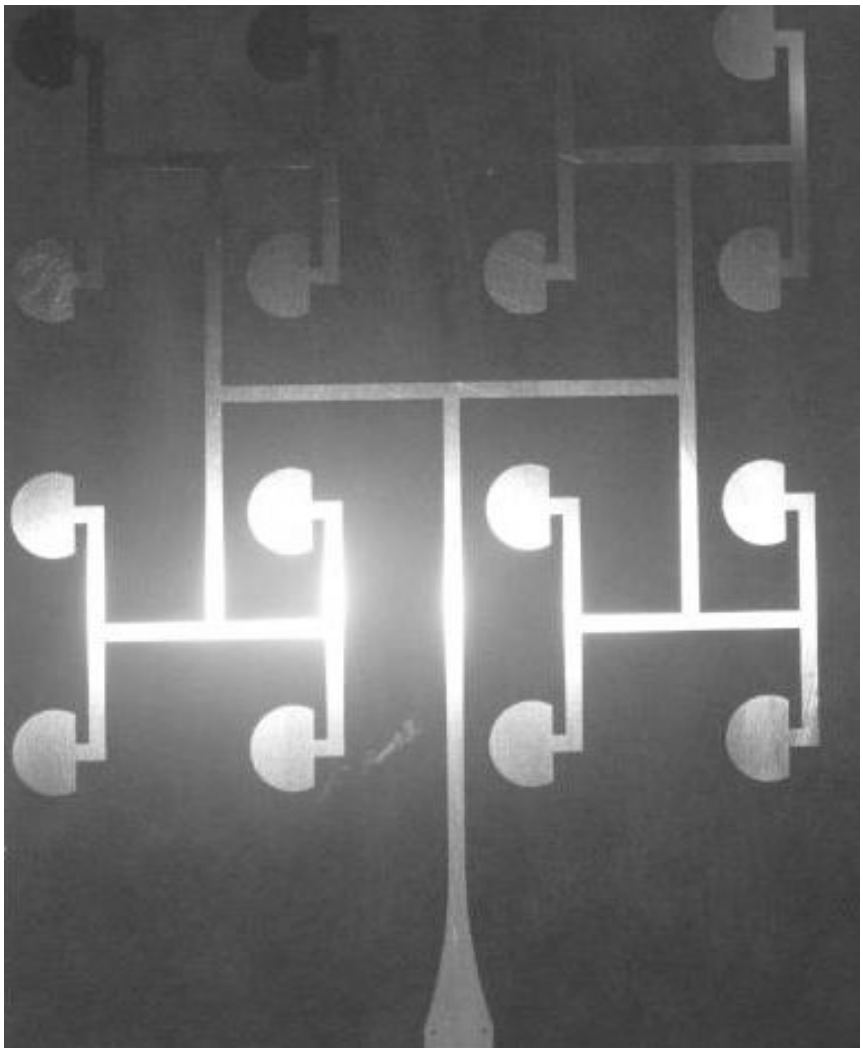

Fig. 16. Bottom of the 4x4 DSPSL-fed radial dipole array with no power weighting.

A $\lambda/2$ element spacing was chosen for several reasons. In order to combat fading in a uniform scattering environment, an element spacing of at least $\lambda/2$ is necessary so that the signals that different elements receive are approximately independent [13–15]. In order to avoid grating lobes, the inter-element spacing should be less than λ,

but to avoid aliasing and the misplacement of nulls, the inter-element spacing should be less than or equal to $\lambda/2$ [13, 16]. Therefore, a $\lambda/2$ element spacing was chosen to satisfy these three conditions.

Uniform, half, binomial, and combination power-weighting schemes showed varying results. The uniform scheme achieved the highest efficiency and gain, but the combination of half and binomial power schemes achieved the minimal SLL. The half and binomial power schemes showed that for symmetrical weighting in both directions, the element pattern caused the SLL to be lower in the x-z plane than in the y-z plane. The half power-weighting scheme did not achieve a -30 dB SLL, as was shown experimentally by Dr. Strassner in the 4x4 microstrip array, and the binomial power-weighting scheme did not achieve a 0 dB SLL, as is expected of a binomial current-weighting scheme.

For the designed 4x4 DSPSL-fed array, the minimal SLL is found at 3.05 GHz. Based on the array factor and element pattern multiplication, the SLL should be constant with respect to frequency, but that assumes a constant current distribution among all the elements regardless of the operating frequency. The power weighting schemes implemented between the elements force all of the elements to receive symmetrical power (based on the weighting) and equal phase, but they do not force the elements to receive constant current independent of frequency. Thus, the actual array does not have a fixed SLL independent of operating frequency.

G. Motivation for the UWB DSPSL-fed Circular Monopole Antenna

Circular and elliptical monopole antennas with microstrip transmission line feeds have been studied in the past for uses in UWB applications [17–21]. Instead of feeding the monopole antenna with a microstrip transmission line, this work feeds the monopole

with a double-sided parallel-strip line (DSPSL), as shown in Fig. 17.

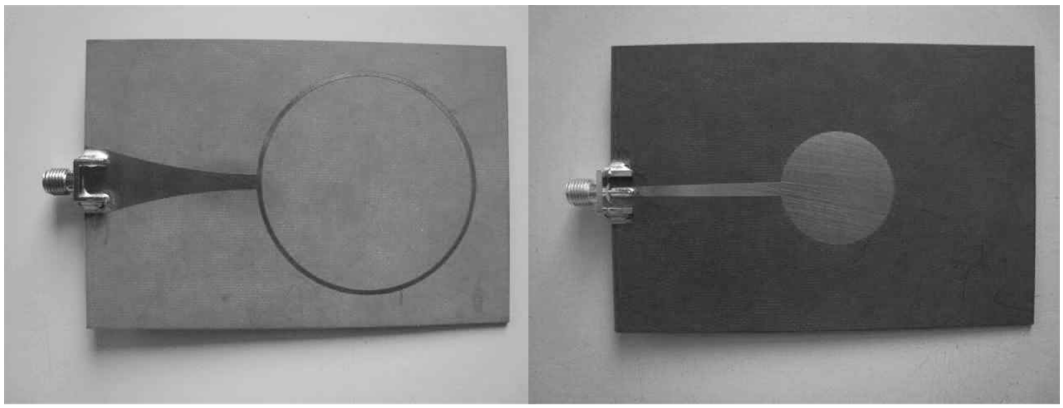

Fig. 17. DSPSL-fed circular monopole antenna's (a) bottom and (b) top sides.

By using the DSPSL feed, the ground of the monopole antenna is forced to cover a smaller area, allowing the antenna to be used in two-dimensional multi-directional antenna arrays with possible applications in radar tracking systems. This work presents the DSPSL-fed circular monopole and leaves arrays of such an element to future researchers.

CHAPTER II

DESIGN*

This chapter describes the design of the modified spiral and the related circuits. The UWB nature of the spiral antenna [1] and the UWB nature of the original microstrip-to-DSPSL transition [8] are complimented by the design of a UWB impedance transforming tapered DSPSL, which matches the spiral to the transition. Similar tapering concepts are applied to the microstrip-to-DSPSL transition and UWB DSPSL power divider, which are demonstrated with new antenna applications.

A. Spiral Antenna Design

The design equations for this spiral antenna and integrated feed are derived from several basic concepts. As shown in [1–7], antenna designers generally attempt to isolate the feed lines from the antennas and make energy propagate from the feed to the antenna or from the antenna to the feed efficiently. By isolating these components everywhere except at the points where they connect physically or through desirable coupling, designers may create each component individually and then connect the components together in a cascade. This design method relieves the burden of designing all of the antenna's components simultaneously.

---

*Part of the data printed in this chapter is reprinted from "Low-loss ultra-wideband double-sided parallel-strip line transition and power divider" by T. W. Eubanks and K. Chang, 2010. *Elect. Lett.*, vol. 46, no. 1, pp. 93-94, Copyright 2010 by The Institution of Engineering and Technology.

1. General Spiral Equations

After assuming that the cascade design method was possible for this antenna, the polar equations for equiangular spiral antenna arms given in [22] were massaged into parametric equations with impedance matching terms to draw the desired spiral in CST Microwave Design Studio with ultra-wideband operation. Eqs. 2.1-2.4 describe the four two-dimensional parametric curves that compose the spiral arm boundaries.

$$\begin{aligned} x &= R_o \cdot e^{A\theta} cos(\theta) \\ y &= R_o \cdot e^{A\theta} sin(\theta) \end{aligned} \tag{2.1}$$

$$\begin{aligned} x_2 &= (R_o + w - subtractor \cdot \theta) e^{A\theta} cos(\theta) \\ y_2 &= (R_o + w - subtractor \cdot \theta) e^{A\theta} sin(\theta) \end{aligned} \tag{2.2}$$

$$\begin{aligned} x_3 &= R_o \cdot e^{A\theta + i\pi} cos(\theta) \\ y_3 &= R_o \cdot e^{A\theta + i\pi} sin(\theta) \end{aligned} \tag{2.3}$$

$$\begin{aligned} x_4 &= (R_o + w - subtractor \cdot \theta) e^{A\theta + i\pi} cos(\theta) \\ y_4 &= (R_o + w - subtractor \cdot \theta) e^{A\theta + i\pi} sin(\theta) \end{aligned} \tag{2.4}$$

where x, x_2, x_3, and x_4 are the Cartesian coordinate references for the spiral arms' positions in the x-direction, y, y_2, y_3, and y_4 are the Cartesian coordinate references

for the spiral arms' positions in the y-direction, R_o is the radius of the spiral at its center, w is the initial width of the spiral's arms, A is the spiral expansion coefficient, t is the angle of the spiral, and *subtractor* is an impedance matching term which limits the spiral arms' width.

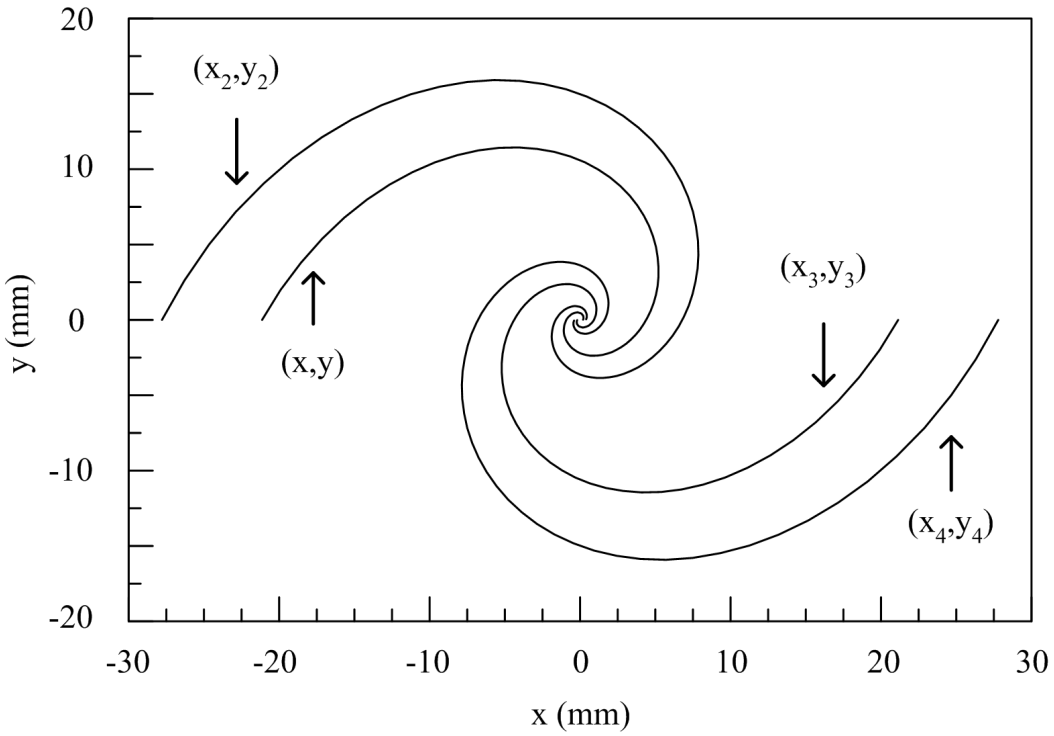

Fig. 18. The four spiral arm boundary curves.

Fig. 18 shows the spatial relationships between the curves given in Eqs. 2.1-2.4. The Cartesian coordinate reference used to draw these spiral arm boundaries is not the same as the Cartesian coordinate reference used everywhere else in this paper (see

Figs. 2-4). In Fig. 18 the y-axis direction is inverted with respect to the Cartesian coordinate reference used to measure the radiation patterns of the spiral.

The acid etching facilities at Texas A&M University cannot etch metal with a width less than 0.2 mm effectively, so the minimum spiral arm width (w) equals 0.2 mm. The minimum central radius of the spiral (R_o) equals 0.2 mm because parametric simulations showed that this initial radius gave the spiral an optimal return loss over the UWB range. After building the spiral completely in CST Microwave Design Studio and connecting the feed shown in Figs. 2-3, the A and *subtractor* values were chosen parametrically to select the best return loss from the antenna. According to these parametric analyses, $A = 0.5$ and $subtractor = 0.0147$ mm.

2. Parallel-plane Considerations

Since the parallel-strip feed line for this spiral carries fields around it as shown in [8], the conductive surface of the spiral antenna reflects some of those fields from the feed that would otherwise propagate to the spiral's center. In order to reduce those reflections and also to reduce the coupling from the feed to the spiral, holes were etched out of the spiral's surface at the places where the feed passed underneath. However, since the spiral cannot radiate without currents propagating through the spiral arms, the hole diameter used to reduce coupling between the spiral and the feed remained limited below the spiral arm width at a certain angle. If the holes became too large, then the spiral's arms would segment into several sections that could no longer propagate currents.

With these considerations, holes were cut from the spiral drawn in CST, and parametric analysis found optimal hole diameters for both of the holes centered above the feed line. Fig. 19 shows the results of this parametric analysis.

Since the equiangular spiral should be defined entirely by angles in order to be

infinitely wideband (with limitation only from the designed structure size) [1], the hole diameters for both holes were designed as a function of the angle of their centers from the origin so that the spiral's impedance and radiation bandwidths would not be limited by the holes' sizes. Effectively, this means that each hole's diameter relates directly to the spiral arm width at the angle of the hole's center, which lies directly above the center of the tapered parallel-strip feed. Fig. 19 calls the difference between the spiral arm width and the hole diameter the "remaining metal width".

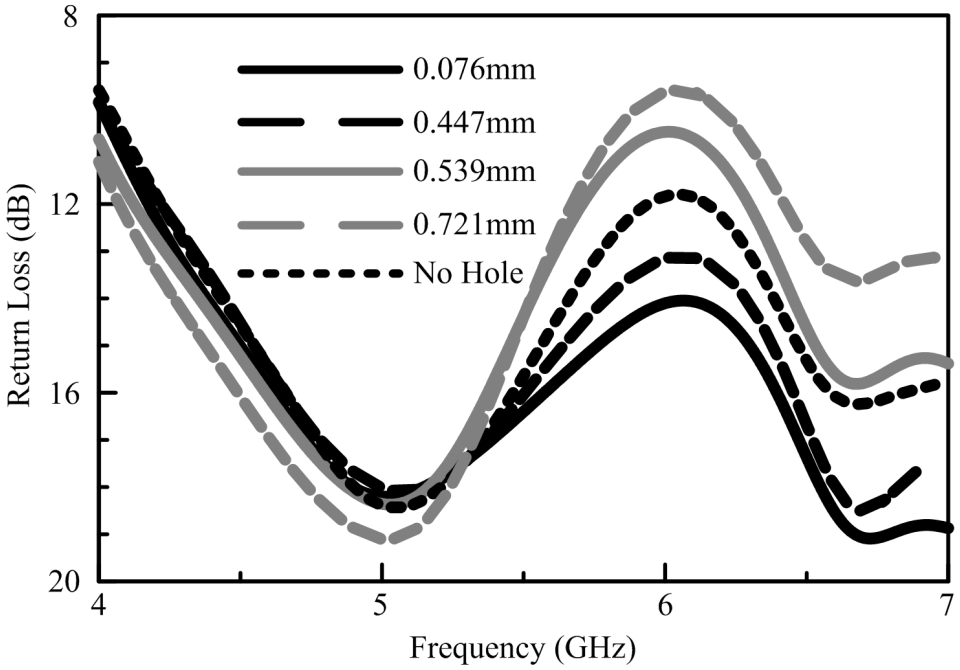

Fig. 19. Various spiral arm widths minus etching hole diameters (remaining metal widths) at specific angles produce varying return losses over the 4-7 GHz frequency range. The maximum metal width occurs with no etching hole present.

The smallest metal width (0.076 mm) produced the best average return loss (16.0 dB) over the 4-7 GHz frequency range. However, this metal width was too small to etch. For this reason, the spiral shown in Fig. 10 has 30 AWG wires (0.254 mm dia.) connecting the segmented sections of the spiral in the locations where the spiral became thinner than the resolution of the etching lab. This fabrication flaw might have produced the slight variation between the measured and simulated VSWR for the spiral with holes, shown later in this work.

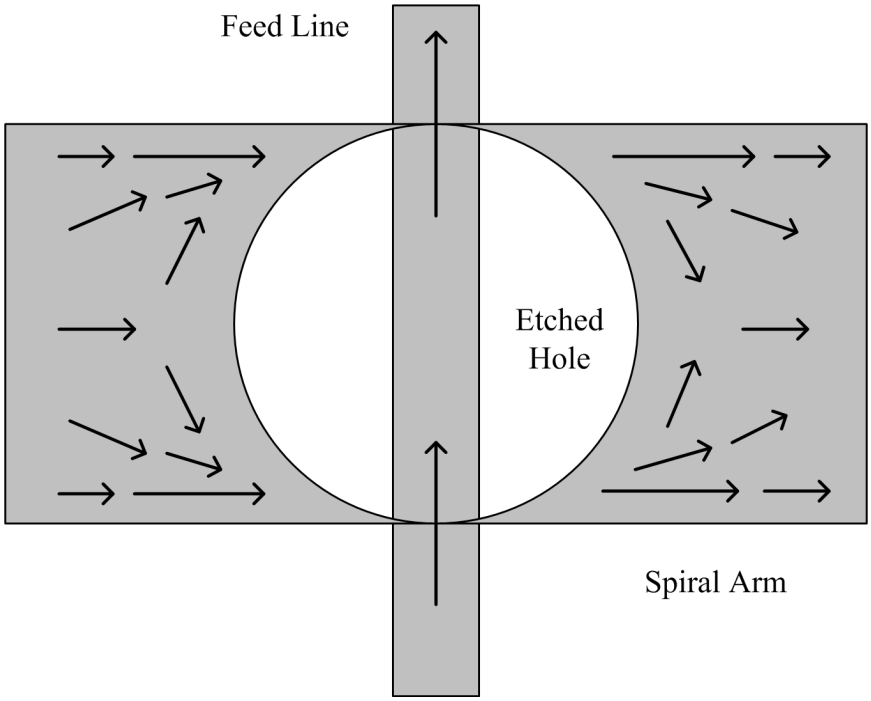

Fig. 20. The surface currents on a rectangular spiral are forced to travel on the tangent of the circle as they approach the crossing between the spiral and the feed. The tangent to the circle is perpendicular to the feed at the feed's center.

3. Perpendicular Currents

As a result of attempting to isolate the fields near the feed line from the fields near the spiral through parametric analysis, the currents through the feed line and the spiral naturally approached perpendicularity between each other. Parametric simulations aided in improving the antenna's return loss by altering the shape of the spiral and by finding the best positions and shapes for the etching holes.

After many of these simulations, the perpendicular-current situation gave the best performance. One can see visually in Fig. 20 that as the diameter of an etching hole approaches the spiral arm width, the currents along the spiral are forced in the direction of the tangent line to the hole at the crossing of the parallel-strip feed and the spiral. The direction of the currents through remaining metal becomes increasingly close to the tangent of the circle as the etched hole diameter approaches the spiral arm width. Fig. 20 idealizes this scenario with a rectangular spiral.

Although it seems that the same phenomenon cannot hold true for a non-rectangular spiral (since the tangent to the etching hole at the center of the feed becomes slanted for an equiangular spiral), simulations show that the vector sum of the currents on the top and bottom of the spiral lies in a direction approximately perpendicular to the direction of the currents on the feed. Altogether, this forces the fields radiated by the spiral and the fields transmitted by the feed to be non-interactive, or isolated from one another.

Fig. 21 shows the surface currents of the spiral antenna, as simulated by CST. The vector sum of the currents on the top and bottom of the equiangular spiral is approximately perpendicular to the currents traveling on the feed line below the spiral at the locations where the feed line passes underneath the spiral. Therefore the fields circulating around the currents on the spiral are mostly non-interactive with the fields

circulating around the currents on the feed line at those locations.

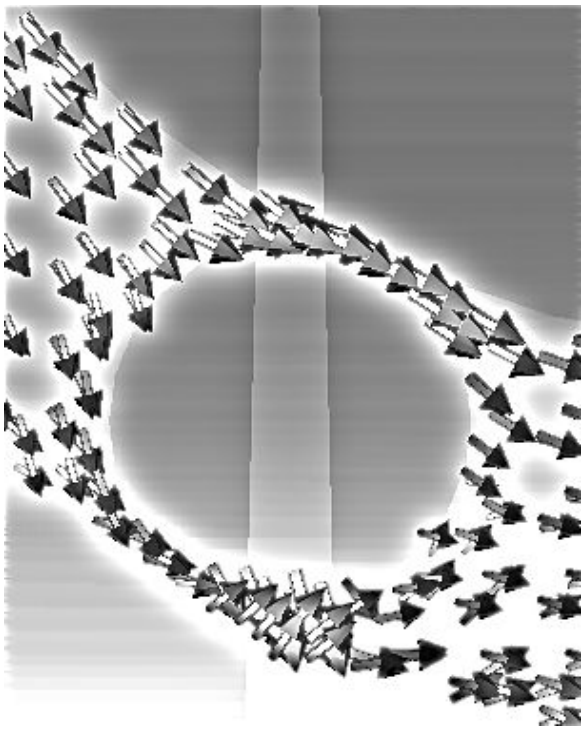

Fig. 21. The top and bottom surface currents on the equiangular spiral sum vectorially to produce a net current perpendicular to the feed's current at the point of crossing between the spiral and the feed.

When these currents become closer to perpendicular to each other, the return loss improves. This explains why the hole of greatest diameter produced the best return loss, as shown in Fig. 19, and it also explains why parametric analysis produced the perpendicular-current situation naturally.

B. Parallel-strip Line Feed Design

In order to match a broadband load to a broadband source of unequal characteristic impedance, one must use a broadband impedance transformer to allow operation of the system through that same broad bandwidth. Since the UWB microstrip to parallel-strip balun given in [8] and the spiral both operate in broad bandwidths, a broadband impedance transformation must match the impedance of the spiral to the 50 Ω microstrip line so that the total antenna and integrated feed may operate in a broadband spectrum. The theory of small reflections, as given in [23] describes the reflection coefficient Γ at the input of a transmission line as a function of the operation frequency f, the transition length L, and the variation of the characteristic impedance of the transmission line through space $Z(y)$.

1. Contributions of the Theory of Small Reflections

Eq. 2.5 shows the integrable $d\Gamma$ as derived in [23] as a function of the characteristic impedance Z, which is a function of position y. In Eq. 2.6, the integral is performed in the y-direction with a phase shift added from the theory of small reflections to find the total reflection coefficient for a transmission line. Eq. 2.7 shows the dependence of Γ in Eq. 2.6 on the frequency f and the speed of light c.

$$d\Gamma = \frac{1}{2}\frac{d(ln(Z(y)))}{dy}dy = \frac{dy}{2Z(y)}\frac{dZ(y)}{dy} \tag{2.5}$$

$$\Gamma = \frac{1}{2}\int_0^L e^{-2j\beta y}\frac{d}{dy}ln(Z(y))\,dy \tag{2.6}$$

$$\beta = \frac{2\pi f}{c} \tag{2.7}$$

The PPPC feed in this paper uses the the transition shown in Fig. 22 to match the UWB balun to the spiral antenna. Since the characteristic impedance of a parallel-strip line depends upon the width of the the line w, it also varies with space according to the relationship between w and y shown in Eq. 2.8, where w and y have millimeter units.

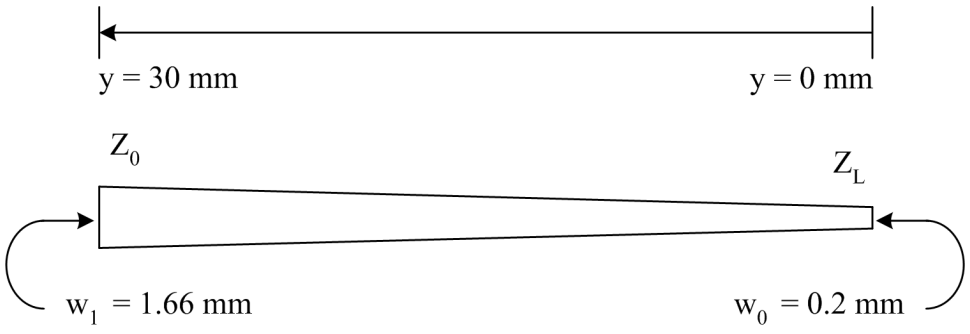

Fig. 22. The taper $w(y)$ used to create the parallel-plane perpendicular-current feed.

$$w = 0.2 + (0.0487)y \tag{2.8}$$

Wheeler explains in [24] that the characteristic impedance of a parallel-strip line

has two governing equations, one for wide strips and one for narrow strips. He also explains that the transition between these two equations usually happens when the width of the line equals half the height.

The equation for the narrow strip characteristic impedance (Eq. 2.9) and the equation for the wide strip characteristic impedance (Eq. 2.10) do not intersect at the transition region for the parallel-strip line in this paper, leaving a discontinuity in the characteristic impedance that gives an infinite value for the derivative of Z(y) at that transition. Due to the fact that the narrowest point on the parallel-strip line lies at $w/h = 0.4$ (substrate height $h = 0.508$ mm), which almost satisfies the wide strip condition according to Wheeler in [24] ($w/h \geq 0.5$), the wide strip equation is used to model this parallel-strip line's impedance over the entire length of the line (avoiding the discontinuity in Z(y)).

$$\begin{aligned} Z_{narrow\ strip} &= \frac{377\sqrt{2}}{\sqrt{\epsilon_r+1}}\frac{1}{\pi}(ln(\frac{4h}{w})+\frac{1}{8}(\frac{w}{h})^2 \\ &\quad -\frac{1}{2}(\frac{\epsilon_r-1}{\epsilon_r+1})(ln(\frac{\pi}{2}+\frac{1}{\epsilon_r}ln(\frac{4}{\pi}))) \end{aligned} \tag{2.9}$$

$$\begin{aligned} Z_{wide\ strip} &= 377(\epsilon_r)^{-1/2}(\frac{w}{h}+0.441 \\ &\quad +(\frac{\epsilon_r+1}{2\pi\epsilon_r})(ln(\frac{w}{h}+0.94) \\ &\quad +1.451)+\frac{\epsilon_r-1}{(\epsilon_r)^2}(0.082))^{-1} \end{aligned} \tag{2.10}$$

2. Calculating the Reflection Coefficient

After substituting w in Eq. 2.8 into Eq. 2.10, the characteristic impedance of the parallel-strip line becomes a function of position y, as shown in Fig. 23. At the narrowest part of the DSPSL, the characteristic impedance of the line reaches 200 Ω. Since a self-similar structure has a self-impedance of $\eta_0/2 \approx 188$ Ω [22], the 200 Ω side of the DSPSL has a good impedance match to the spiral. At the widest point on the DSPSL, the characteristic impedance drops to nearly 50 Ω. The wide end of the tapered DSPSL is well matched to the 50 Ω coaxial-line input.

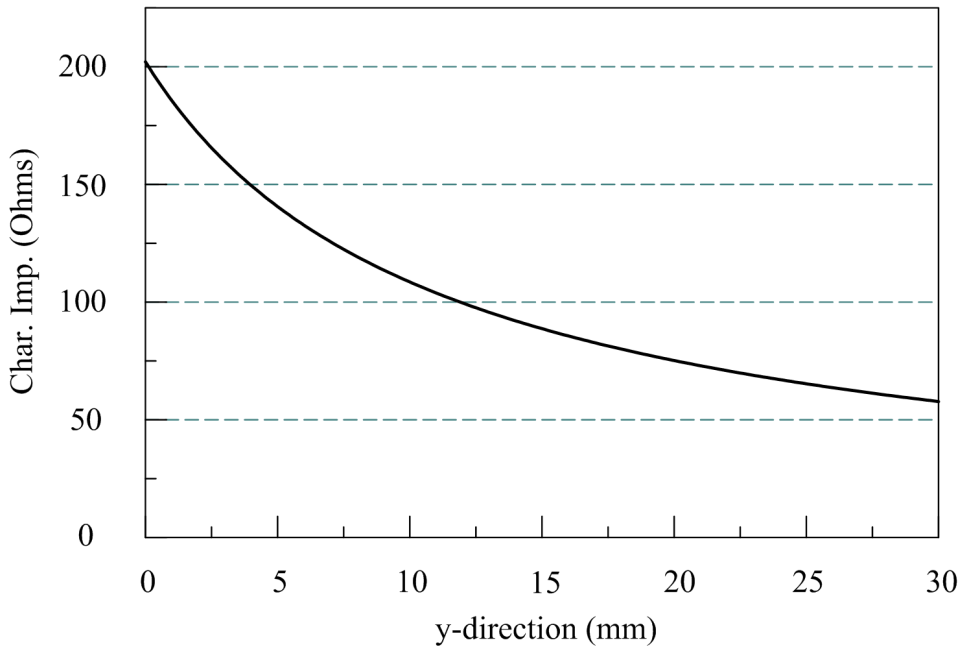

Fig. 23. Characteristic impedance of the parallel strip-line versus distance in the y-direction.

Then substituting this characteristic impedance $Z(y)$ into Eq. 2.6 gives the ratio value of Γ for a single frequency f. Taking the integral in Eq. 2.6 for many frequency points in the range 0-20 GHz gives the magnitude of the input reflection coefficient versus frequency for the perfectly-matched linearly-tapered transmission line, as shown in Fig. 24.

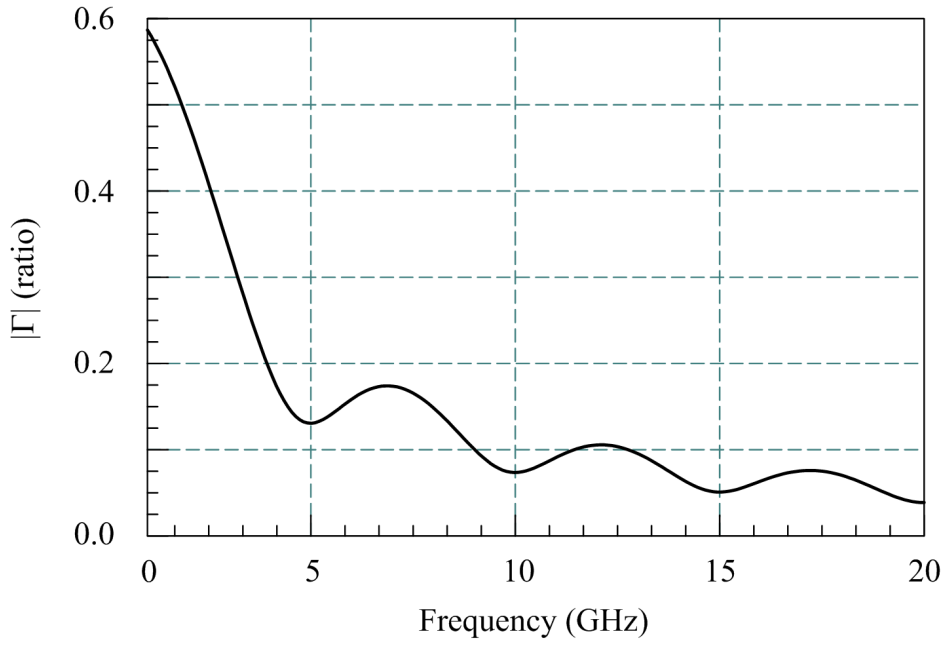

Fig. 24. Magnitude of the reflection coefficient for the perfectly-matched linearly-tapered parallel-strip line.

This shows the best possible reflection coefficient through the tapered parallel-strip transmission line, since these calculations assume that the transmission line is perfectly matched on both ends. The return loss through this tapered parallel-strip

line equals $-10log(|\Gamma|^2)$, and the return loss remains better than 10 dB for $f > 3$ GHz.

Now knowing the return loss intrinsic to the perfectly-matched linearly-tapered parallel-strip transmission line shown in Fig. 22, one can expect that the total return loss from the antenna specified in Fig. 1 will be worse than the return loss of the tapered transmission line since other losses exist in the spiral specified in [1] and in the UWB transition specified in [8]. This means that the complete antenna and integrated feed should operate at frequencies greater than or equal to 3 GHz since the tapered transmission line cannot operate below 3 GHz with less than 10% power reflection. This transmission line meets the requirements for UWB operation since the FCC allotted frequency band for UWB lies between 3.1-10.6 GHz.

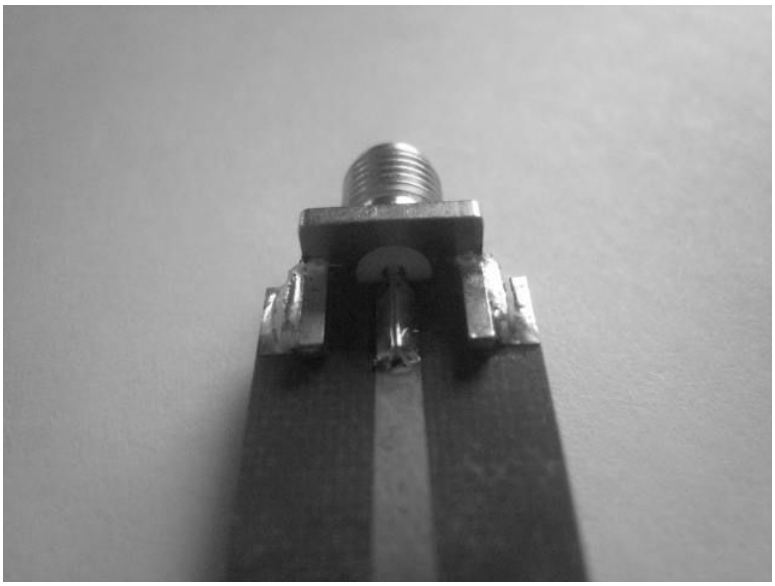

Fig. 25. Coaxial-to-DSPSL transition top.

C. Coaxial-to-DSPSL Transition Design

The coaxial-to-microstrip transition utilizes an SMA PCB mount end-launch jack designed for a 31 mil substrate. The center pin of the SMA connector solders directly to the top of the microstrip line as shown in Fig. 25. The sides of the SMA connector are soldered to a grounding tab and to a bent 18 AWG (1.024 mm) wire pushed through a via hole to the ground plane. This via connection prevents the currents traveling outward from the coaxial connection from being reflected at the edge of the ground terminations on the top side of the DSPSL.

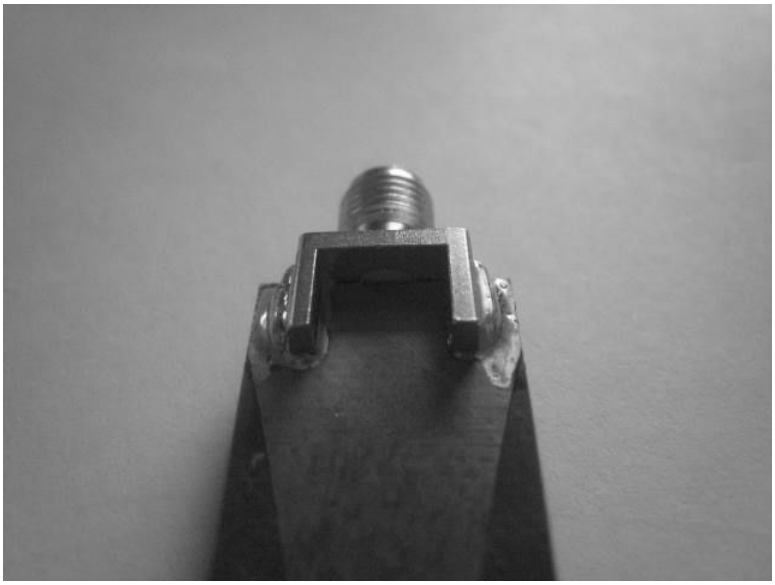

Fig. 26. Coaxial-to-DSPSL transition bottom.

The ground extensions of the SMA connector act like a coplanar waveguide on

the top side of the substrate, but the bottom of the substrate contains a microstrip ground as shown in Fig. 26. As shown in Fig. 26, the bent wires pushed through the via holes from the top side are also soldered to the ground plane on the bottom of the substrate.

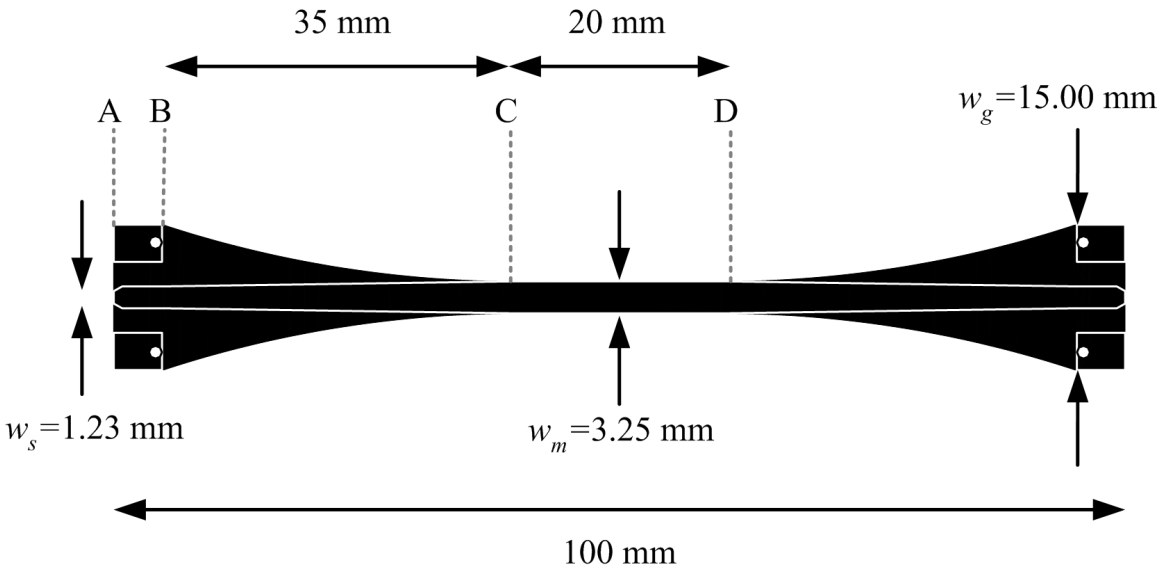

Fig. 27. Coaxial-to-DSPSL transition dimensions.

This quasi-microstrip, quasi-coplanar waveguide section (speaking of both the bottom and the top planes) has improved performance over the more abrupt junction shown in Figs. 2-3, which is fed by a tab-terminated SMA connector without a gradual transition from coaxial-to-microstrip transmission line. Fig. 27 shows the designed layout of the coaxial-to-DSPSL transition in a 2D format, wherein the top layer is

outlined in white above the bottom layer. The copper in both layers is black.

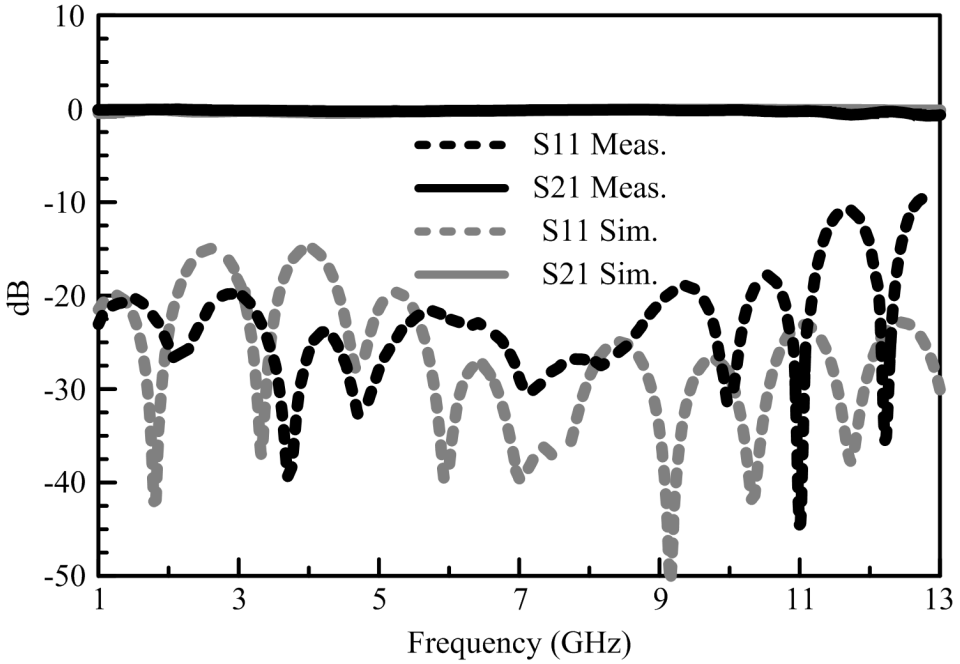

Fig. 28. Throughput and reflected power levels of the coaxial-to-DSPSL transition.

The theory of small reflections showed previously that a low-loss UWB DSPSL impedance transformer from 50 Ω to 188 Ω could be created by linearly tapering a DSPSL line through a length of 30 mm. Since the rigorous characteristic impedance equations for the transitional regions shown in Fig. 27 are unknown, the reflection coefficient's dependence on frequency cannot be as easily calculated for this transmission line. However, parametric simulations in CST Microwave Studio and measured results show that this transitional transmission line has low loss between 1-11 GHz.

The throughput and reflected power levels for this circuit are given in Fig. 28. The back-to-back coaxial-to-DSPSL transition exhibits insertion losses better than 0.3 dB and return losses better than 14.6 dB from 1.00-11.27 GHz. Since this transition has a 1 dB to 2 dB better insertion loss than the transition from [8] in the UWB frequency range, it is better suited for use in the design of UWB DSPSL-fed circuits and antennas.

This transition is essentially a 50 Ω to 50 Ω impedance transformer that uses similar geometries to those shown in the previously calculated PPPC fed spiral's tapered DSPSL and in the UWB microstrip-to-DSPSL transition in [8]. The back-to-back coaxial-to-DSPSL transition adopts the linearly tapered 30 mm DSPSL line used in the PPPC-fed spiral by applying that tapered line's geometry to the microstrip line on the top of the transition. The circularly chamfered microstrip ground used in [8] was extended in the transition shown in Fig. 27 in order to decrease the chamfered region's loss and match the length of the linear taper on the other side.

By extending the length of both the top and bottom transitions from 30 mm to 40 mm, the lower operation frequency of the transition – as given by the 2:1 VSWR bandwidth – was reduced from 3 GHz to 1 GHz. Since the length of the transition was extended 10 mm longer than the length of the linearly tapered DSPSL, the transition became less abrupt to longer wavelength frequencies, thereby reducing the losses between 1 GHz and 3 GHz.

For an antenna designed to operate in the entire UWB band from 3.1-10.6 GHz, a feed with a bandwidth exceeding the UWB region can appropriately show the antenna's operating frequency. If both the antenna and the feed are designed to operate at the same frequencies, it may be difficult to tell whether the antenna or the feed limits the operating frequency if unexpected results occur when they are measured simultaneously. Sometimes measured results provide higher losses than the

simulated results, and in that case, it would be helpful to know whether the antenna or the feed were providing higher losses in the circuit. Therefore, the designed low-loss UWB transition from coaxial-to-DSPSL can be used to appropriately measure the operating frequency of a DSPSL-fed antenna in the entire UWB band.

In Fig. 27, the coaxial center-pin extends through section A-B, which transforms the coaxial transmission line into a microstrip transmission line. At segment A, the top of the quasi-microstrip line has a width equal to the width w_s of the coaxial center-pin. In the next 0.83 mm extending from segment A towards segment B, the quasi-microstrip line linearly tapers from 1.23 mm to 2.15 mm, where the larger width corresponds to a 50 Ω characteristic impedance for microstrip line on 31-mil 5870 RT/duroid.

In section B-C, the transition transforms the microstrip transmission line from segment B to a DSPSL at segment C. The width of the top line linearly tapers from 2.15 mm near segment A to 3.25 mm at segment C, while the bottom line circularly tapers from 15.0 mm at segment B to 3.25 mm at segment C. The larger width corresponds to a 50 Ω characteristic impedance for DSPSL on the aforementioned substrate.

Section C-D of the back-to-back transition propagates fields completely in a DSPSL. For a circuit utilizing the DSPSL connection provided by the transition, the circuit would be connected to segment C, where section A-C provides the complete transformation from coaxial line to DSPSL.

D. UWB DSPSL Equal Power Divider Design

A 3 dB in-phase power divider was constructed using three of the aforementioned coaxial to DSPSL transitions and three tapered DSPSLs. Fig. 29 illustrates the

design of the complete DSPSL power divider with the power division components shown inside of the gray hashed box. The DSPSL coming from port 1 tapers from 3.25 mm to 3.45 mm (w_c) at the center of the power divider. Both of the other DSPSLs from port 2 and port 3 taper to 1.15 mm at the center of the power divider. The taper from port 1 to the center of the divider is only 20 mm long, while the tapers from ports 2 and 3 to the center of the divider are 25 mm long.

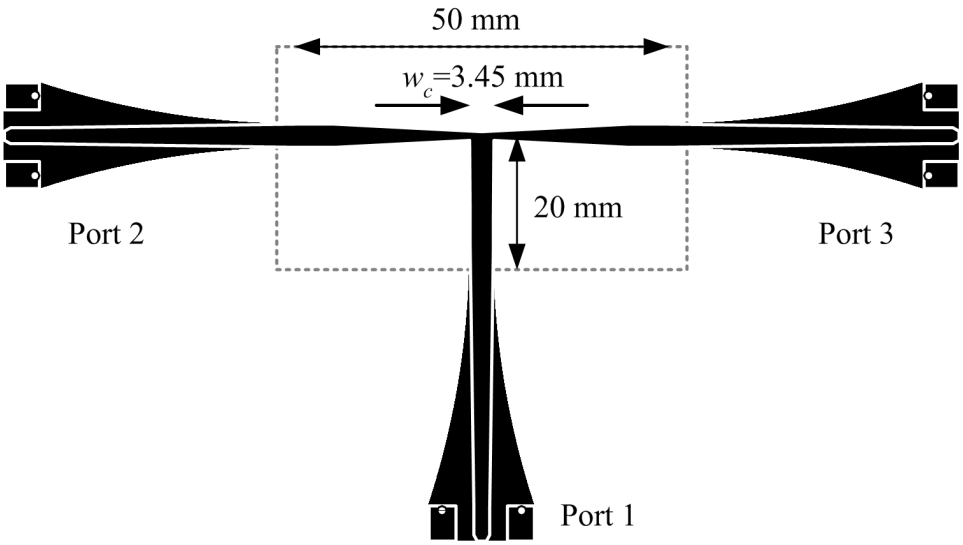

Fig. 29. UWB DSPSL power divider with three coaxial-to-DSPSL transitions.

In an array of differential antennas, all of the coaxial-to-DSPSL transitions would be unnecessary except for possibly port 1, depending on the connector configuration of the user's power amplifiers. Port 1 serves as the power dividers input, and as such

it may be necessary in most cases to use a coaxial-to-DSPSL transition at port 1 in order to feed the power divider and to take measurements on the power divider. Without the coaxial to DSPSL transition, it would be difficult to connect the DSPSL power divider to a network analyzer.

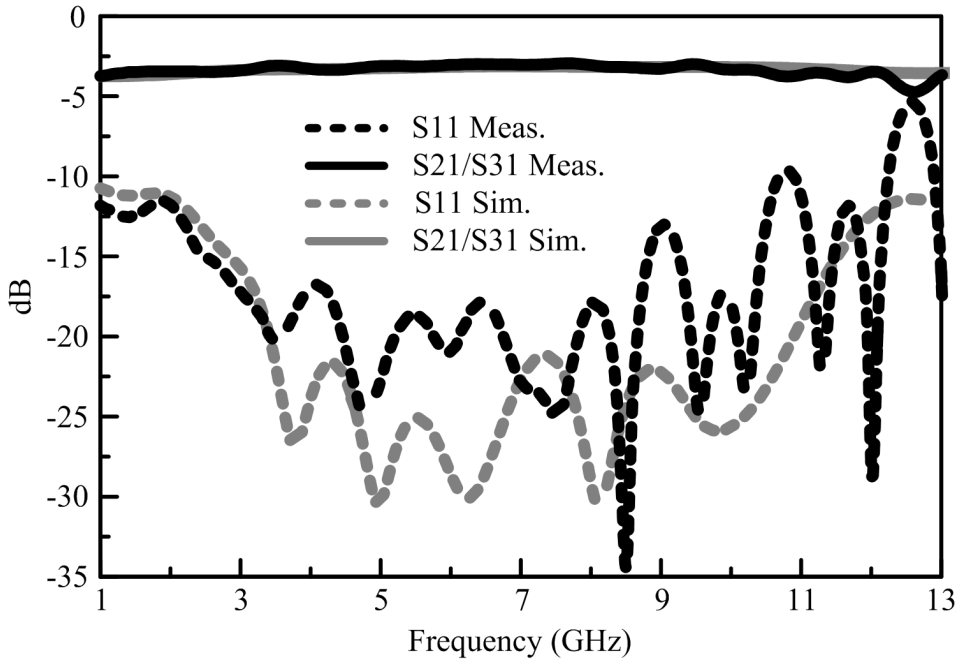

Fig. 30. Throughput and reflected power levels of the 3 dB in-phase UWB DSPSL power divider.

With an equal amplitude DSPSL power divider designed, a symmetrical array of DSPSL-fed antennas can be created. Since the designed power divider exhibits low losses over the entire UWB range, minimal power would be wasted in the array's feed

network for an array of any variety of antennas inside the UWB frequency band.

Fig. 30 shows the return and insertion losses of this divider by plotting $10log(|S|^2)$. This connectorized power divider exhibits throughput power levels from port 1 to both port 2 and port 3 that are better than 3.7 dB down from the input power level from 1-10.7 GHz. It also exhibits return losses that are better than 10 dB from 1-10.7 GHz. The phase difference between S21 and S31 is $0° \pm 1.1°$ from 1-13 GHz.

The most desirable characteristics in the UWB DSPSL equal amplitude power divider are minimal reflection at the input port (port 1), maximal transmission to the output ports (ports 2 and 3), equal amplitude transmission to the outputs, and equal phase at the outputs. The designed UWB DSPSL 3 dB power divider exhibits all of the characteristics, most of which are shown in Fig. 30. The phase differences between the output ports are so minimal that plotting the port phases together over the UWB band shows them overlapping.

The isolation between the output ports is less important than these other characteristics. When the corporate-H fed array receives a signal, the two output ports are stimulated simultaneously with the same received signal due to the corporate-H symmetry. Therefore, isolating the received signal at port 3 from port 2 is meaningless. For transmitted signals, port isolation is also meaningless because the signal from port 1 is split and given to both port 2 and port 3.

E. UWB DSPSL Unequal Power Divider Design

The previously described 3 dB in-phase DSPSL equal power divider that has low loss over the frequency range from 1 to 11 GHz was adapted to create an unequal power divider that also has equal phase outputs at two ports. This unequal power divider was demonstrated in the corporate-H fed 4x4 array of DSPSL dipole antennas, whose

implementation is later described. In that array, the 3 dB equal amplitude power divider splits the power three times near the center of the array, and the unequal power divider splits the power twelve times near the elements in order to reduce the SLL of the array.

The UWB DSPSL unequal power divider is defined by six separate parameters that describe various widths and lengths at certain sections of the divider. For each port, there are two distinct parameters that characterize the power divider along the DSPSL tapered linearly from the port to the center of the divider. Each port is designed to match a 50 Ω impedance, so the widths of the ports is constant (w_0).

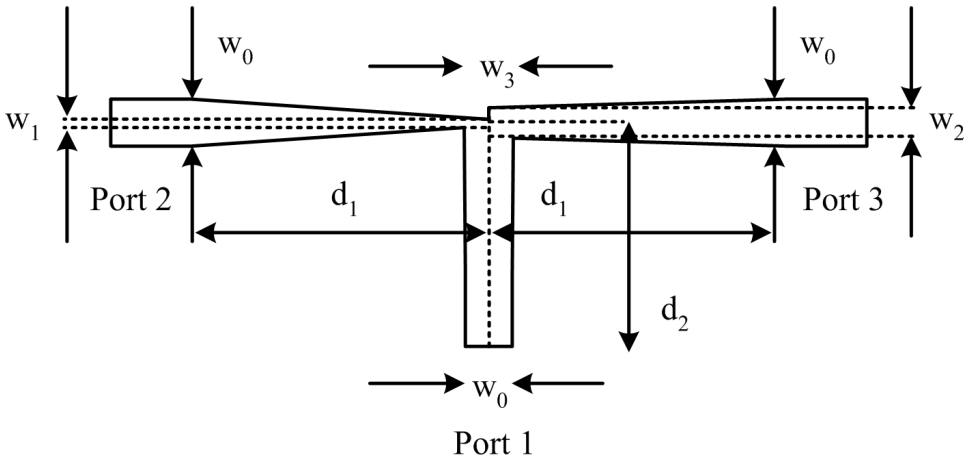

Fig. 31. Unequal power divider for the 2:1 and 3:1 configurations.

The lengths of the tapered DSPSL sections and the widths of the DSPSLs at the center of the divider determine the power ratios between port 2 and port 3, the

phase differences between the ports, the return loss at port 1, and the insertion losses between the input and the outputs. Since it is desirable to have equal phases at the output ports for a broadside array of antenna elements, the lengths of the tapered DSPSL sections leading to the two output ports are fixed.

Table I. Unequal Power Divider Parameters

Parameter	2:1 Value (mm)	3:1 Value (mm)
w_0	3.15	3.15
w_1	0.44	0.44
w_2	2.00	3.30
w_3	3.30	3.86
d_1	20.0	20.0
d_2	10.0	10.0

The unequal power divider shown in Fig. 31 can be designed to provide twice as much power to port 3 as it does to the port 2. For the purpose of this work, this half-power divider is referred to as the 2:1 unequal power divider. A 3:1 unequal power divider is necessary to create a binomial power distribution in an antenna array, and it can be created from the 2:1 unequal power divider's form with modified parameters. Table I gives the parameter values for both the 2:1 and 3:1 unequal power dividers. The throughput and reflected power levels for these two dividers are shown in Fig. 32.

In the 2:1 unequal power divider, port 3's received power is 1.80 dB down from

the input power level at 3.00 GHz, and port 2's received power is 4.80 dB down from the input power level at 3.00 GHz. This corresponds to a 3 dB power difference between the ports, which means that twice as much power is going to port 3 as is going to port 2. Also, it means that 99.2% of the input power is being received by the output ports at 3.00 GHz.

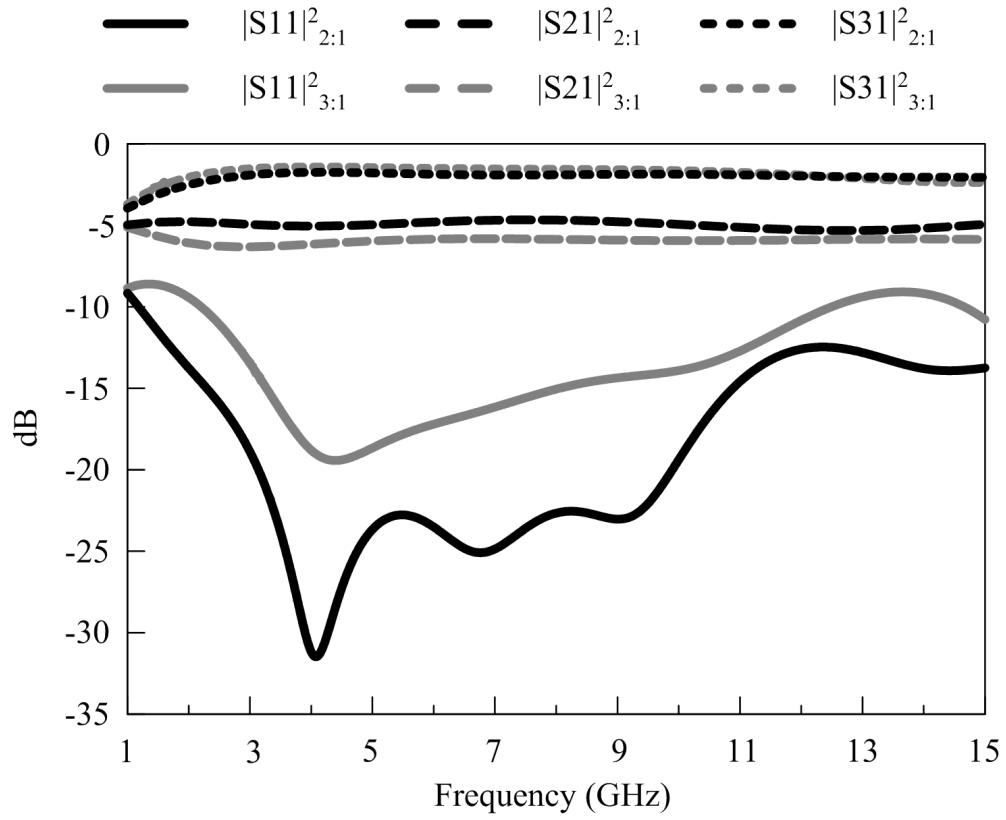

Fig. 32. Through and reflected power levels for the 2:1 and 3:1 power dividers.

For the 3:1 unequal power divider, the power received at port 3 is 1.55 dB down from the input power level, and the power received at port 2 is 6.35 dB down from the input power level at 3.00 GHz. This corresponds to a 4.8 dB power difference between the ports, which means that three times as much power is going to port 3 as is going to port 2. It also shows that 93.2% of the input power is being received by the output ports at 3.00 GHz. As can be seen in Fig. 32, the 2:1 power divider has a lower reflected power level than the 3:1 power divider, so it is expected that less power will be received by ports 2 and 3 in the 3:1 divider.

Now that the power dividers necessary for half-power and binomial weighting schemes have been described, four different symmetrical implementations of these dividers can be inserted into the DSPSL-fed 4x4 antenna array to test the weighting schemes' effects upon the array's impedance bandwidth, SLL, and radiation efficiency. Before the array is completely described, the designs of the antenna elements used in the array are divulged.

F. DSPSL-fed Dipole Antennas

Several different types of antennas could have been chosen for this array, but it was desirable to choose an antenna that physically fit within the size constraint for a half-wavelength spaced array at 3.00 GHz. At 3.00 GHz, the half-wavelength spacing limits the antenna elements to be less than 25 mm in both vertical and horizontal directions. Four different suitable antennas for the array are presented in this section.

1. Radial Dipole Antenna

Payne showed in [10] that radial elements on the end of shortened dipoles cause those dipoles to have increased efficiency and increased bandwidth at their shortened

lengths. The radial dipole was designed with a DSPSL feed for the purpose of inserting it into a 4x4 array, and that 4x4 array was measured and simulated. Fig. 33 shows the structural parameters defining the radial dipole, and Table II defines the parameters' values used in this paper.

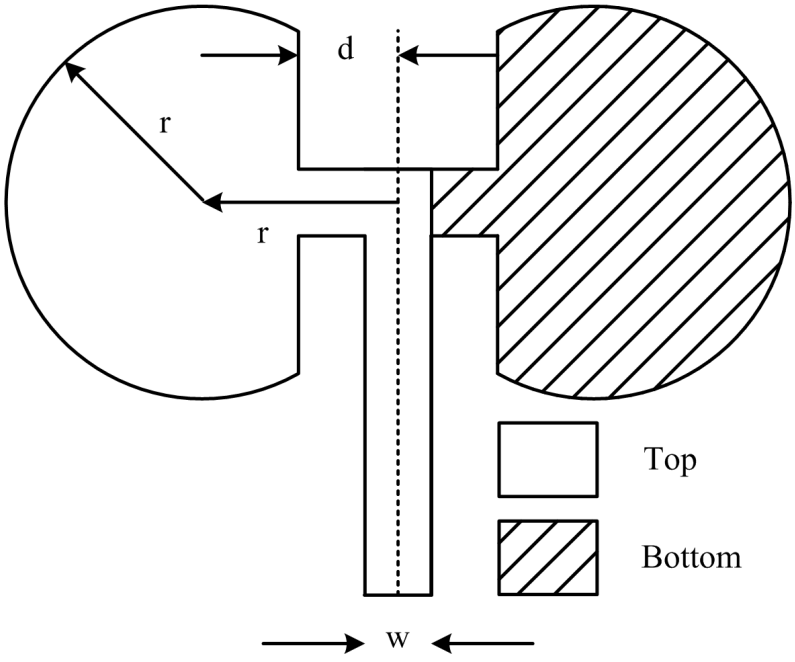

Fig. 33. DSPSL-fed radial dipole antenna.

Table II. Radial Dipole Parameters

Parameter	Value (mm)
r	9.50
d	4.80
w	3.15

2. Bowtie Antenna

A DSPSL-fed bowtie antenna, as shown in [25], has a dipole radiation pattern with wider impedance bandwidth than the straight-wire dipole. The terminating edge of the bowtie antenna is similar to the terminating edge of the radial dipole in that both antennas carve out a radial arc, but unlike the radial dipole, the bowtie's edges are defined by the angle θ from the symmetry axis. Fig. 34 shows the bowtie antenna used in this paper, and Table III shows the antenna's design parameters and their values.

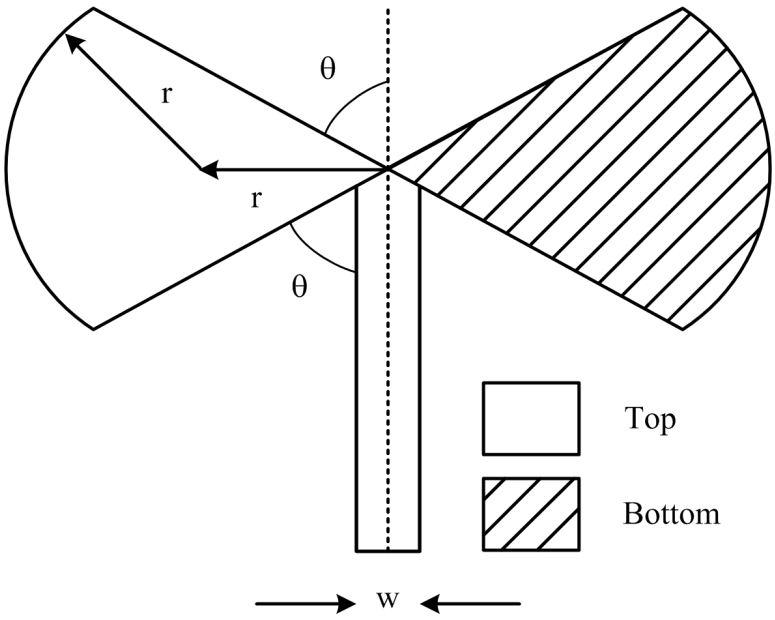

Fig. 34. DSPSL-fed bowtie antenna.

Table III. Bowtie Parameters

Parameter	Value
r	9.50 mm
w	3.15 mm
θ	26.6°

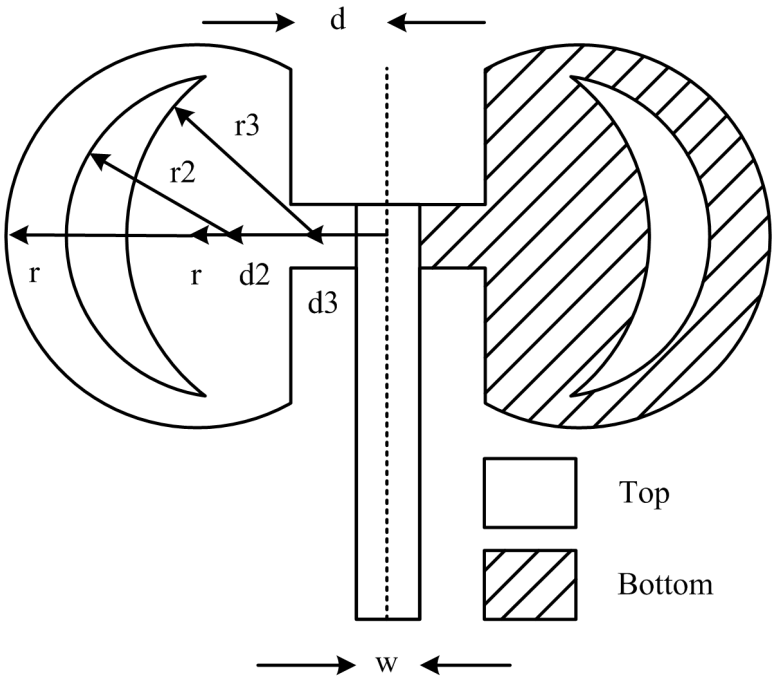

Fig. 35. DSPSL-fed slotted radial dipole antenna.

3. Slotted Radial Dipole Antenna

The slotted radial dipole is simply a short study on the effects of adding slots to the radial dipole to observe the changes in the antenna's impedance bandwidth. This

antenna exhibits a dipole radiation pattern equal to the pattern of the non-slotted radial dipole, but the impedance bandwidth of the dipole is smaller than the bandwidth of the non-slotted radial dipole. Since the radiation pattern is unaffected by the slots but the impedance bandwidth is affected, the slots can be used to tune the impedance of a radial dipole that is mismatched to its feed.

Table IV. Slotted Radial Dipole Parameters

Parameter	Value (mm)
r	9.50
r2	8.00
r3	10.0
d	4.80
d2	8.00
d3	3.00
w	3.15

The outer radial arc is the same arc shown in Fig. 33, but the two inner arcs are defined by radii of different lengths with different offset values. Fig. 35 shows the radii and offsets as well as the other parameters of the slotted radial dipole used in this paper. Table IV shows the values of those parameters.

4. Tri-circularly Tapered Dipole Antenna

A dual-circularly tapered dipole antenna was presented in [26] that had an exceptional 2:1 VSWR bandwidth at its lower operating frequencies compared to the other antennas in that paper. In order to match the antenna to a 50 Ω line instead of a 100 Ω line as shown in [26], the third circular taper was added to this antenna to make it a tri-circularly tapered dipole antenna.

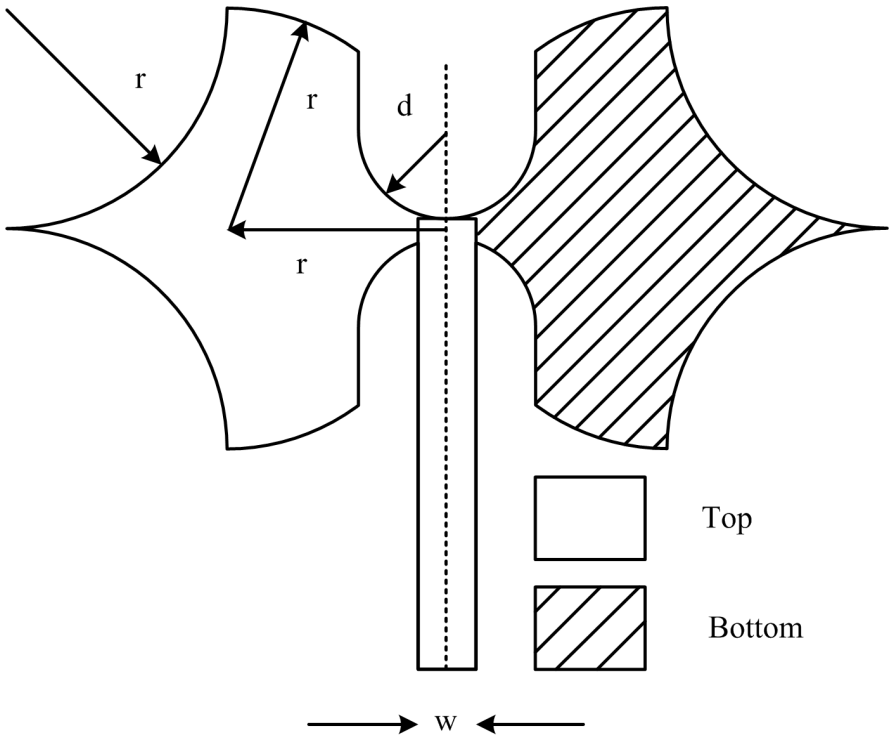

Fig. 36. DSPSL-fed tri-circularly-tapered dipole antenna.

Since the power dividers for the 4x4 array were already designed with 50 Ω outputs and little room was left for impedance transitioning, it was necessary to match these antennas to 50 Ω to consider them for the array. Fig. 36 presents the tri-circularly tapered dipole, and Table V shows the values for the antennas design parameters used in this paper.

Table V. Tri-circularly-tapered Dipole Parameters

Parameter	Value (mm)
r	12.0
d	4.80
w	3.15

5. VSWR of The Designed Dipoles

Since the capacitive coupling among the tightly spaced elements in the 4x4 array increases the center frequency of the impedance bandwidth, the elements were all designed for approximately a 2.75 GHz center frequency so that the array could have a center frequency of approximately 3.00 GHz. The VSWRs of these antennas are shown in Fig. 37. The notations “RD”, “SRD”, and “TCTD” represent the radial dipole, slotted radial dipole, and tri-circularly tapered dipole, respectively.

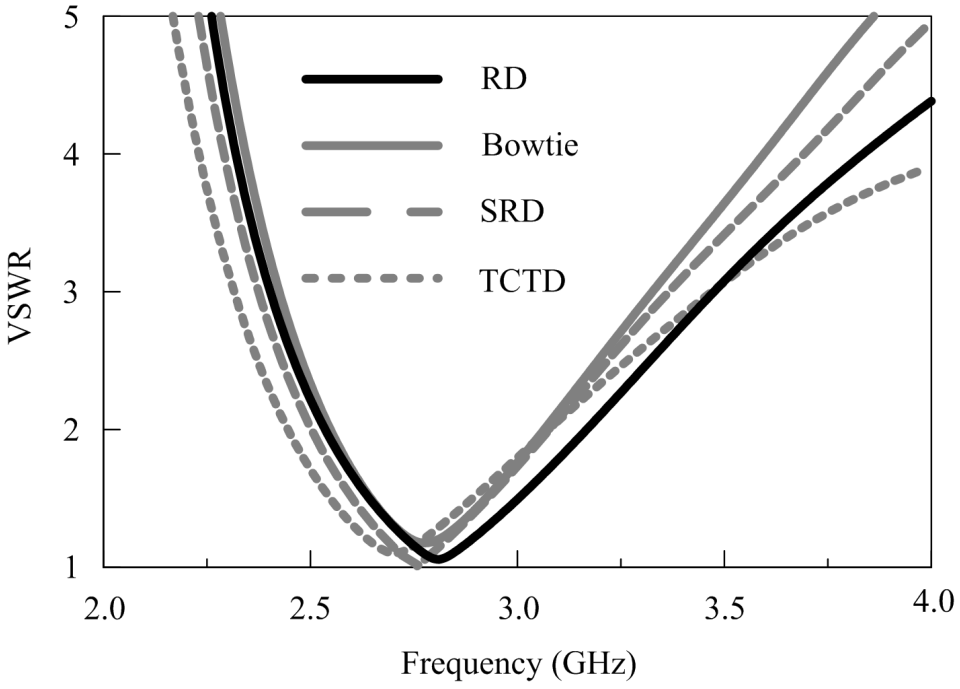

Fig. 37. VSWRs of the various DSPSL-fed dipole antennas.

The 2:1 VSWR bandwidths for the radial dipole, bowtie, slotted radial dipole, and tri-circularly tapered dipole antennas are 640 MHz, 530 MHz, 580 MHz, and 640 MHz, respectively. The radial dipole and tri-circularly tapered dipole have the largest (and equal) bandwidths with the given design parameters, but its possible that the bandwidths of these antennas may be improved with additional impedance matching sections added to the DSPSL prior to the antennas.

6. Radiation Pattern of the Designed Dipoles

All of the designed dipoles have a wide-band linearly polarized radiation pattern with a 2 dB gain and a 45° half-power beamwidth. The radiated E_θ and E_ϕ fields are shown

in Fig. 38 for varying degrees of θ in the x-z and y-z planes. The y-z plane is co-linear with the dashed line in the antenna's DSPSL feed (Figs. 33-36) and perpendicular to the surface of the antenna. The x-z plane is perpendicular to both the antenna's surface and the y-z plane. The x-y plane is co-planar with the antenna's surface. The 3-dimensional representations of the dipoles' radiated $|E|$ fields are given in Fig. 39, as simulated by CST Microwave Studio.

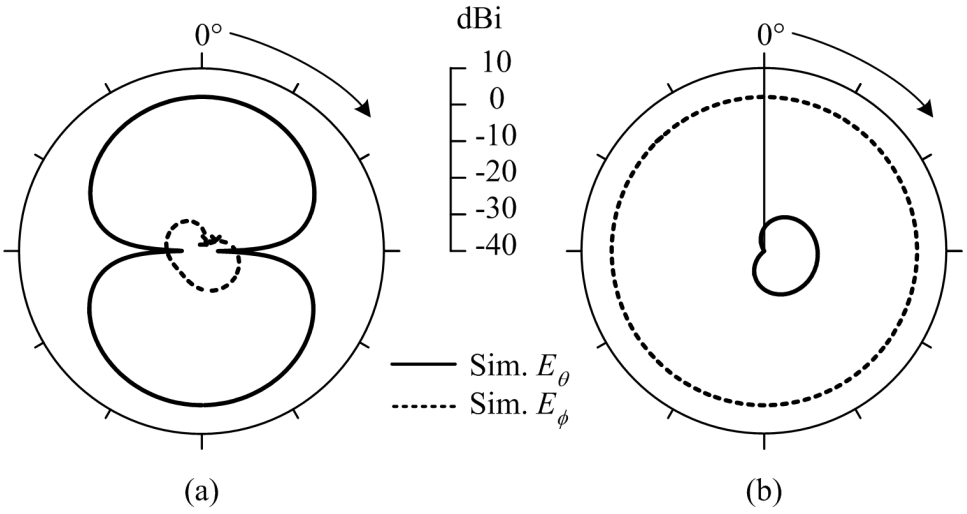

Fig. 38. Radiated E_θ and E_ϕ versus θ angle for the designed dipoles in the (a) x-z and (b) y-z planes.

Since the radial dipole is 5 mm narrower than the tri-circularly tapered dipole and since both dipoles have the same radiation pattern and impedance bandwidth, the radial dipole was chosen for the 4x4 DSPSL-fed array. The tri-circularly tapered dipole is 24 mm wide, but only 25 mm of clearance are available between the ad-

jacent DSPSL transmission lines in the corporate-H fed DSPSL array. The 19 mm wide radial dipole antenna leaves 3 mm of clearance between the antenna and the transmission line on both sides of the antenna.

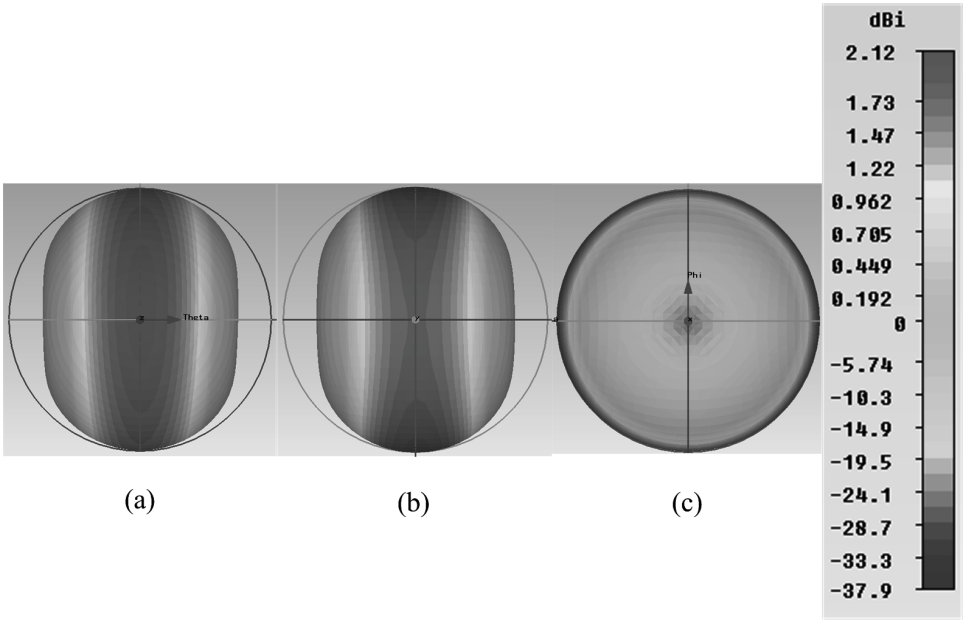

Fig. 39. Radiated $|E|$ fields for the designed dipoles in the (a) x-y, (b) x-z, and (c) y-z planes.

G. DSPSL-fed Radial Dipole Array Design

The 4x4 radial dipole array with a half-power weighting scheme is shown in Fig. 40. This array was fabricated on a 31-mil 5870 RT/duroid substrate, and the radial dipole elements were spaced 50 mm away from each other (center-to-center) based on

a half-wavelength spacing at 3.00 GHz.

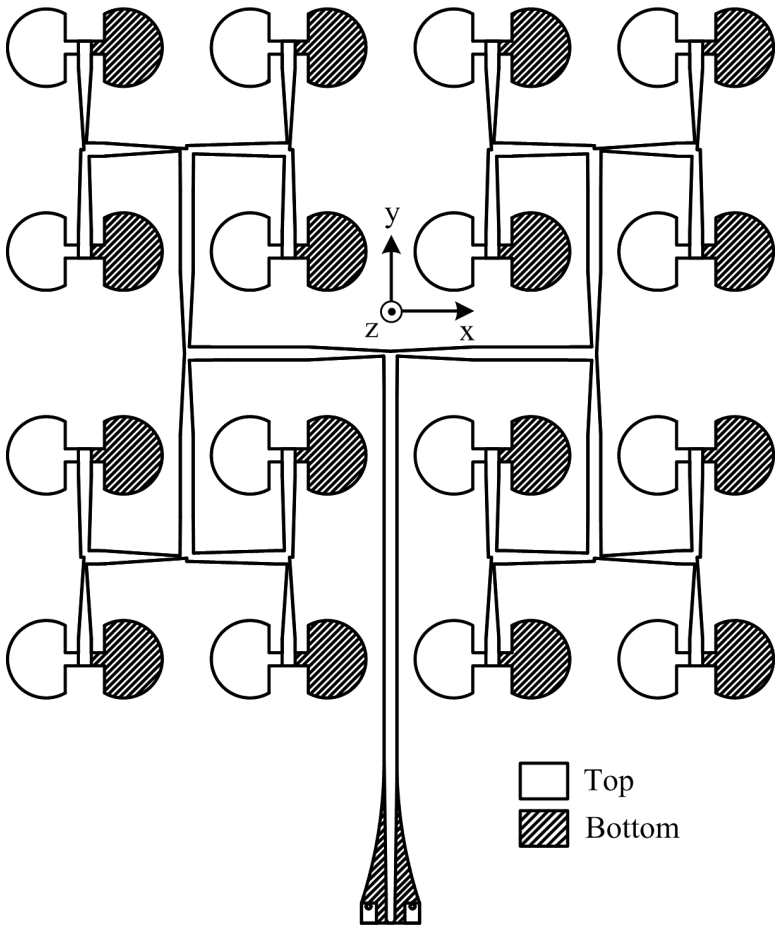

Fig. 40. The 4x4 array of radial dipole antennas with unequal and symmetrical power weighting.

Using modern array theory, the radiation pattern of an array can be found by multiplying the array factor by the element pattern [22]. King argued that this

approach is merely an approximation in [27] for antenna arrays that have mutual coupling among the elements. Since mutual coupling causes each element to have different current distributions, that means that each element will not radiate the same pattern, which is assumed in the calculation of the array factor. Even though the array factor does not provide the exact radiated field of the array when multiplied by the element pattern, it still provides insight into how the array operates so that improvements on the array may be made.

1. Array Factor

According to the equations for the array factor given in [22], the array factor for the 4x4 array with equal half-wavelength spacing and symmetrical weighting is given by Eq. 2.11,

$$AF = 2I_0 cos(\frac{3\pi\lambda_0 f}{2c} sin\theta) + 2I_1 cos(\frac{\pi\lambda_0 f}{2c} sin\theta) \tag{2.11}$$

where I_0 is the current given to the outer two elements in a four-element linear array, I_1 is the current given to the inner two elements, λ_0 is the wavelength for the half-wavelength spacing, f is the frequency of operation, c is the speed of light, and θ is the angle from the z-axis, as shown in Fig. 40.

Multiplying this array factor by the dipole element pattern shown previously shows that the array requires stronger power weighting in the y-z plane than in the x-z plane in order to have the same SLL in both planes. This prediction is verified by the higher measured SLL in the y-z direction than in the x-z direction that is discussed later. Since all four of the dipole element antennas described earlier in this work have the same radiation pattern between 2-4 GHz, an array of any of those

antennas requires stronger power weighting in the y-z plane to compensate for the increased element gain in that direction if low side-lobes are desired.

Since it is actually the power distribution that is determined by the power dividers in the array instead of the current distribution, the array factor multiplied by the element pattern cannot completely describe the SLL. The array factor suggests that the SLL is constant with respect to frequency, but measured and simulated radiation patterns show that the SLL actually varies with frequency.

2. Various Power Weighting Schemes

Four different equal-phase power weighting schemes are tested in the 4x4 array of dipole antennas. These four schemes are the equal-power, half-power, binomial, and half-power/binomial distribution schemes. The scheme that has equal power distributed to every element is called the "no weight" scheme, and the scheme that combines both half-power and binomial weighting is referred to as the "mixed" scheme.

An equal-magnitude scheme is implemented as a reference for the other schemes, which all include unequal power weighting. This "no weight" scheme does not include any of the tapered power dividers shown in Fig. 40 in order to illustrate the improvements in impedance matching that these dividers offer over an array without these power dividers. The equal-magnitude scheme allows the array to radiate with maximal gain (and maximal efficiency) since all elements are powered equally, and it also exhibits the largest side-lobes. For the sake of clarity, the power distribution among the elements in the "no weight" scheme is shown in Table VI.

A half-power scheme is used to show the effects of an array with moderate and symmetrical weighting. The half-power scheme uses the 2:1 power divider to give the central four elements maximal power, outer 8 elements half of that power, and corner elements one-fourth of the power provided to the central elements. In a uni-directional

4x4 array of patch antenna elements, Dr. Berndie Strassner showed experimentally that this power weighting scheme provided the array with a -30 dB SLL. It is implemented here to compare his result with the effects of this weighting scheme on a DSPSL-fed array of dipole elements. The power distribution among the elements in the half-power scheme is shown in Table VII.

Table VI. No Weight Power Distribution

Element	1	2	3	4
1	1	1	1	1
2	1	1	1	1
3	1	1	1	1
4	1	1	1	1

Table VII. Half Power Distribution

Element	1	2	3	4
1	1	2	2	1
2	2	4	4	2
3	2	4	4	2
4	1	2	2	1

According to array theory [22], the binomial current distribution among a linear array of equally spaced elements provides a total pattern that has a 0 dB SLL.

Although the binomial current distribution theoretically has a 0 dB SLL, it also has increased main beam width and reduced efficiency due to the higher current ratios among elements [9]. Since the currents could not be specifically assigned in this array due to the corporate-H feed network, a binomial power distribution was implemented instead. That binomial distribution is given in Table VIII.

Table VIII. Binomial Power Distribution

Element	1	2	3	4
1	1	3	3	1
2	3	9	9	3
3	3	9	9	3
4	1	3	3	1

Table IX. Mixed Power Distribution

Element	1	2	3	4
1	1	2	2	1
2	3	6	6	3
3	3	6	6	3
4	1	2	2	1

Since measured and simulated results for the half-power distribution showed that a stronger weighting was needed in the y-z plane to lower the SLL in that plane, the

mixed power distribution scheme was designed to leave everything else constant except for the weighting in the y-z plane. In the y-z direction, power is given to the elements with a binomial distribution, and in the x-z direction, the elements see a half-power distribution. The mixed power distribution is shown in Table IX.

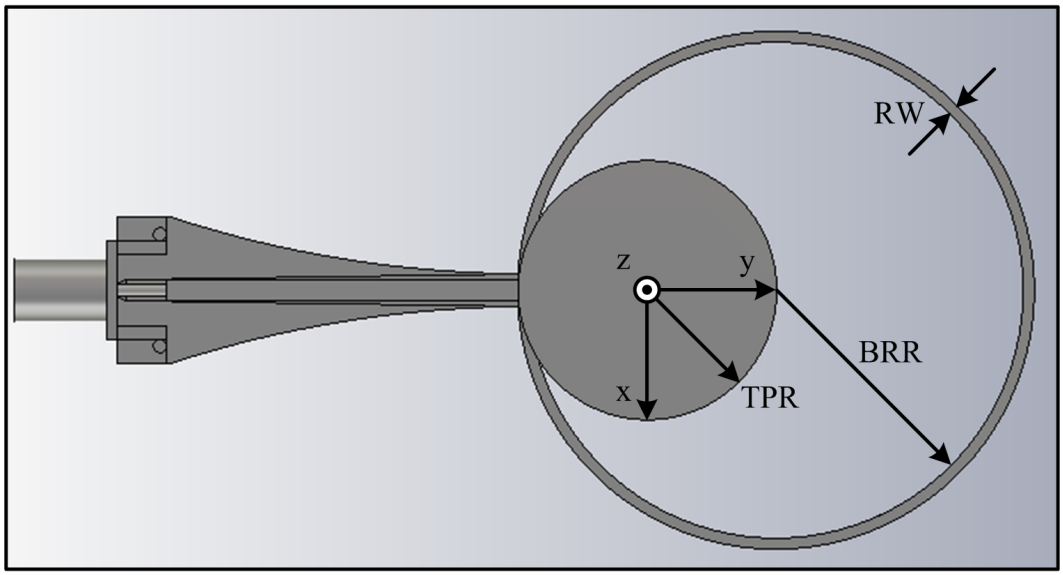

Fig. 41. DSPSL-fed circular monopole with dielectric hidden.

H. UWB DSPSL-fed Circular Monopole Antenna Design

In its lower range of operation (1-9 GHz), the DSPSL-fed circular monopole radiates omni-directionally like the antennas in [17–21], but in its higher range of operation (above 9 GHz with no visible upper limit), the described antenna radiates a monopulse

beam in the end-fire direction with a maximum gain that increases with frequency. Since radar tracking applications use monopulse beams to verify the target's location, this antenna's end-fire monopulse beam may be used for radar tracking in an array of scanned beams.

By cutting and bending the substrate containing the positive side of the monopole, the maximum gain of the lower frequency radiation might be shifted into the end-fire direction. If both the lower frequency and higher frequency radiation patterns have maximal gain in the same directions, then an array of these antenna elements would be able to verify a target's location with the focused lower-frequency beam and then error check this reading with the high-frequency monopulse beam. This theoretical array would not require a separate feed network to create a monopulse beam.

The design of the DSPSL-fed circular monopole is presented in Fig. 41 with the substrate hidden to illustrate the radiating aperture. The top patch radius (TPR) is 12.5 mm, the bottom ring radius (BRR) is 25.0 mm, the ring width (RW) is 1.08 mm, and the line width of the DSPSL line feeding the antenna is 3.15 mm, corresponding to a 50 Ω junction on 31-mil Rogers RT/duroid 5870 substrate ($\epsilon_r = 2.33$).

CHAPTER III

RESULTS

The measured and simulated data for the various previously discussed antennas are described in this section. The impedance bandwidths, radiation patterns, and radiation efficiencies are discussed for all of the designed antennas. Several other unique results are described for the relevant designed antennas, including the signal fidelity of the spiral antenna and the dependence of the SLL of the DSPSL-fed radial dipole array on the power weighting scheme used.

Since the spiral antenna radiates bi-directionally for its entire impedance bandwidth, the signal fidelity of an ultra-wideband pulse input into the spiral is calculated in order to quantitatively describe the transient output signal's distortion through the ultra-wideband frequency range. This quantitative analysis is not helpful for the DSPSL-fed array of dipoles because that array does not have an ultra-wideband impedance bandwidth. Although the DSPSL-fed planar monopole antenna has an ultra-wideband impedance bandwidth, it is not sensical to calculate the antenna's fidelity factor because the direction of the radiation of this antenna varies with frequency, preventing an ultra-wideband pulse from radiating out of the antenna to one receive location.

The SLL of the DSPSL-fed radial dipole array is reduced by increasing the power weighting in the direction that has a stronger element gain. The SLL is not discussed for the spiral antenna or the DSPSL-fed planar monopole because they are single elements whose radiation patterns are shown.

A. Final Spiral Antenna Performance

Since this antenna was designed with cascaded elements to create the final antenna, parametric analysis reduced the coupling between elements in the antenna as much as possible before construction began. After finishing such reductions in simulation, a complete antenna construction allowed for physical measurements that verified the simulated results. These measurements agree with the assumption that all elements could be designed individually and then cascaded together (with moderate parametric analysis for tuning).

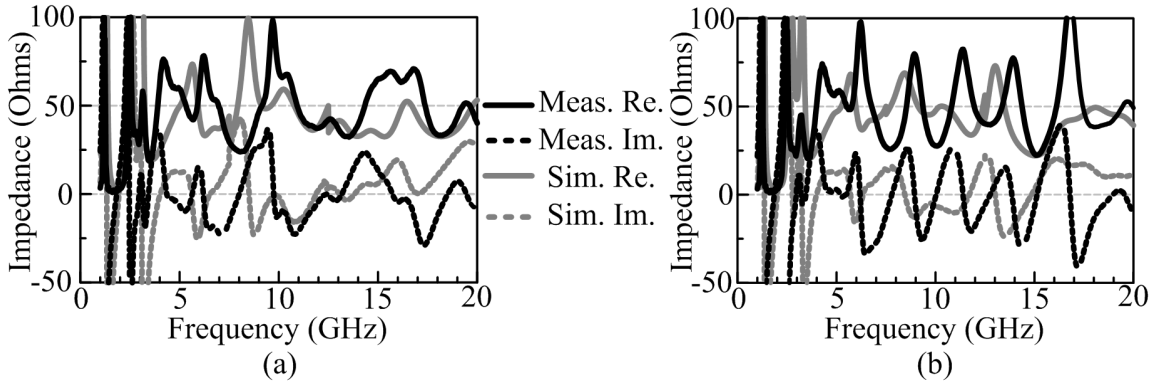

Fig. 42. Real and imaginary impedance versus frequency for the antenna (a) without etching holes and (b) with etching holes.

The antenna's spiral arms were truncated at a radius of 21 mm to limit the antenna's size and provide optimal impedance matching for the antenna. The remaining metal width between the etching holes and the outer spiral arms was set to 0.076 mm

since that value produced the best return loss parametrically. The tapered microstrip to tapered parallel-strip line that feeds the antenna is 30 mm long, and the total antenna dimensions are 59.94 mm x 59.94 mm x 1.14 mm.

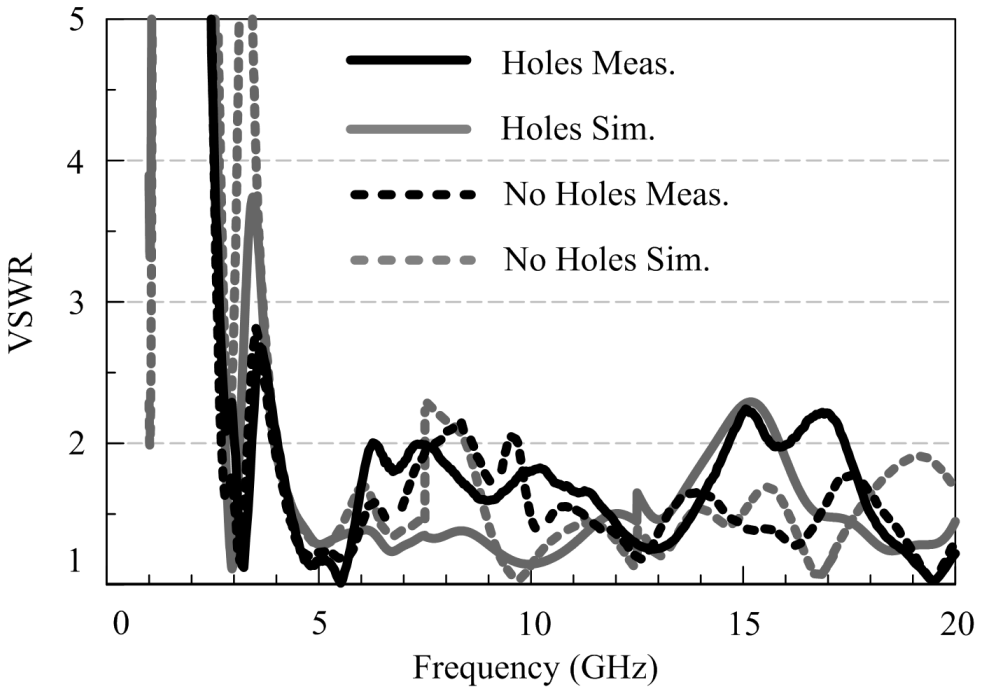

Fig. 43. VSWR plots for spiral antennas with and without etching holes.

The antenna's bandwidth is the unity between its impedance and radiation bandwidths. After determining the impedance bandwidth through network analyzer measurements and determining the radiation bandwidth through anechoic chamber measurements, the antenna with etching holes was found to have a bandwidth equal to

its impedance bandwidth. The input impedance of the two antennas and the VSWRs of those antennas are shown in Figs. 42-43, respectively.

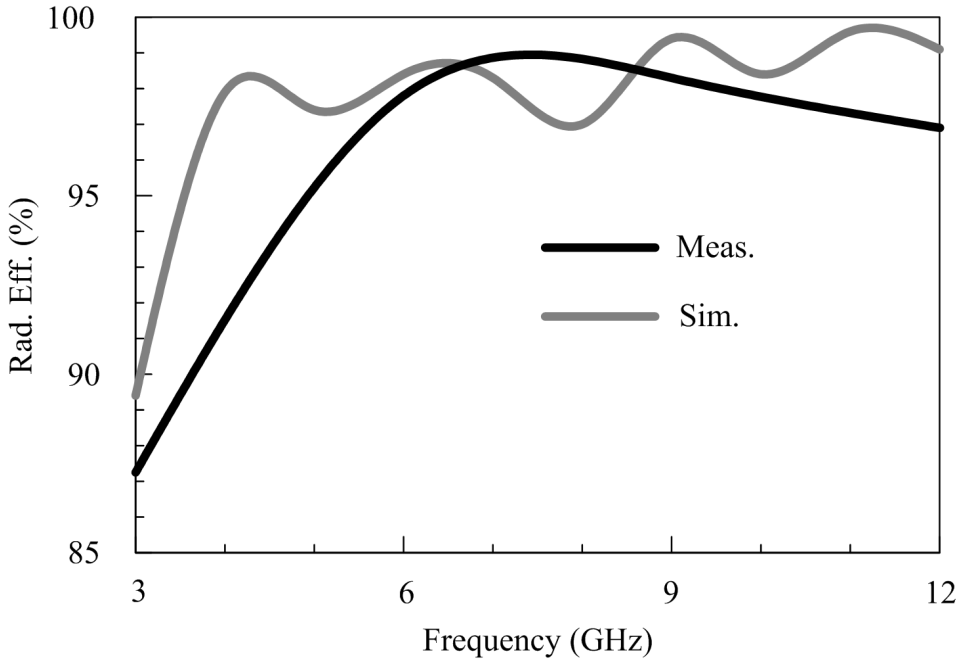

Fig. 44. Measured and simulated radiation efficiency of the antenna with etching holes over the 3-12 GHz range.

John Dyson showed that equiangular spirals could operate with a 98% radiation efficiency in the mid-1950's [1], and the designed antenna verifies his result in measurement and simulation. This antenna exhibits its lowest radiation efficiency of 87.3% at 3.0 GHz and its highest radiation efficiency of 98.9% at 7.4 GHz. Fig. 44 shows the radiation efficiency of the antenna with etching holes. The mean displacement

error of the measured radiation efficiency is ± 1.94%.

The radiation efficiency of the spiral was found by calculating the maximum effective aperture size and by measuring the gain. The radiation efficiency, gain, and maximum effective aperture size are related by Eq. 3.1 [13, 22, 28],

$$e_r = \frac{\lambda^2 G}{4\pi A_{em}} \tag{3.1}$$

where e_r is the radiation efficiency, λ is the wavelength of a specific frequency under consideration, G is the maximum measured gain, and A_{em} is the maximum effective aperture size.

Since an equiangular spiral with an arc length equal to λ has a lower operating frequency limit equal to c/λ [1], the maximum effective aperture of the equiangular spiral at its lower frequency limit is bound by a circle completely enclosing the spiral arc of length λ. The maximum effective aperture of the spiral decreases with increased frequency since the circle enclosing the arc of length λ decreases in size as the frequency increases.

The arc lengths corresponding to one wavelength at 3, 6, 9, and 12 GHz were calculated, and the radii of the circles enclosing those arcs were measured in order to find the maximum effective aperture at those frequencies. The arc lengths, enclosing circle radii, and maximum effective aperture areas at 3, 6, 9, and 12 GHz are given in Table X.

1. Impedance Bandwidth

In order to test the hypothesis that the etching holes in the spiral would improve the return loss of the antenna and thereby increase the impedance bandwidth, two spiral

antennas were constructed: one with etching holes, and one without etching holes. Fig. 42 shows the real and imaginary measured and simulated impedances for both antennas. The antenna with etching holes oscillates much more regularly around the point in the complex plane $50 + i0$, corresponding to a perfect match.

Table X. Spiral Antenna's Maximum Effective Aperture Area

Frequency (GHz)	Arc Length (mm)	Radius (mm)	A_{em} (mm^2)
3	100.0	30.0	2827.4
6	50.0	16.1	814.3
9	33.3	11.7	430.1
12	25.0	4.3	58.1

Typically the impedance bandwidth lies in the range of frequencies where the return loss remains better than 10 dB, which corresponds to a $1 \leq \text{VSWR} \leq 2$. Fig. 43 shows the VSWRs for the antennas with and without etching holes in measurement and simulation. The spiral antenna with holes exhibits a better VSWR than the spiral antenna without holes over the UWB range, and the simulated spiral with holes exhibits much lower loss than the fabricated spiral.

By observation, one can see that the theory of small reflections accurately predicted the lowest operating frequency limit for the antenna. Fig. 24 showed that the antenna could not operate effectively below 3 GHz, and the measured data in Fig. 43 confirmed that prediction.

The simulated VSWR for the antenna with etching holes remained less than 1.5 between 4-12 GHz while the measured VSWR rose to nearly 2 at 6 GHz and 7 GHz. This difference between measurement and simulation might be due to the etching resolution, as discussed previously. The small scale manipulation of solder under a microscope by hand poses another possible source of discrepancy between measured and simulated results.

Nonetheless, the measured VSWR of the antenna with etching holes shows 2:1 VSWR impedance bandwidths between 2.81-3.33 GHz and 3.95-14.80 GHz and a 3:1 VSWR impedance bandwidth between 3.33-3.95 GHz. The antenna without etching holes exhibits 2:1 VSWR impedance bandwidths between 4.00-7.75 GHz, 8.30-9.25 GHz, and 9.90-20.00 GHz and 3:1 VSWR impedance bandwidths elsewhere in the 3.00-9.90 GHz range. Therefore, etching holes into the spiral for the purpose of improving the return loss in the UWB band has succeeded.

2. Radiation Bandwidth

The frequency range in which an antenna radiates in a desirable way describes the radiation bandwidth of that antenna. Since different applications require different types of radiation, the radiation bandwidth of this antenna shall be defined as the frequency range over which this antenna exhibits bidirectional radiation with greater than or near unity gain in at least one polarization.

The spiral's radiation pattern rotates with changes in frequency since the distance between spiral arms increases with the angle of the spiral's rotation. Fig. 45 and Fig. 46 show the simulated and measured radiation patterns with the coordinate reference shown in Figs. 1-4. E_θ and E_ϕ are given for the designed antenna at 3 GHz, 6 GHz, 9 GHz, and 12 GHz at the planes $\phi = 0\,^\circ$ and $\phi = 90\,^\circ$. In all of these measurements, the gain of the spiral antenna remained above or near 0 dBi in bidirectional

broadside radiation with elliptical polarization. Therefore, the radiation pattern does not limit the bandwidth of the antenna in the UWB range (3.1-10.6 GHz).

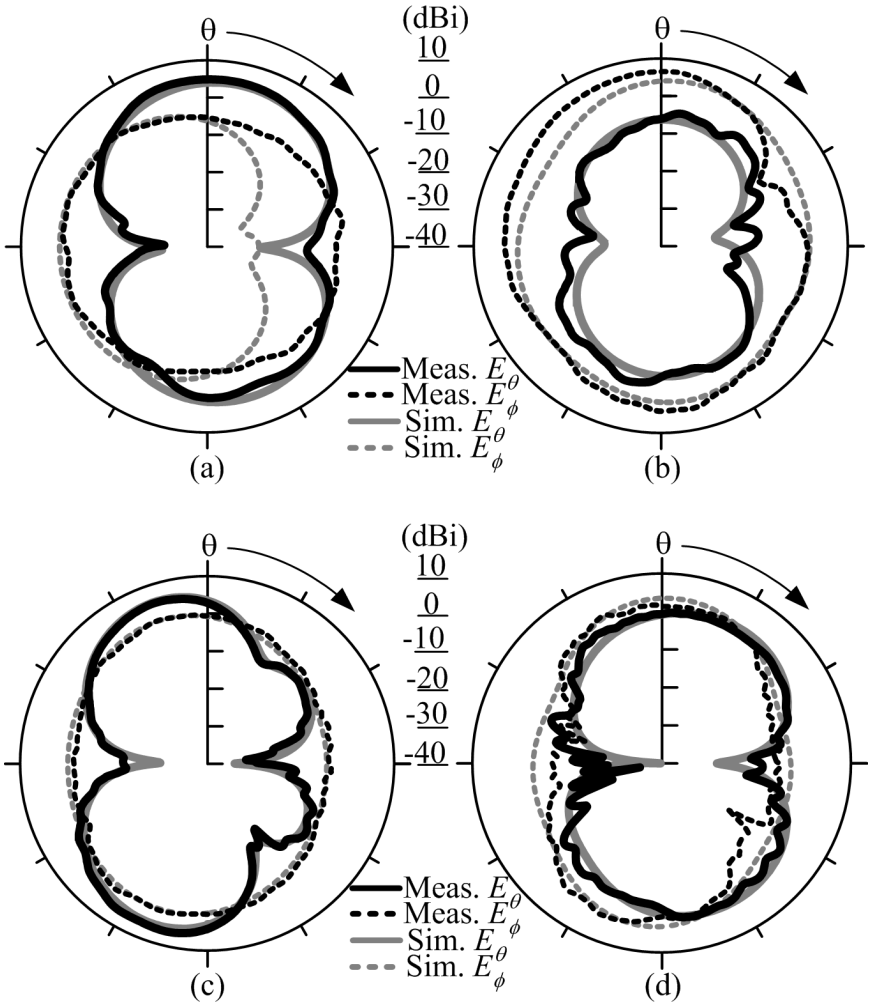

Fig. 45. Radiation patterns for the spiral antenna with measured gain shown in dBi. (a) 3 GHz and $\phi = 0\,^\circ$. (b) 3 GHz and $\phi = 90\,^\circ$. (c) 6 GHz and $\phi = 0\,^\circ$. (d) 6 GHz and $\phi = 90\,^\circ$.

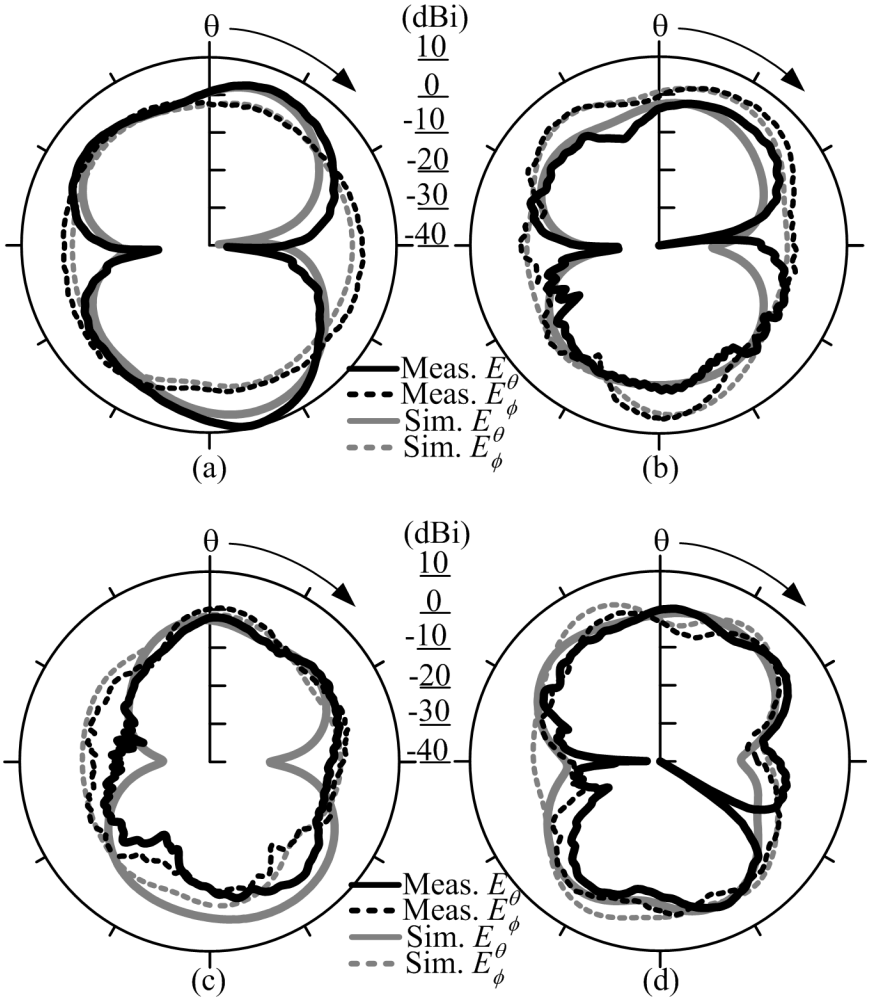

Fig. 46. Radiation patterns for the spiral antenna with measured gain shown in dBi. (a) 9 GHz and $\phi = 0\,^\circ$. (b) 9 GHz and $\phi = 90\,^\circ$. (c) 12 GHz and $\phi = 0\,^\circ$. (d) 12 GHz and $\phi = 90\,^\circ$.

Measurements showed that both a spiral with etching holes and a spiral without etching holes radiate the same patterns, so Fig. 45 and Fig. 46 only show the radiation

patterns of a spiral with holes. Since both spirals exhibit the same radiation patterns, the etching holes do not affect the radiation pattern of the spiral with holes through the measured UWB range.

Linear polarization is defined by an axial ratio of 10 dB or greater, elliptical polarization is defined by an axial ratio less than 10 dB and greater than 3 dB, and circular polarization is defined by an axial ratio less than 3 dB. For the entire UWB range, this antenna exhibits elliptical polarization. Fig. 47 shows the axial ratio for the spiral over the frequency range 3-12 GHz. The measured results for the axial ratio follow the general trend of the simulated results.

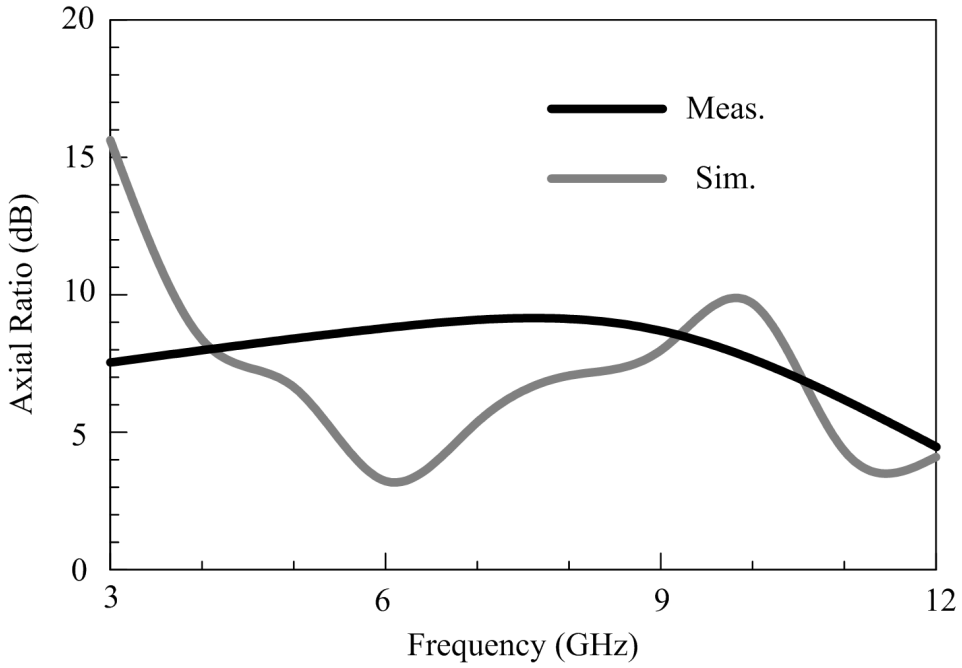

Fig. 47. The axial ratio for the spiral with etching holes. This antenna exhibits elliptical polarization from 3-12 GHz.

Since the radiation pattern does not limit the antenna's bandwidth in the UWB range, the impedance bandwidth imposes the only restriction on the antenna's bandwidth. The antenna's radiation shows good performance for all frequencies between 3-12 GHz. For the purpose of UWB communications, this antenna can radiate well over the entire UWB range.

3. Signal Distortion

Since the spiral receives and sends different frequency signals at different areas on the antenna, wideband signals undergo phase distortion by the time they are received or transmitted at the spiral's center feed points. Phase linearization techniques can be used to reduce this distortion [29].

The fidelity factor of an antenna measures the similarity between the transmitted and received signals in order to characterize the antenna's distortion [30–34]. An antenna with little distortion has a fidelity factor near unity. This factor F is calculated using Eq. 3.2 [30],

$$F = \max_{\tau} \frac{\int_{-\infty}^{\infty} S_t(t) S_r(t-\tau)\, dt}{\sqrt{\int_{-\infty}^{\infty} |S_t(t)|^2\, dt \cdot \int_{-\infty}^{\infty} |S_r(t)|^2\, dt}} \tag{3.2}$$

where $S_t(t)$ and $S_r(t)$ are the transmitted and received signals, respectively. The antenna under test was excited with a 0.5 ns UWB pulse to cover the frequency range 3-12 GHz. Since the antenna's feed structure is asymmetrical, which may cause some antennas to have an unbalanced phase center, the same excitation was given to a spiral that had a dummy feed on the opposite side of the actual feed and symmetrical hole modifications on both sides of the spiral.

The excitation and far-field received signals for both spirals are plotted together

in Fig. 48. The far-field of the spiral is defined here as the distance exceeding $2D^2/\lambda$, where D is the maximum dimension of the antenna's aperture, and λ is the wavelength of the lowest operating frequency [22]. For this antenna, the far-field exists at a distance exceeding 72 mm, and the signals were received at 73 mm. The fidelity factor for both spirals is given in Table XI.

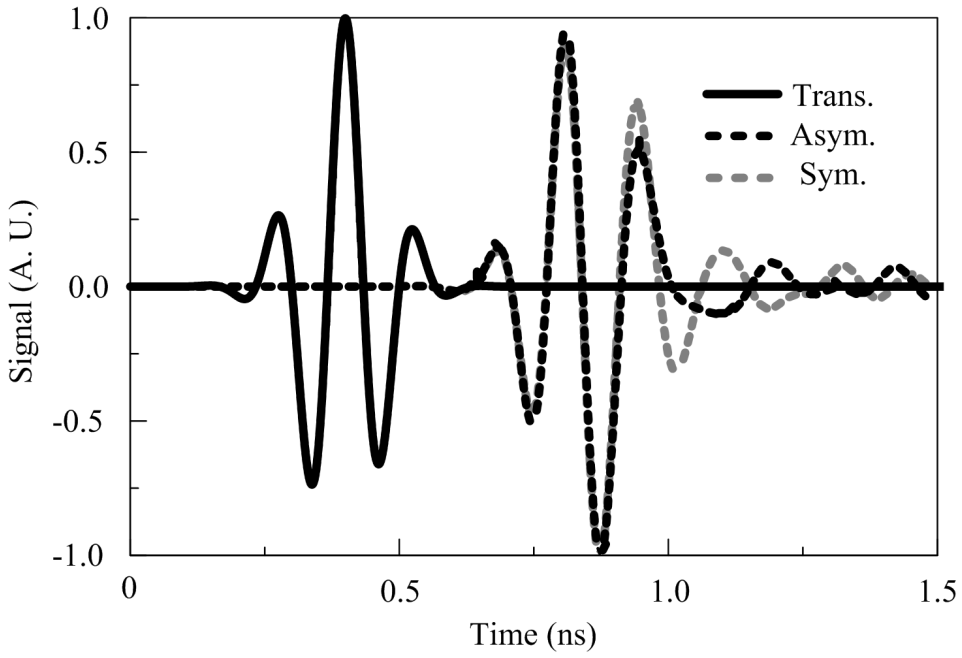

Fig. 48. The transmitted signal for both spirals (Trans.), received signal from the asymmetrical spiral (Asym.), and received signal from the symmetrical spiral (Sym.).

As seen in Table XI, the asymmetric spiral described in this paper has a higher fidelity factor than a similar spiral with a dummy feed and symmetrically placed

etching holes. The asymmetric spiral emits a high-fidelity signal in the UWB range, which shows that it would be a good candidate for use in UWB applications.

Table XI. Asymmetric and Symmetric Spiral Fidelity Factor Comparison

Antenna	Fidelity Factor
Asym. Spiral	0.939
Sym. Spiral	0.897

B. DSPSL-fed Radial Dipole Array Performance

A hypothesis was proposed that stronger weighting in the y-z plane would reduce the SLL of the 4x4 dipole array in that plane, and the hypothesis was confirmed with both the binomial power distribution and the mixed power distribution. Interestingly, both the binomial power distribution and the mixed power distribution had a higher SLL than the half-power distribution in the x-z plane while having equal or stronger weighting in that plane.

Unlike Dr. Berndie Strassner's experimental results that showed -30 dB SLLs for the 4x4 patch antenna array with a half-power distribution, the half-power distribution for the 4x4 array of dipole antennas had a -24.5 dB SLL in the x-z plane and a -16.4 dB SLL in the y-z plane. Possible causes for the differences between Strassner's experimental results and the ones shown in this paper arise from the differences in

antenna element radiation patterns (uni-directional patch vs. bi-directional dipole), mutual coupling between differing elements, and different power divider characteristics (stripline vs. DSPSL).

Even though the "no weight" scheme did not possess any impedance transforming sections in its array, it still had a non-zero 2:1 VSWR bandwidth near 3.00 GHz. However, this scheme possessed the highest SLL out of all the distributions, making it the least likely choice for directional applications.

In Dolph's model of the antenna array, he optimized the SLL such that it could be specified and made minimally flat by choosing the appropriate current distribution. In this case, the SLL was optimized by modifying the power distributions in the array until the best SLL was achieved with usable bandwidth and moderate radiation efficiency. The mixed power weighting scheme provided the DSPSL 4x4 dipole array with the second lowest SLL in the $\phi = 0°$ plane and the lowest SLL in the $\phi = 90°$ plane while maintaining a 73.2% radiation efficiency and the largest impedance bandwidth out of all four tested power distributions. Therefore, the mixed power distribution is the optimal choice among all four of the tested power distributions.

1. Radiation Pattern Versus Frequency

The simulated fields were taken from CST Microwave Studio simulations. These simulated fields have good agreement with the measured fields, which are shown together with the simulated fields in Figs. 49-50. The radiated and simulated fields show that minimal power is radiated in the side-lobes at 3.05 GHz.

Since the element pattern and array factor do not show SLL variation with frequency, it can be assumed that the SLL variation either arises from mutual coupling effects between the elements (as King described in [27]) or from the phase variations with frequency in the feed network. These phase variations do not alter the relation-

ship between the voltage and the current, but they would alter the magnitudes of the voltages and currents delivered at the elements based on the operating frequency.

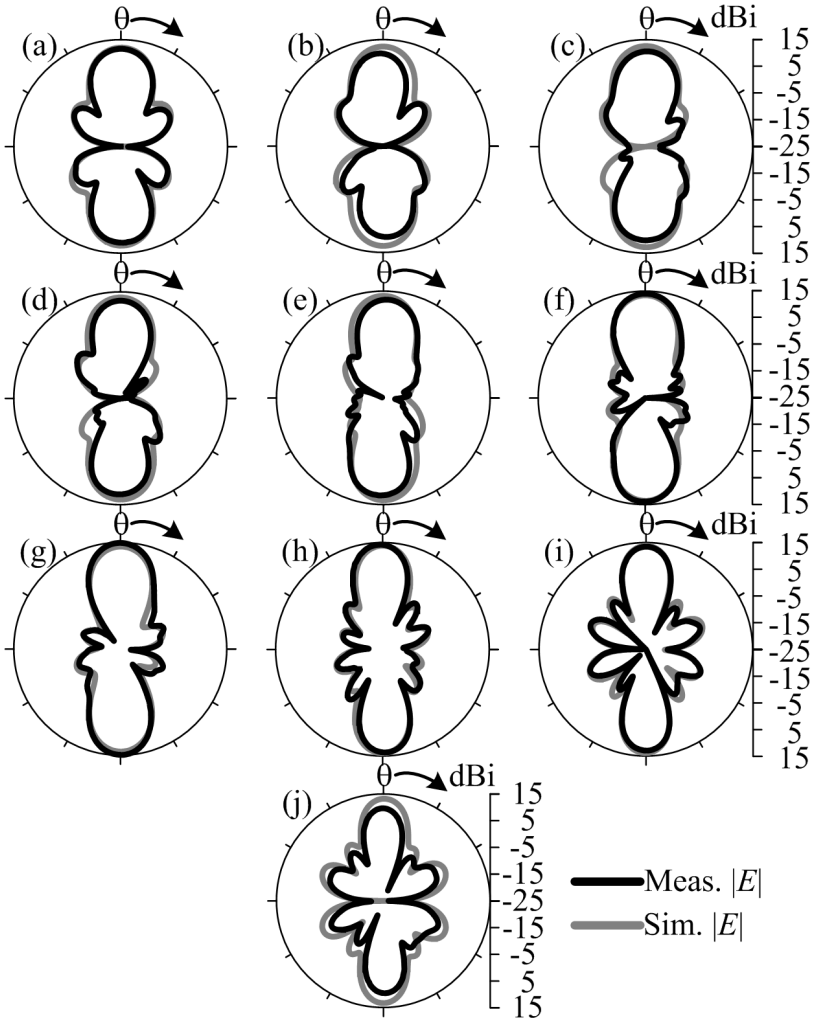

Fig. 49. Measured and simulated $|E|$ field versus θ angle in the $\phi = 0°$ plane for the half-power distribution at (a) 2.55 GHz, (b) 2.65 GHz, (c) 2.75 GHz, (d) 2.85 GHz, (e) 2.95 GHz, (f) 3.05 GHz, (g) 3.15 GHz, (h) 3.25 GHz, (i) 3.35 GHz, (j) 3.45 GHz.

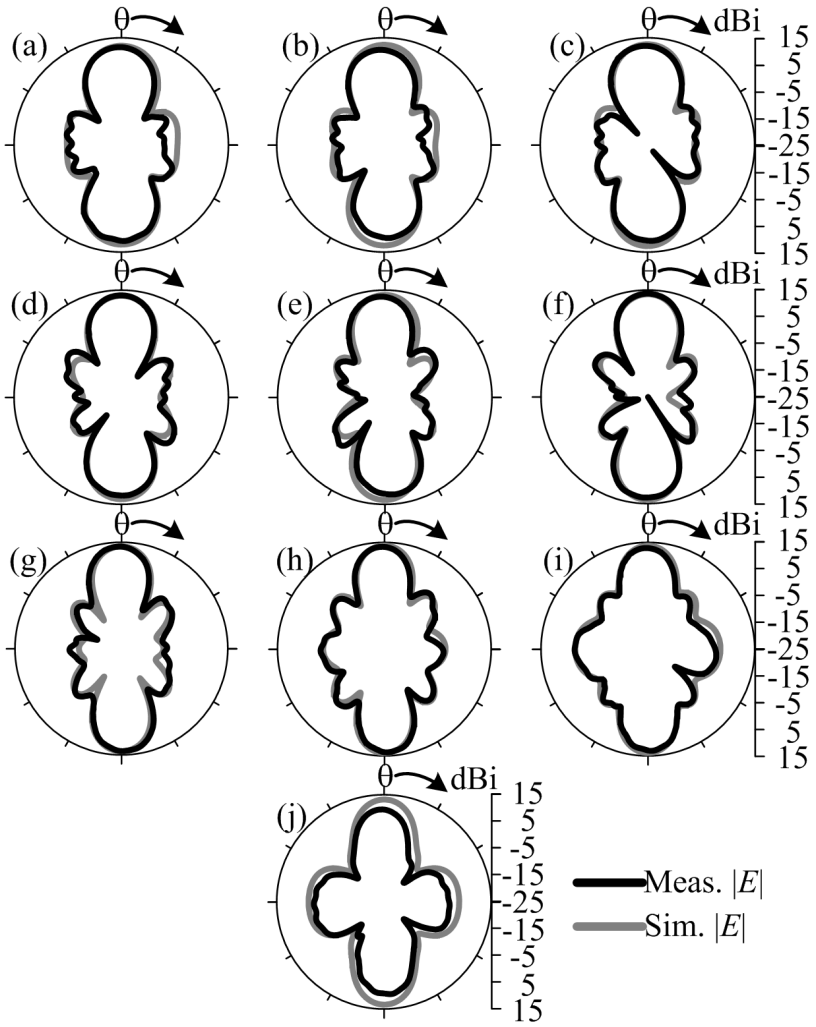

Fig. 50. Measured and simulated $|E|$ field versus θ angle for in the $\phi = 90°$ plane for the half-power distribution at (a) 2.55 GHz, (b) 2.65 GHz, (c) 2.75 GHz, (d) 2.85 GHz, (e) 2.95 GHz, (f) 3.05 GHz, (g) 3.15 GHz, (h) 3.25 GHz, (i) 3.35 GHz, (j) 3.45 GHz.

Regardless of the specific cause of the SLL variation, 2:1 and 3:1 power dividers have been designed for the array to create half-power and binomial distributions in

the array without changing the phase relationships between elements or their mutual coupling effects. Therefore the SLL remains minimal at 3.05 GHz for variations in equal-phase power dividers.

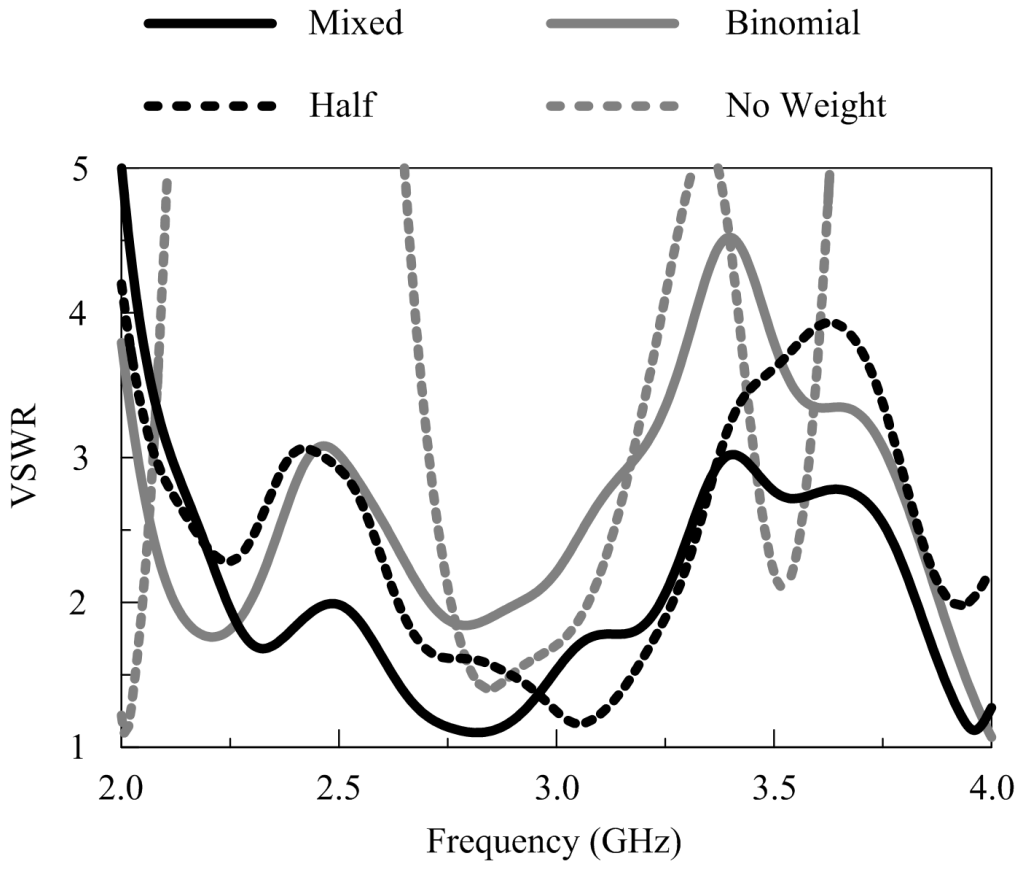

Fig. 51. VSWRs of the 4x4 radial dipole array for four different power weighting schemes.

Improvements upon the array's SLL with these dividers apply for an array with

any of the elements described earlier because all of those elements have the same radiation pattern (and therefore the same coupling). In this way, the SLL improvements for the 4x4 radial dipole array generally apply for any array of dipoles oriented in the same polarization as the dipoles in Fig. 40. In order to provide unequal powers to the various antennas for SLL improvement, a DSPSL unequal power divider is required.

2. Weighting Effects on the Impedance Bandwidth

The arrays with "no weight", half-power, binomial, and mixed distributions have 310 MHz, 630 MHz, 220 MHz, and 990 MHz 2:1 VSWR impedance bandwidths near 3.00 GHz, respectively. The binomial array has the smallest 2:1 VSWR bandwidth, and the mixed array has the largest 2:1 VSWR bandwidth. These VSWRs are shown together in Fig. 51.

Table XII. Weighting Effects on the Radial Dipole Array's Side-lobe Level

	E_θ for $\phi = 0°$ (dB)	E_ϕ for $\phi = 90°$ (dB)
No Weight	-16.1	-10.1
Half-Power	-24.5	-16.4
Binomial	-22.0	-20.4
Mixed	-23.4	-20.6

3. Weighting Effects on the Side-lobe Level

The dipole array's polarization in the $\phi = 0°$ plane is in the direction of the E_θ field, and its polarization in the $\phi = 90°$ plane is in the direction of the E_ϕ field. The SLLs for these polarizations are shown in Table XII, and the radiated fields in those polarizations are plotted in Figs. 52-53.

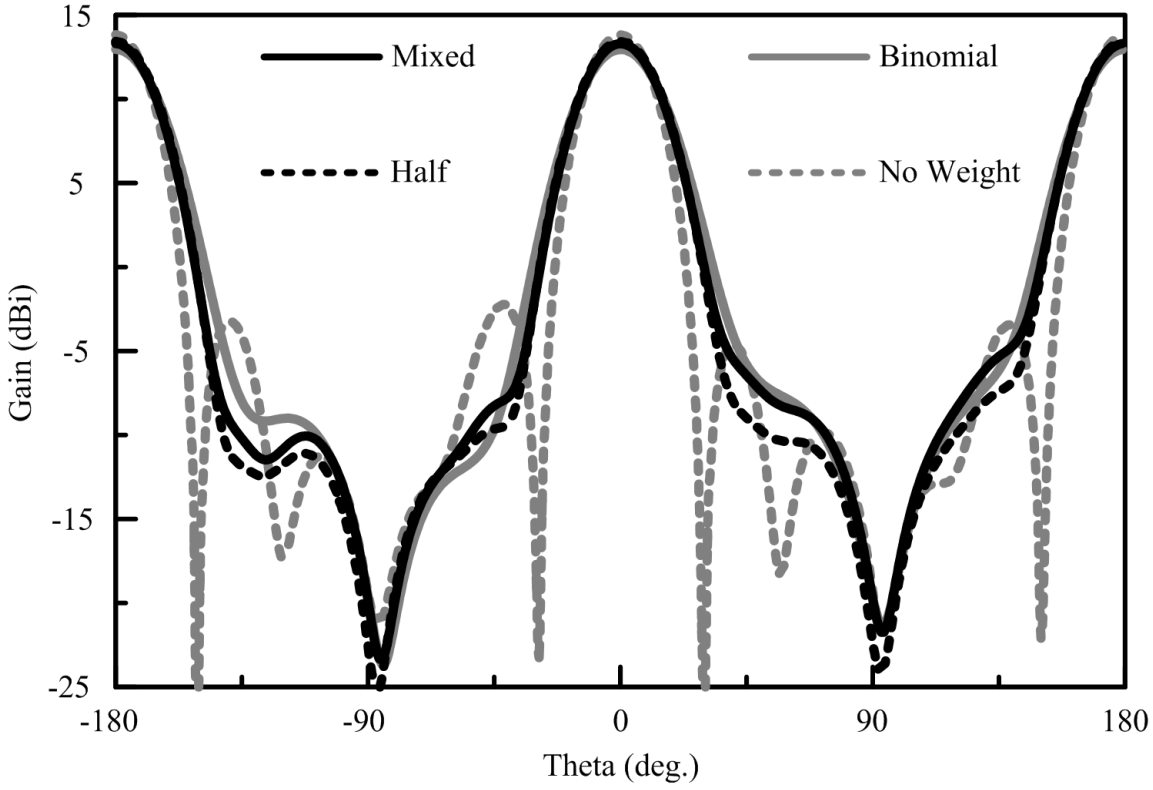

Fig. 52. Radiated $|E_\theta|$ patterns for the various weighting schemes at 3.05 GHz in the $\phi = 0°$ plane for varying degrees of θ.

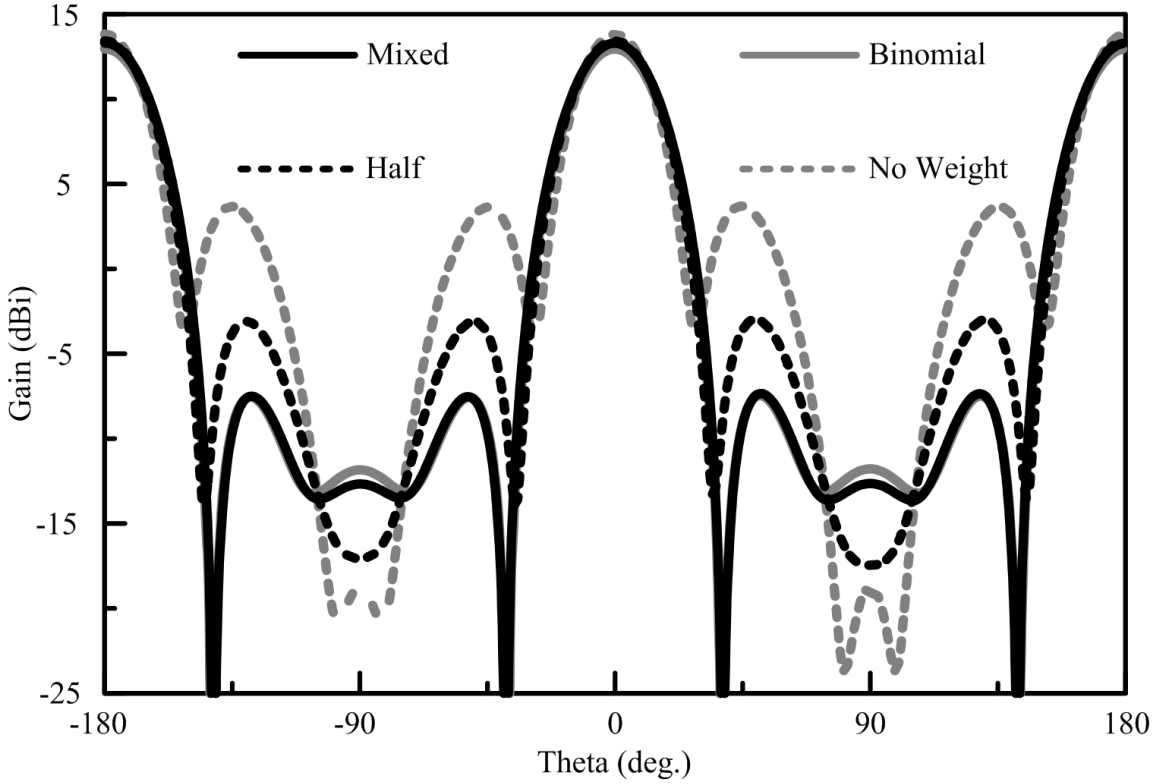

Fig. 53. Radiated $|E_\phi|$ patterns for the various weighting schemes at 3.05 GHz in the $\phi = 90°$ plane for varying degrees of θ.

The minimal SLL is achieved in the E_θ polarization in the $\phi = 0°$ plane for the half-power weighting scheme, but the SLL of the half-power weighting scheme in the $\phi = 90°$ plane is 8.1 dB worse than in the $\phi = 0°$ plane. The binomial and mixed weighting schemes decrease the SLL in the $\phi = 90°$ plane by 4.0 dB and 4.2 dB relative to the half-power distribution's SLL, respectively, and they suffer 2.5 dB and 1.1 dB increases for the SLL in the $\phi = 0°$ plane, respectively and relative to the half-power distribution's minimal SLL. The E_ϕ fields in the $\phi = 0°$ plane and the E_θ

fields in the $\phi = 90°$ plane do not contribute significantly to the SLL of the various arrays since the radial dipole used has a strong linear polarization.

The results show both predicted and unpredicted relative SLLs for the various distributions. The "no weight" distribution achieved the worst SLL in both planes, as was predicted. The binomial power distribution did not have a 0 dB SLL as theory predicts for a binomial current distribution, but it could not be expected to operate exactly like the binomial current distribution, considering that the binomial power distribution arranges power levels and not currents. The mixed power distribution's SLLs were better than the binomial distribution's SLLs in both planes, which was also unpredicted.

Table XIII. Gain and Efficiency for the Radial Dipole Array

	Maximum Gain (dB)	Radiation Efficiency (%)
No Weight	13.8	82.1
Half-Power	13.4	74.9
Binomial	13.0	68.3
Mixed	13.3	73.2

4. Weighting Effects on the Radiation Efficiency

The radiation efficiency was calculated based on Eq. 3.1 [13, 22, 28], which relates the maximum gain in Table XIII and the maximum effective aperture area to the radiation

efficiency. The maximum effective aperture area is given by $A_{em} = (3/2\lambda_0)^2$, which covers the array's face for a 16 element array with half-wavelength spacing. The "no weight" power distribution achieved the highest radiation efficiency at 82.1%, and the binomial power distribution had the lowest efficiency at 68.3%.

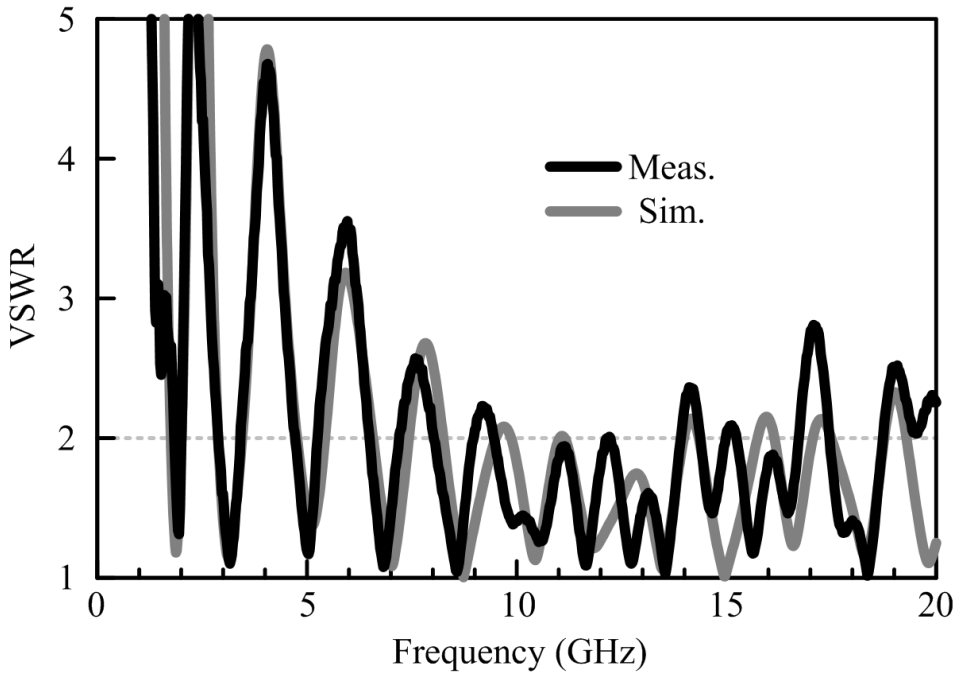

Fig. 54. Measured and simulated VSWR of the DSPSL-fed circular monopole antenna.

C. UWB DSPSL-fed Circular Monopole Antenna Performance

This section presents the impedance bandwidth, radiation patterns, and efficiency of the DSPSL-fed circular monopole antenna. Although the circular monopole antenna

radiates efficiently over most of the UWB spectrum, the continuous bandwidth of the antenna is limited by the impedance bandwidth and the direction of the radiation. At frequencies where the antenna is not well matched, the total efficiency is low even though the radiation efficiency may be high.

The radiation pattern shifts from a bi-directional broadside beam near 5 GHz to a monopulse beam at and above 10 GHz. Since the beam direction is not constant with frequency, the antenna's application must either be suited to its shifting beam direction or the antenna must only be used in narrow bandwidths.

1. Impedance Bandwidth

The VSWR of the DSPSL-fed circular monopole is shown in Fig. 54 from 1-20 GHz. Below 9.0 GHz, the 2:1 VSWR bandwidth is periodic, from 9.5-14.0 GHz the 2:1 VSWR bandwidth is continuous, and above 14.0 GHz the 2:1 VSWR bandwidth is a mixture of periodic and continuous. The 3:1 VSWR bandwidth is continuous from 6.5-20 GHz.

The VSWR first drops below 2 at slightly less than 2 GHz due to the modal resonance of the ring on the bottom of the antenna. The ring has a radius of 25 mm, corresponding to a circumference of 157 mm. The frequency 1.91 GHz has a wavelength of 157 mm also, and Fig. 54 shows the first 2:1 VSWR frequency near 1.9 GHz.

Since this first impedance match is caused by modal resonance in the bottom ring, it seems reasonable to expect that higher frequency impedance matches would occur at multiples of this frequency. The waves corresponding to 3.8, 5.7, 7.6, and 9.6 GHz have the same node positions as the wave corresponding to 1.9 GHz because these frequencies are the first five multiples of 1.9 GHz. Although these higher frequencies share the same nodes as 1.9 GHz, the measured higher order resonances occur at slightly lower frequencies. Fig. 54 shows higher order resonances occurring at 3.1, 5.0, 6.9, and 8.5 GHz.

The top ring has a radius of 12.5 mm, which is exactly half of the radius of the bottom ring. Therefore, the circumference of the top ring is half of the circumference of the bottom ring, and the top ring should also resonate at the same frequencies as the bottom ring, excluding the primary resonance at 1.9 GHz.

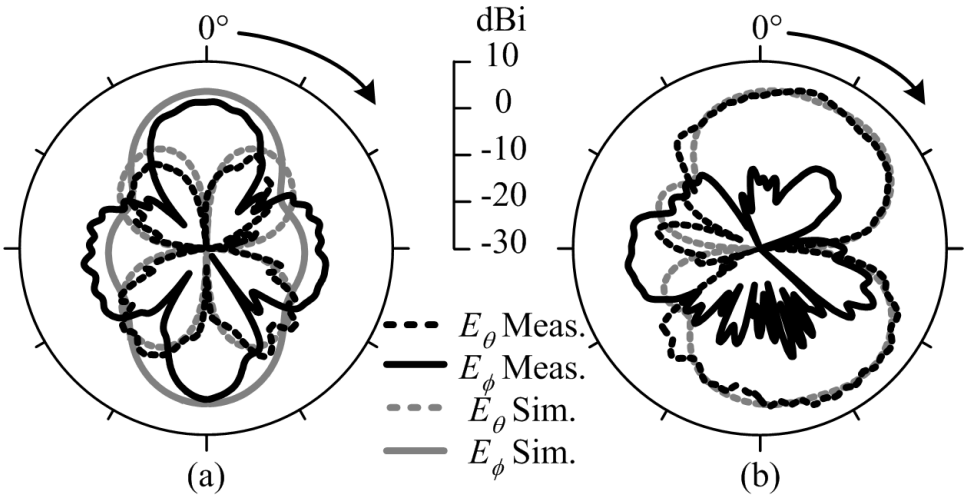

Fig. 55. Measured and simulated radiation patterns versus θ angle for E_θ and E_ϕ at (a) $\phi = 0°$ and (b) $\phi = 90°$ at 5.0 GHz.

2. Radiation Pattern

Figs. 55-56 show the radiation patterns of the DSPSL-fed circular monopole at 5.0 and 10.0 GHz, respectively. At 5.0 GHz, the monopole radiates omni-directionally in the $x - z$ plane and tri-directionally in the $y - z$ plane with a maximum gain of 5.5 dBi. At 10.0 GHz, the monopole radiates a monopulse beam in the end-fire

direction ($\theta = 90°, \phi = 90°$) with a maximum gain of 6.7 dBi.

With some structural modifications to the DSPSL-fed circular monopole, it may be possible to direct the maximal gain of the antenna at lower frequencies into the end-fire direction. This would allow the antenna to verify a target's location with directive and monopulse beams at two respective frequencies for radar and tracking.

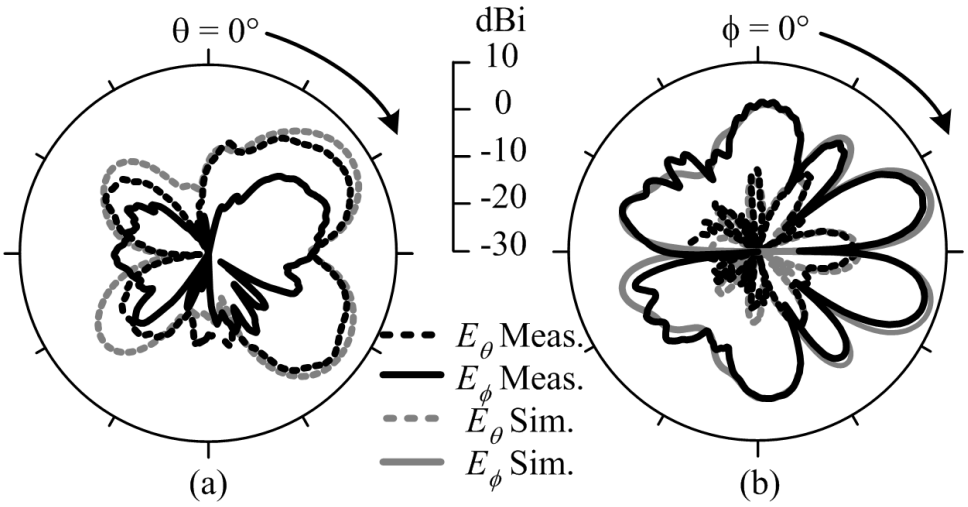

Fig. 56. Measured and simulated radiation patterns in E_θ and E_ϕ versus θ angle for (a) $\phi = 90°$ and versus ϕ angle for (b) $\theta = 90°$ at 10.0 GHz.

3. Efficiency

The radiation efficiency of the circular monopole antenna is calculated using Eq. 3.1 at 5 and 10 GHz, where the radiation patterns were measured. The maximum effective aperture area for the bi-directional broadside radiation at 5 GHz is the area enclosed

by the bottom ring, which is 1963 mm^2. The maximum effective aperture area for the monopulse beam at 10 GHz is harder to determine because the monopulse beam radiates perpendicularly to the two-dimensional antenna's face. For the purpose of not accidentally inflating the calculated efficiency levels, the same maximum effective aperture size that was used for the bi-directional broadside beam is also used for the monopulse beam even though the monopulse beam radiates perpendicularly to the measured aperture. At 5 GHz, the wavelength is 60 mm, and the maximum gain is 3.55 (ratio). At 10 GHz, the wavelength is 30 mm, and the maximum gain is 4.68 (ratio). The calculated efficiencies for these frequencies are shown in Table XIV.

Table XIV. DSPSL-fed Circular Monopole Antenna's Radiation Efficiency

Frequency (GHz)	Max. Gain (dB)	A_{em} mm^2	Rad. Efficiency (%)
5	5.5	1963	51.8
10	6.7	1963	17.1

The antenna's low radiation efficiency at 5 GHz shows that this antenna is physically large compared to the 5 GHz wavelength. Since this frequency corresponds to the third harmonic resonance, low radiation efficiency can be expected because the 1.9 GHz wavelength is 2.6 times larger than the 5 GHz wavelength.

In order to more efficiently receive a planar wave at 5 GHz with an array of these elements, the elements could be stacked and offset from one another in a three-dimensional grid such that the radiating components of the elements cover the array's

two-dimensional receiving aperture.

The low radiation efficiency at 10 GHz is really an underestimation of the antenna's efficiency at this frequency. The maximum effective aperture area used to calculate this efficiency is perpendicular to the radiating aperture at 10 GHz, which shows that the area used for this calculation is only a best guess. However, the two-dimensional antenna has a very small surface area in the monopulse beam's direction, and the maximum effective area for this beam's radiation could not be measured because it is not a physical area. Therefore the antenna's maximum dimensions were used as the maximum effective area because that is the maximum area that could possibly be affecting the monopulse radiation.

CHAPTER IV

COMPARATIVE ANALYSIS

This chapter describes the improvements of the designed antennas and circuits over existing technology by illustrating the differences between the new ideas and older ones. The six sections of this chapter correspond to the six basic new ideas that were introduced in this dissertation.

A. Spiral Antenna Comparisons

In this section, the spiral antenna designs and results from [1, 3–5, 7] are briefly summarized and compared with the planar side-fed spiral designed for this dissertation. The new spiral presented in this dissertation improves upon these older designs by reducing the volume and weight required for the spiral and its feed while maintaining an ultra-wideband impedance and radiation bandwidth.

1. Coaxially-fed Equiangular Slot Spiral

Dyson designed an equiangular slot spiral antenna fed from the center with a coaxial cable. He wrapped the coaxial feed line in such a way that it followed the metal layer of the spiral as shown in Fig. 57. He also added a dummy coaxial line to the other metal arm to prevent an asymmetrical beam from forming. Adding the dummy coaxial line has the greatest effect in maintaining symmetrical beam formation for his spiral when the thickness of the coaxial cable approaches the thickness of the metal on which it sits [1]. As shown in Fig. 57, Dyson designed his slot spiral with three different thicknesses of coaxial cable to ensure that the spiral's radiation would be unchanged by the thickness of the coaxial line used.

The PPPC-fed spiral designed in this dissertation reduces the volume and weight

required by the feed by using a parallel-strip line beneath the spiral instead of a coaxial line. The substrate that holds the parallel-strip line is only 0.5 mm thick, while 50 Ω RG standard coaxial lines can vary from 2.6 mm (RG-174/U) to 22 mm (RG-218) in diameter.

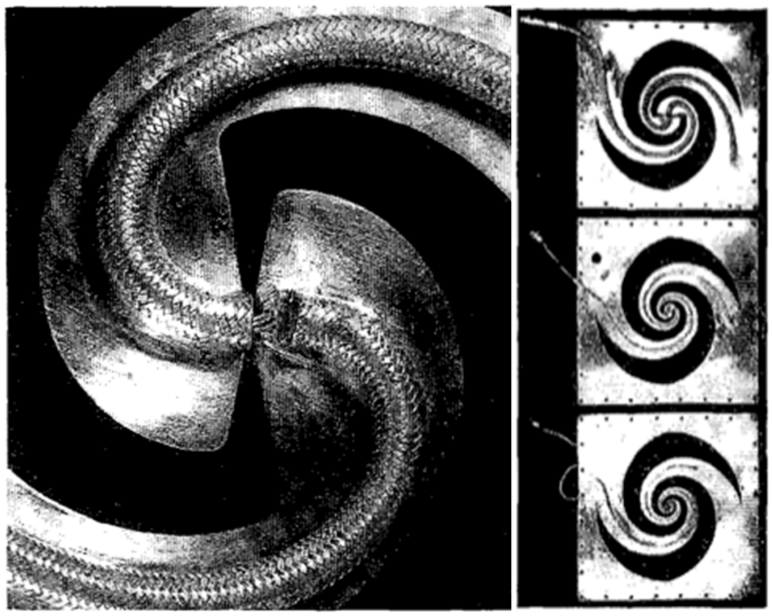

Fig. 57. Dyson's slot spiral antenna fed by three coaxial lines of differing widths.

Since the PPPC-fed spiral is not a slot spiral, it does not require the extra metal surrounding the spiral shown in Fig. 57. Dyson's metal layer had to be thick enough to mechanically support a mounted coaxial cable, which forced the extra metal surrounding the spiral to add additional weight to the antenna.

Dyson's spiral has a 2:1 VSWR impedance bandwidth ranging from 0.65 GHz to

at least 10 GHz, as shown in Fig. 58. He achieved such a high impedance bandwidth by using an arm length of 42 cm. Since the PPPC-fed spiral antenna was designed for the UWB range (3.1-10.6) GHz, the arm length of the PPPC-fed spiral extends to only 10 cm.

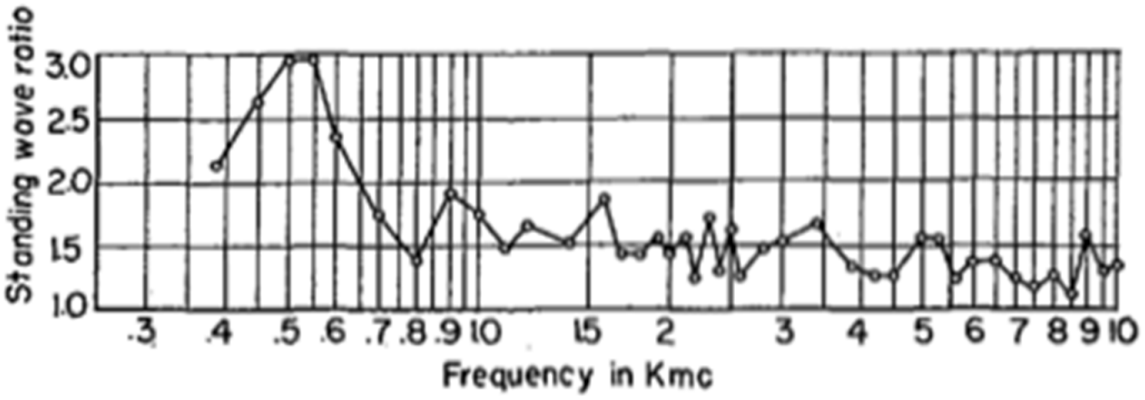

Fig. 58. The VSWR of Dyson's slot spiral from 0.4 to 10 GHz.

The radiation from Dyson's spiral exhibits circular polarization from 0.5 to 12 GHz with no tilt in the main beam direction. The PPPC-fed spiral exhibits elliptical polarization from 3 to 12 GHz with minimal beam tilting. Dyson's spiral radiates bi-directionally with only one hemisphere shown in Fig. 59.

The minimal variation in the broadside gain between the $\phi = 0°$ and $\phi = 90°$ patterns at each frequency results from Dyson's spiral's rotational symmetry. Since the PPPC-fed spiral is not rotationally symmetric (due to the DSPSL feed that passes underneath the spiral), the $\phi = 0°$ and $\phi = 90°$ patterns from 3-12 GHz

shown in Figs. 45-46 show greater variation between their E_θ and E_ϕ patterns. For this reason, the PPPC-fed spiral exhibits elliptical polarization over the FCC allotted UWB spectrum.

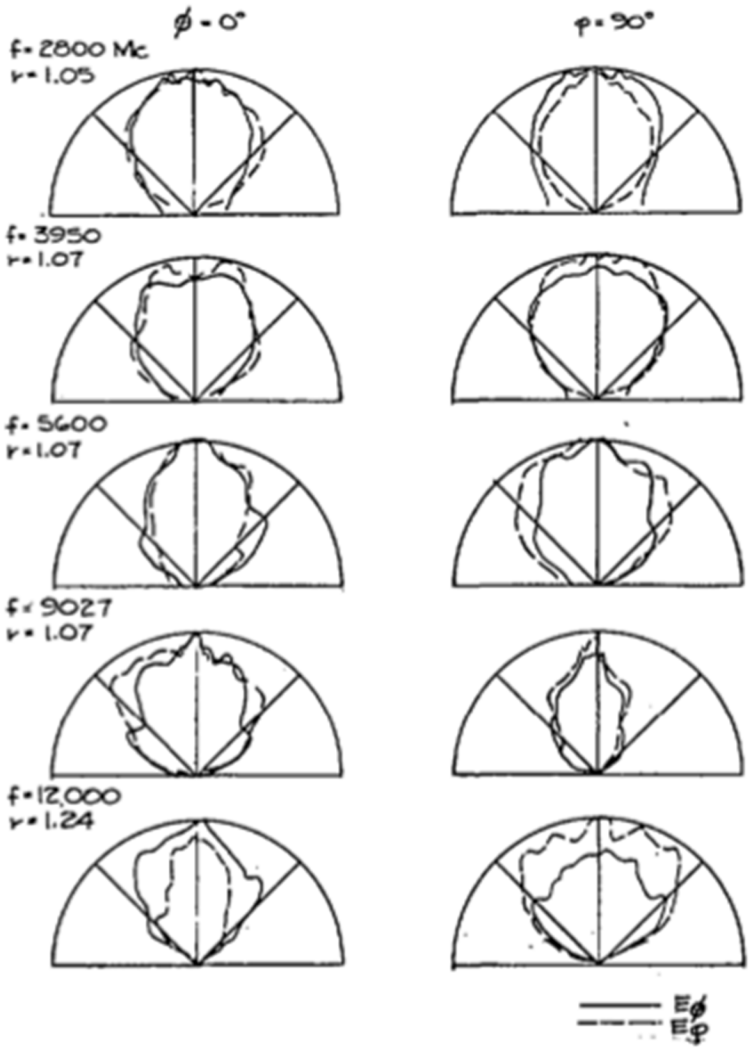

Fig. 59. Radiation patterns in E_θ and E_ϕ for Dyson's slot spiral from 2.8 to 12 GHz.

2. Co-planar Strip Line-fed Equiangular Spiral

Tu designed an equiangular spiral antenna perpendicularly fed by co-planar strip line [7]. Fig. 60 shows the design of his spiral antenna, where the black section represents the metal of the antenna's surface.

Fig. 60. Tu's spiral antenna fed perpendicularly by co-planar strip line.

Since Tu's spiral requires a perpendicular feed, it effectively occupies the cylindrical volume defined by the spiral's diameter and the length of the perpendicular feed, which takes effectively the same volume as a soda can. It also requires mechanical stabilizers near the center of the spiral to hold the perpendicular feed flush against the spiral at a 90° degree angle. This mechanical arrangement does not allow this antenna to be used in portable technology such as laptops or cell phones because

it takes up too much volume and does not possess enough mechanical stability to survive normal wear and tear.

The PPPC-fed spiral presented in this dissertation allows the spiral antenna to fit inside the volume occupied by a paper matchbook. This volume could easily be integrated into existing portable technology, and the spiral's design possesses enough mechanical rigidity that it could survive being dropped or stepped on.

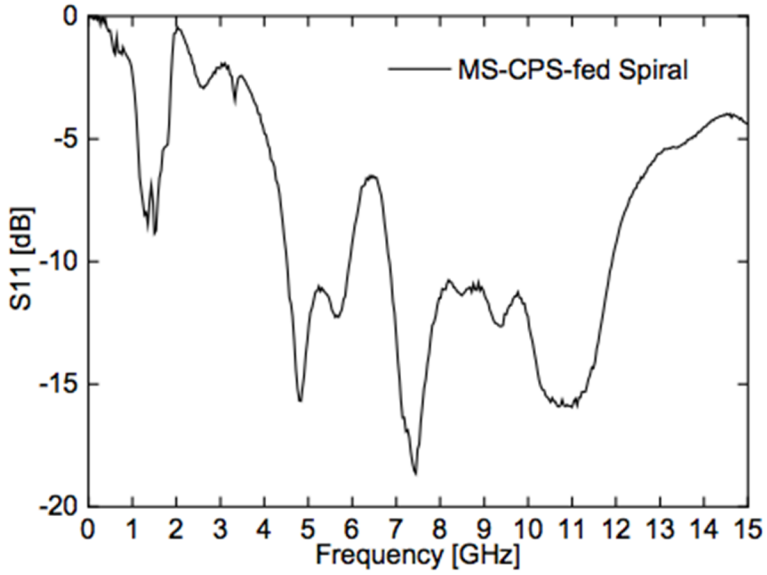

Fig. 61. Negative return loss for Tu's spiral.

Fig. 61 shows the negative return loss for Tu's spiral from 0-15 GHz. His spiral has a 2:1 VSWR impedance bandwidth covering approximately 4.2-6.2 GHz and 6.8-12 GHz. The PPPC-fed spiral has a better impedance match with a 2:1 VSWR

impedance bandwidth covering 2.8-3.3 GHz and 4-14.8 GHz.

Like Dyson's spiral, Tu's spiral also exhibits rotational symmetry, and its radiation pattern has a circularly polarized beam from 7-11.5 GHz. Fig. 62 shows the differences between E_θ and E_ϕ in the $\phi = 0°$ and $\phi = 90°$ planes at 10 GHz. In the $\theta = 0°$ direction, the difference between E_θ and E_ϕ is less than 3 dB.

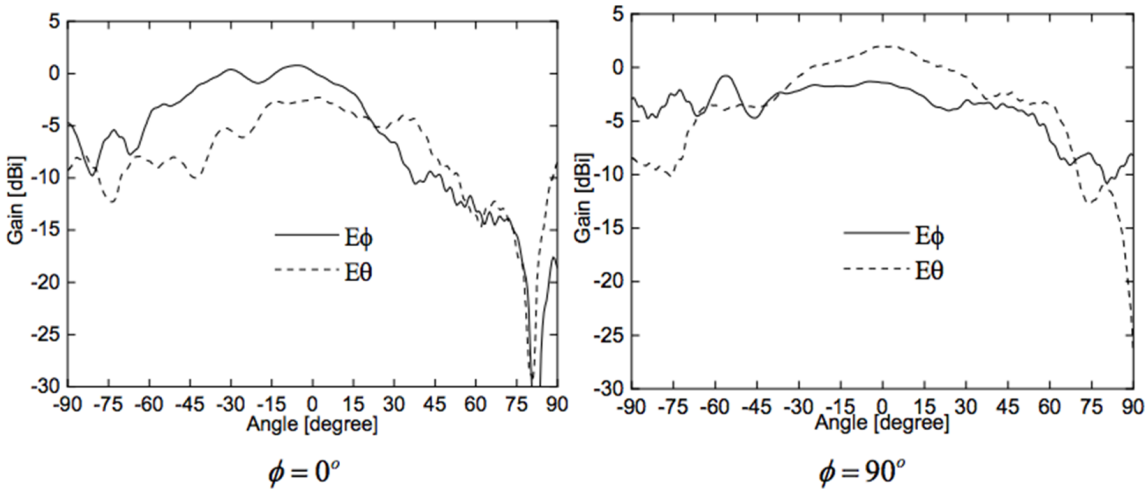

Fig. 62. Radiation patterns in E_θ and E_ϕ for Tu's spiral at $\phi = 0°$ and $\phi = 90°$.

3. Slot Line-fed Archimedean Spiral

Instead of passing a feed line underneath the spiral or choosing to feed it perpendicularly, Wu chose to feed the outer arms of his Archimedean spiral as shown in Fig. 63 by converting a microstrip line into a slot transmission line at the spiral's outer boundaries [4]. By doing so, he avoided interrupting the rotational symmetry

of the spiral to preserve the spiral's circular polarization, but he also narrowed the bandwidth of the radiation pattern by putting a planar reflecting cavity behind the spiral. Since the reflecting cavity works best at a quarter-wavelength spacing away from the spiral antenna, Wu's cavity theoretically narrows the pattern bandwidth with phase subtractions, and in measurement, Wu's spiral showed uni-directional circularly polarized radiation with a 3 dBi gain between 3-5 GHz.

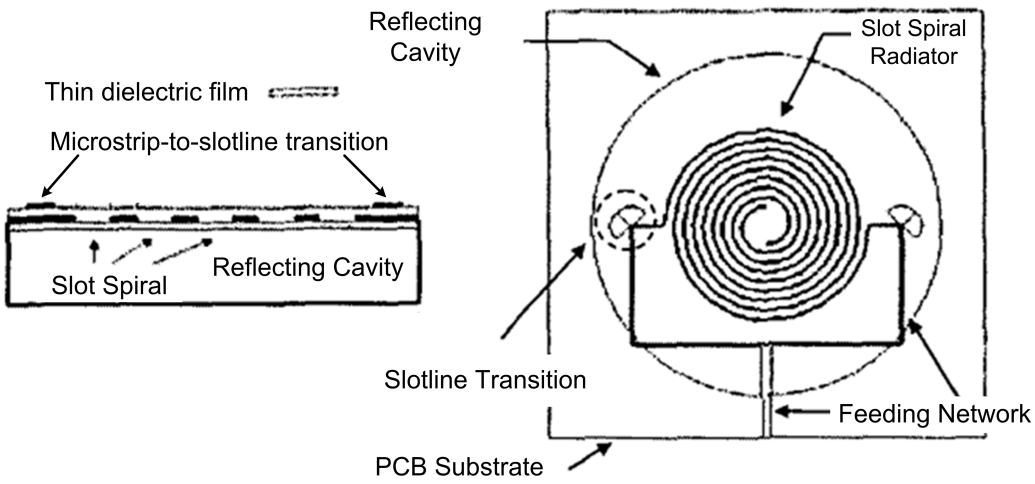

Fig. 63. Wu's cavity backed side-fed spiral antenna.

For the purpose of portable UWB technology, uni-directional radiation is undesirable. Omni-directional radiation in a 2-D plane is preferred in order to cover the horizon where transmitting stations can be reached. Data may be received from multiple directions in a multi-path environment, and signal reconstruction techniques

can be used to recreate the original signal from multiple received signals. Since the PPPC-fed spiral exhibits bi-directional radiation, it may be necessary to use two perpendicular antennas in a portable device to cover the transmitting station horizon if multi-path techniques cannot adequately recreate the intended signal with only one antenna.

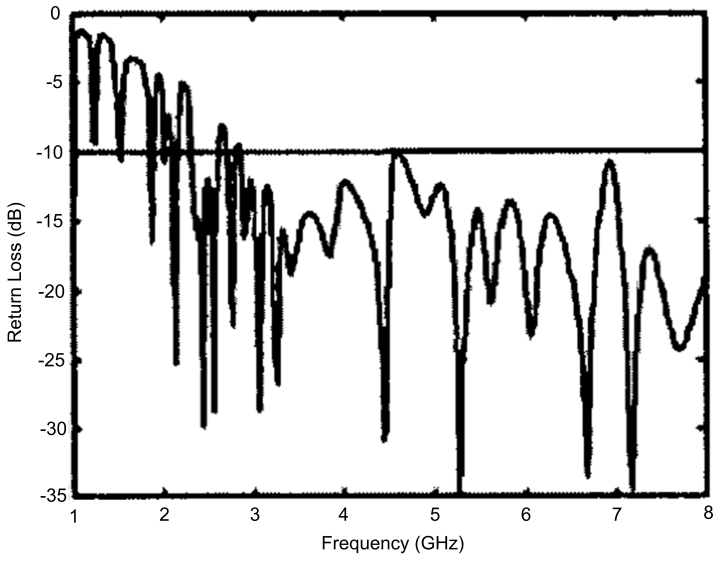

Fig. 64. Negative return loss for Wu's spiral.

If Wu had chosen a conical or parabolic reflector instead of a planar reflector, perhaps his antenna's pattern bandwidth would have been as wide as his 2:1 VSWR impedance bandwidth, which covers 2.8 GHz to at least 8 GHz. The negative return loss for Wu's spiral is shown in Fig. 64.

4. Coaxially-fed Monofilar Archimedean Spiral

Nakano designed a monofilar Archimedean spiral antenna fed perpendicularly by the center probe of a coaxial cable [5]. Like Tu's spiral, Nakano's spiral also requires sufficient cylindrical clearance below the spiral to maintain perpendicularity between the coaxial probe feed and the spiral.

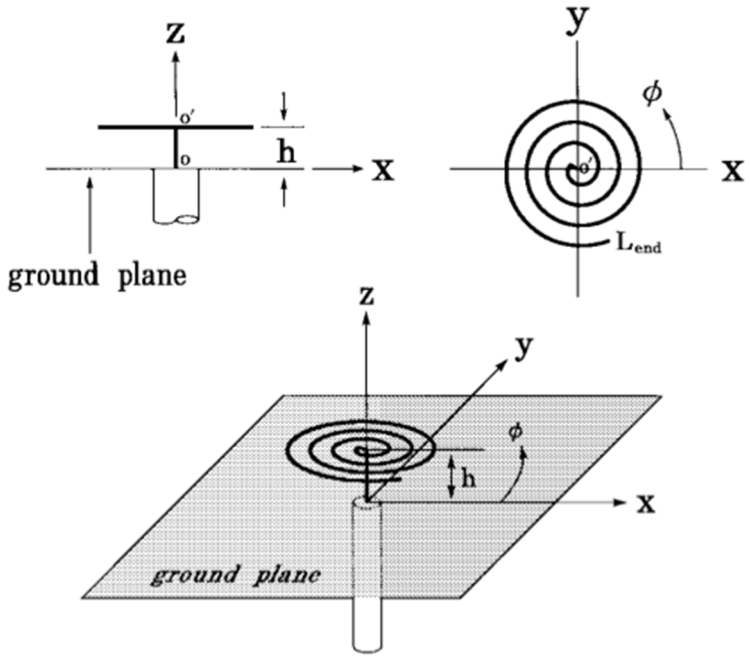

Fig. 65. Nakano's monofilar perpendicularly-fed spiral antenna.

If the coaxial cable comes too close to the spiral at a tilted angle, the spiral's input impedance will undesirably vary. To avoid the tedious positioning of mechanical

stabilizers and to force uni-directional radiation, Nakano placed a ground plane below his monofilar spiral antenna, as shown in Fig. 65.

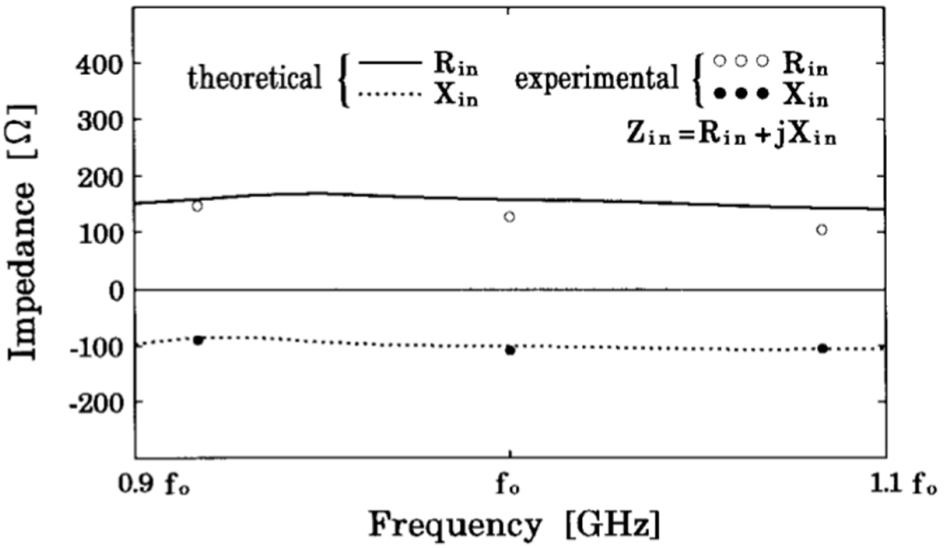

Fig. 66. Real and imaginary impedance for Nakano's spiral near its center frequency.

The input impedance of Nakano's spiral remains relatively constant over a 20% fractional bandwidth, as shown in Fig. 66. Resonance occurs at the frequencies where the imaginary part of the impedance equals zero, so Nakano's spiral antenna does not resonate. The PPPC-fed spiral with holes (including the integrated feed) has an oscillatory input impedance that resonates repeatedly between 3-19 GHz, as shown in Fig. 42. Since a resonant antenna has zero reactive impedance at its resonant frequencies, it does not store wasted energy at those frequencies, allowing it to radiate more efficiently.

The theoretical and experimental right-hand circularly polarized and left-hand circularly polarized radiation patterns for Nakano's spiral are shown in Fig. 67 at the spiral's center frequency. The main beam tilts nearly 30° away from $\theta = 0°$ toward $\phi = 232°$.

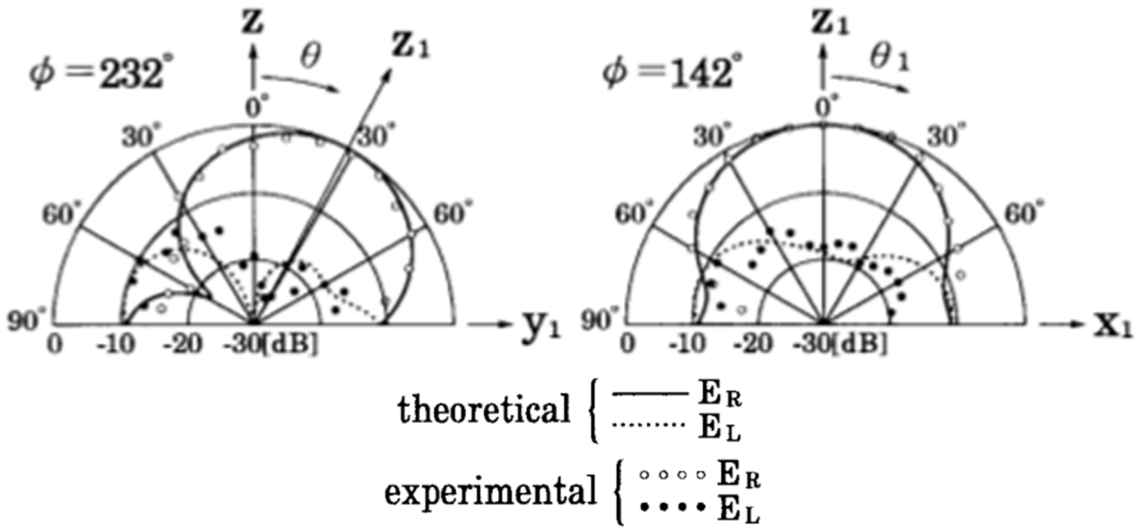

Fig. 67. Right-hand circularly polarized (E_R) and left-hand circularly polarized (E_L) radiation patterns for Nakano's spiral at f_0.

5. Tapered Microstrip Line-fed Archimedean Spiral

Huff designed a planar Archimedean spiral fed by a tapered microstrip line that uses one arm of the spiral as the microstrip ground [3]. Like Dyson's spiral, Huff's feed line follows the spiral's arms to avoid crossing the radiation zone between the arms.

This spiral exhibits a 2:1 VSWR impedance bandwidth from 0.7-1.8 GHz and from 1.9 GHz to at least 3 GHz, and it was designed to operate between 0.7-4.5 GHz, according to Huff's paper [3]. Fig. 68 shows the planar spiral's design and the VSWR associated with it between 0.5-3 GHz.

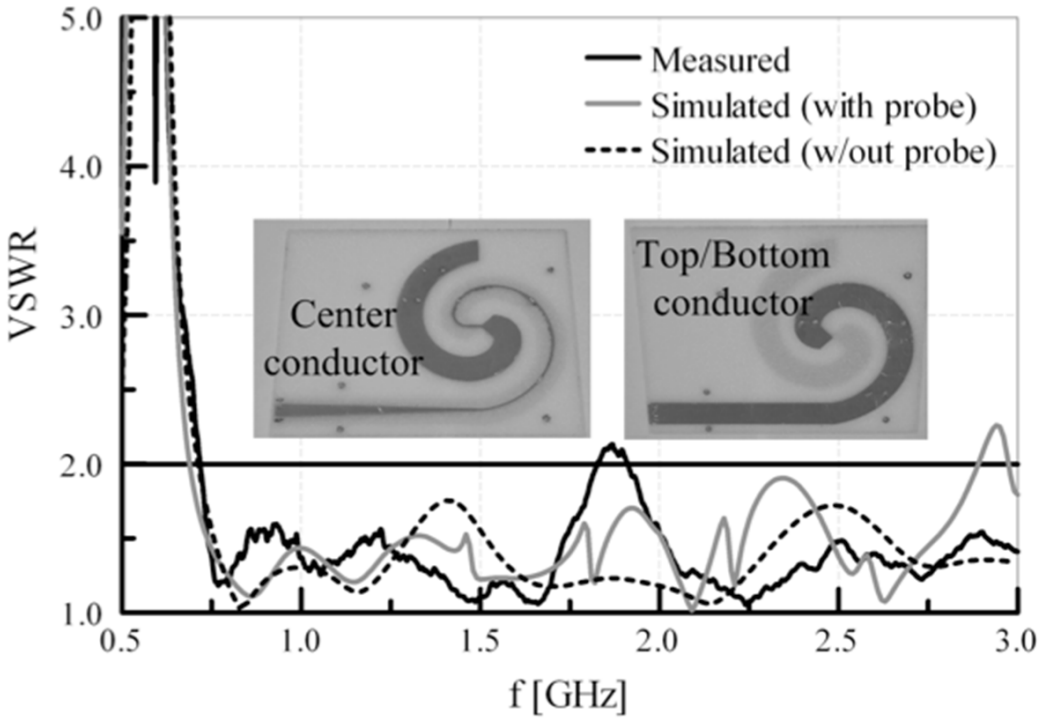

Fig. 68. Top and bottom of Huff's planar spiral antenna and the spiral's VSWR.

Although no radiated fields are presented, Huff states that his spiral has maintained the typical radiation behavior and broadband operation of spiral antennas, according to the early spiral antenna results presented by Dyson [1]. If Huff's spiral

were redesigned to operate from 3.1-10.6 GHz and shown to exhibit the same pattern as Dyson's planar spiral, it would be a good solution to the problem of designing a light-weight, planar spiral for portable UWB applications, like the PPPC-fed spiral.

Huff's spiral only requires one substrate to carry the microstrip line feed and spiral, while the PPPC-fed spiral requires two substrates to carry the DSPSL feed and spiral. For microstrip line networks feeding Archimedean spirals, Huff's single-substrate antenna and feed provide a compact method for powering those antennas. However, Huff's method does not apply for DSPSL-fed antennas because a single substrate does not have enough room for the top and bottom DSPSL conductors as well as a spiral antenna. Therefore a dual substrate integrated feed would need to be used for DSPSL-fed antennas, as shown in the PPPC-fed spiral's design (Figs. 2-4).

Since Huff's feed does not cross the radiation zone of the spiral, his spiral would most likely exhibit circular polarization, while the PPPC-fed spiral exhibits elliptical polarization. Huff's microstrip line is capable of using one spiral antenna arm as a ground plane for signal transmission in order to wrap the feed line directly beneath the spiral, but this same approach cannot be used for DSPSL-fed spirals because the DSPSL has fields circulating above and below the top and bottom conductors. Those fields would be interrupted by the proximity of the spiral on the adjacent substrate. Partially for this reason, and partially to increase the perpendicularity of currents in the spiral and the feed, holes were etched in the PPPC-fed spiral antenna. If the DSPSL feed were wrapped beneath the spiral to prevent crossing the spiral's radiation zone, the losses incurred in the DSPSL feed would be significantly increased due to the circulating field reflections off of the adjacent spiral. To prevent increased return losses, the DSPSL feed in the PPPC-fed spiral takes the shortest path from the coaxial connector to the spiral's center.

B. Coaxial-to-DSPSL Transition Comparisons

This section compares the newly designed coaxial-to-DSPSL transition to two similar transitions to show the physical design differences and the improvements in the new design over the older ones through reduced insertion loss.

1. Microstrip-to-DSPSL Transition

Kim designed a microstrip-to-DSPSL transition in order to measure his DSPSL circuits presented in [8]. Common coaxial-to-microstrip tab connectors can be purchased that aid in making the transition from coaxial line to microstrip line. Therefore, Kim created a microstrip-to-DSPSL transition in order to attach his DSPSL circuits to the existing coaxial-to-microstrip tab connector transition. Kim's transition's design is shown in Fig. 69.

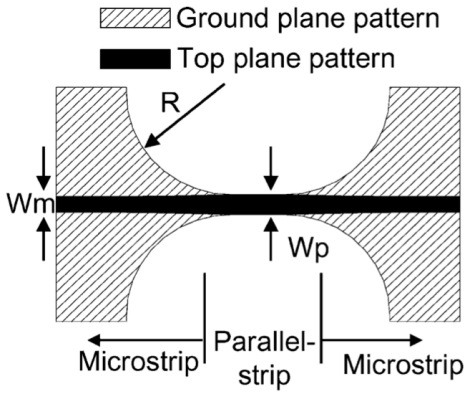

Fig. 69. Kim's back-to-back microstrip-to-DSPSL transition.

By not incorporating the primary coaxial-to-microstrip transition into the design of Kim's microstrip-to-DSPSL transition, he has neglected to consider the losses incurred from his connector type. In fact, these losses can be neglected even in measurement by using a through-reflect-line calibration instead of a short-open-load calibration. This exclusion does not present a problem for circuits that are embedded into microstrip networks, but for antennas that may need to be connected or disconnected for different applications, the coaxial-to-microstrip transition information should be included in the measured data. Kim's transition's network analyzer measurements show the transmitted (S_{21}) and reflected (S_{11}) power levels in Fig. 70.

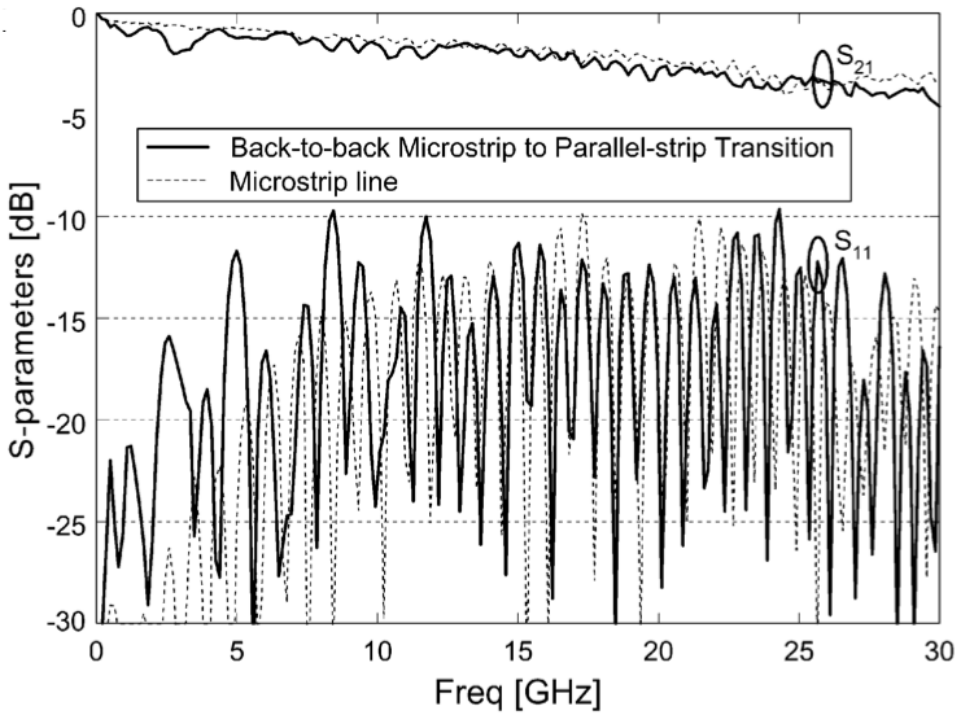

Fig. 70. Transmitted and reflected power levels for Kim's back-to-back microstrip–to-DSPSL transition.

The coaxial transmission line has radially directed electric fields, the microstrip line has primarily vertically directed fields with fringing effects at the microstrip line's edges, and the DSPSL has a combination of vertically directed fields and fringing fields on the top and bottom conductor's edges. In order to create a transition from coaxial-to-DSPSL, the radially directed fields of the coaxial line need to bend to suit the orientations of the microstrip and DSPSL fields. The field-bending phenomenon occurs at the end of the coaxial-to-microstrip connector and between the microstrip and DSPSL. By incorporating both of these field-transition regions into the design of the back-to-back coaxial-to-DSPSL transition shown in Fig. 27, the return loss and the insertion loss in this transition were minimized between 1-11 GHz, which covers the UWB spectrum from 3.1-10.6 GHz.

Kim's back-to-back microstrip-to-DSPSL transition has an insertion loss that varies from 1-2 dB between 3-11 GHz, but the newly designed back-to-back coaxial-to-DSPSL transition has an insertion loss lower than 0.3 dB from 1-11 GHz. The newly designed back-to-back coaxial-to-DSPSL transition includes the losses from the coaxial-to-microstrip transition as well as the microstrip-to-DSPSL transition since they were designed together, and it has lower insertion loss than Kim's microstrip-to-DSPSL transition. In perspective, Kim's transition allows only 63%-79% of the input power to reach the output terminal between 3-11 GHz, but the newly designed transition allows more than 93% of the input power to reach the output terminal between 1-11 GHz.

The return loss in Kim's transition remains better than 9.5 dB from 1-11 GHz, and the return loss in the newly designed transition remains better than 18 dB from 1-11 GHz. Practically, this means that at the input of Kim's transition, less than 11.3% of the input power initially reflects back to the input, whereas at the input of the newly designed transition, less than 1.6% of the input power initially reflects

back to the input between 1-11 GHz.

The SMA PCB mount end-launch jack attachment, the microstrip line taper from the coaxial inner conductor to the 50 Ω line width, and the increased circular taper radius are the major physical differences between Kim's transition and the newly designed transition.

The end-launch jack attachment to the transition gives the coaxial-to-microstrip transition approximately 5 mm of extended quasi-co-planar waveguide, allowing the fields to appropriately bend to suit the microstrip line instead of reflecting back to the input. As shown in Fig. 25, the grounding prongs that extend from the end-launch jack allow the ground to more gradually recede from the center conductor instead of abruptly terminating the coaxial line with a tabbed SMA-to-microstrip connector.

The 0.83 mm tapered microstrip line, shown in Fig. 27 just to the right of Section A, reduces the return loss of the newly designed back-to-back transition by more gradually transitioning the center conductor of the coaxial line from 1.23 mm to the 2.15 mm 50 Ω microstrip line width.

By increasing the circular taper radius and thereby extending the length of Kim's transition from 6 mm to 40 mm, the return and insertion losses were further reduced. This length extension provided a greater space through which the microstrip field lines could be bent into the DSPSL field line positions.

2. Microstrip-to-co-planar Strip Line Transition

Although Tu's transition has a different form, it serves the same purpose as the newly designed coaxial-to-DSPSL transition. Tu's microstrip to co-planar strip line transition converts a microstrip line into a spiral antenna feed [7]. Like Kim's transition, Tu's transition ignores the coaxial-to-microstrip transition that is required for measurement purposes and also for antenna connections and disconnections. Fig. 71

shows this transition's design parameters.

This transition utilizes a stepped impedance transformer adjacent to a coupling balun in order to convert the microstrip line into a co-planar strip line so that it can perpendicularly feed a spiral antenna. The gray portions of Fig. 71 illustrate the microstrip ground plane, and the black portions of this figure illustrate the microstrip line and the co-planar strip line. The length of Tu's transition extends 27 mm, making it nearly 3/4 the length of the newly designed transition.

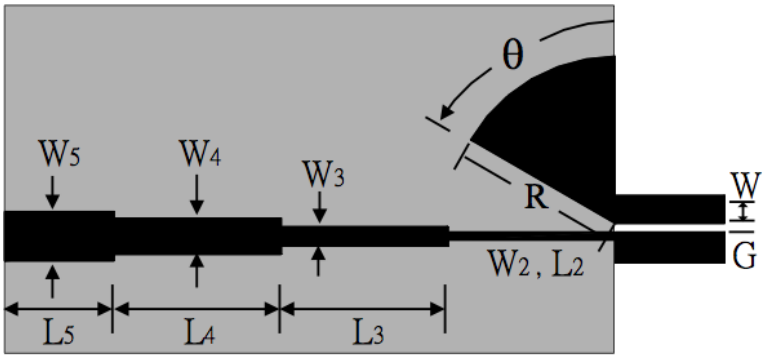

Fig. 71. Tu's microstrip-to-co-planar strip line transition.

Tu's microstrip to co-planar strip line transition exhibits a return loss better than 10 dB from 4-13 GHz, and it has an insertion loss that varies from 0.5 dB to 3 dB from 3-12 GHz. While the low return loss allows more than 90% of the input power to enter the transition instead of reflecting back to the input, the insertion loss forces between 11-50% of the power entering the transition to either remain trapped in the transition or to radiate away from it. The return and insertion losses of Tu's

transition are shown together in Fig. 72.

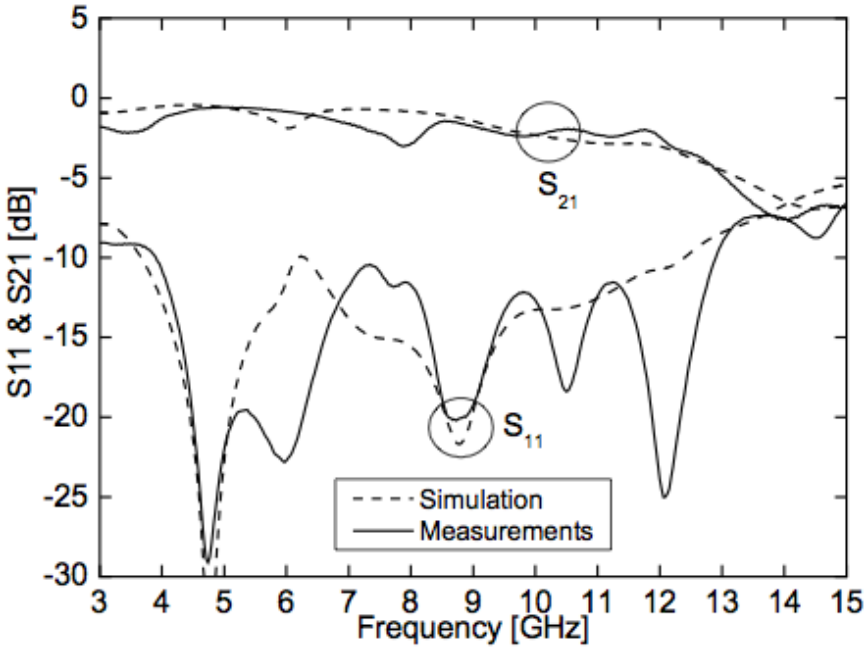

Fig. 72. Transmitted and reflected power levels for Tu's back-to-back microstrip-to–co-planar strip line transition.

C. UWB DSPSL Power Divider Comparisons

This section compares the newly designed UWB DSPSL equal and unequal power dividers with Wilkinson microstrip equal and unequal power dividers. The DSPSL and microstrip equal dividers both exhibit low insertion loss and an UWB 2:1 VSWR bandwidth, but the unequal microstrip divider exhibits a much lower impedance

bandwidth than the unequal DSPSL divider.

1. UWB Microstrip Line Equal Power Wilkinson Divider

Wong created a Wilkinson microstrip equal power divider with an UWB 2:1 VSWR impedance bandwidth spanning from approximately 3.3-10.8 GHz that also has low insertion loss across this frequency range [35]. The newly designed DSPSL equal power divider exhibits a larger 2:1 VSWR impedance bandwidth spanning from 1-10.7 GHz, and it does not require the four quarter-wavelength short-circuit tuning stubs shown in Fig. 73, whose lengths are defined for the Wilkinson's center frequency of 6.85 GHz. The measured and simulated S-parameters for Wong's UWB Wilkinson divider are shown in Fig. 74.

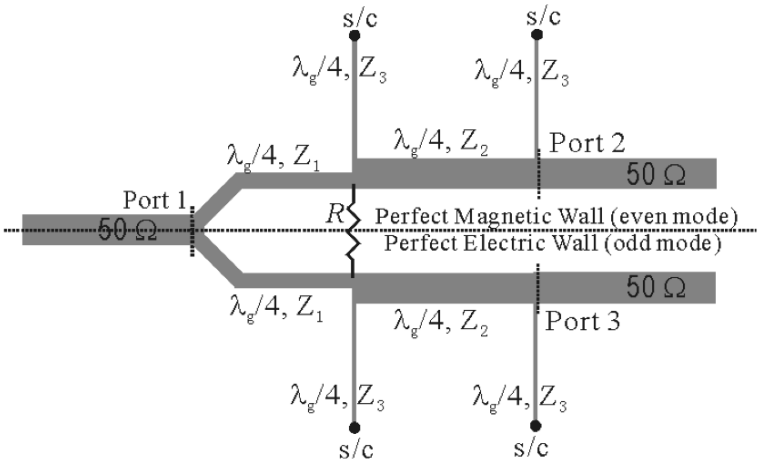

Fig. 73. Wong's microstrip line-fed UWB equal power Wilkinson divider.

The UWB Wilkinson divider exhibits an isolation between Port 2 and Port 3 better than 10 dB over the 2:1 VSWR impedance bandwidth, but this parameter does not apply to the array of linearly combined antennas for which the equal and unequal UWB DSPSL dividers were created. Since the transmitted and received signals in the DSPSL array in Fig. 40 are all in-phase and equivalent at the DSPSL dividers' conjoining junctions, output port isolation is meaningless for that array.

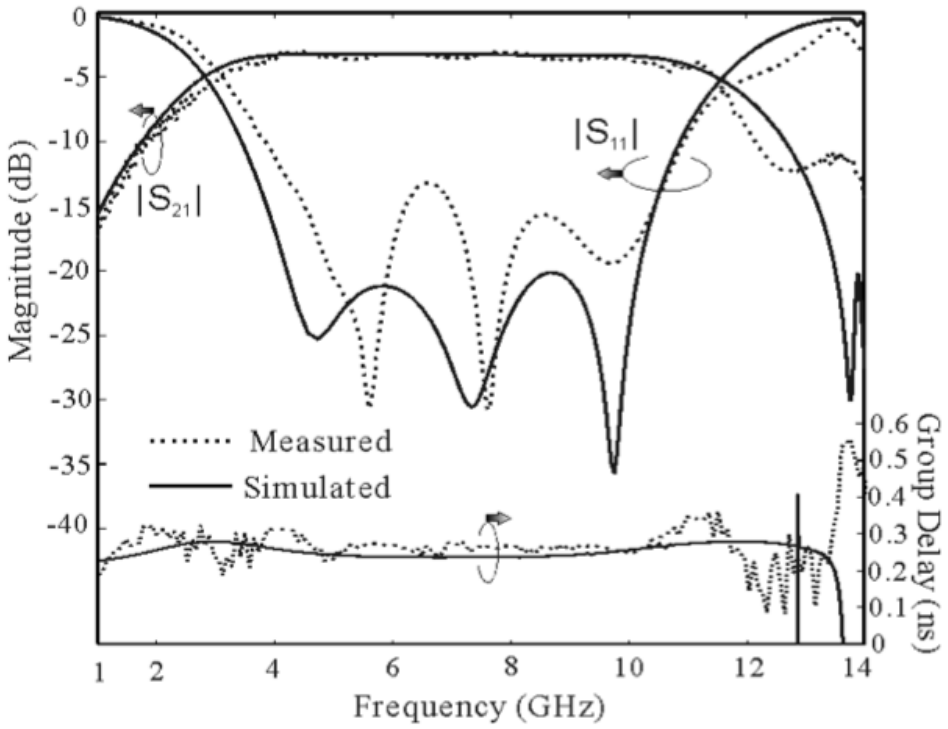

Fig. 74. Transmitted and reflected power levels for Wong's Wilkinson divider.

2. Microstrip Line Unequal Power Wilkinson Divider

The Wilkinson microstrip unequal power divider shown in Fig. 75 has 4:1 ratio power splitting between port 2 and port 3, with port 2 receiving the higher power level [36].

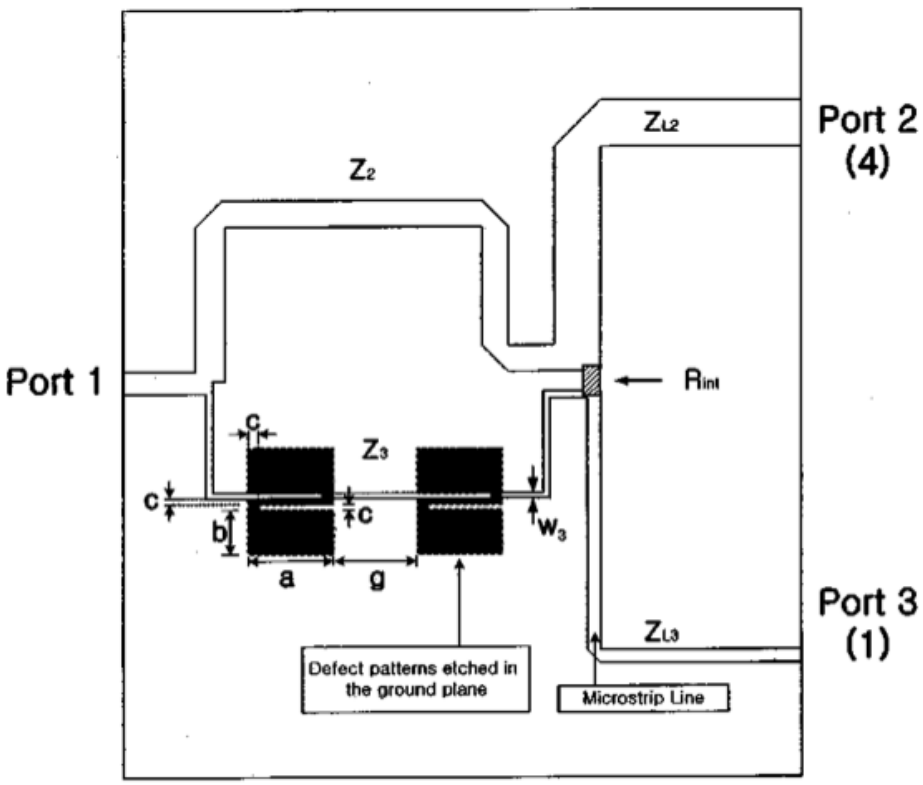

Fig. 75. Lim's microstrip line-fed unequal power Wilkinson divider.

The output power levels received at each port remain constant over the divider's 1.4:1 VSWR impedance bandwidth that covers 1.2-1.8 GHz, as shown in Fig. 76.

The operational bandwidth of the newly designed DSPSL unequal divider surpasses the operational bandwidth of the Wilkinson microstrip unequal divider because it maintains a 2:1 VSWR bandwidth and stable output power ratio from 3-13 GHz for its 2:1 and 3:1 power ratio configurations, as shown in Fig. 32.

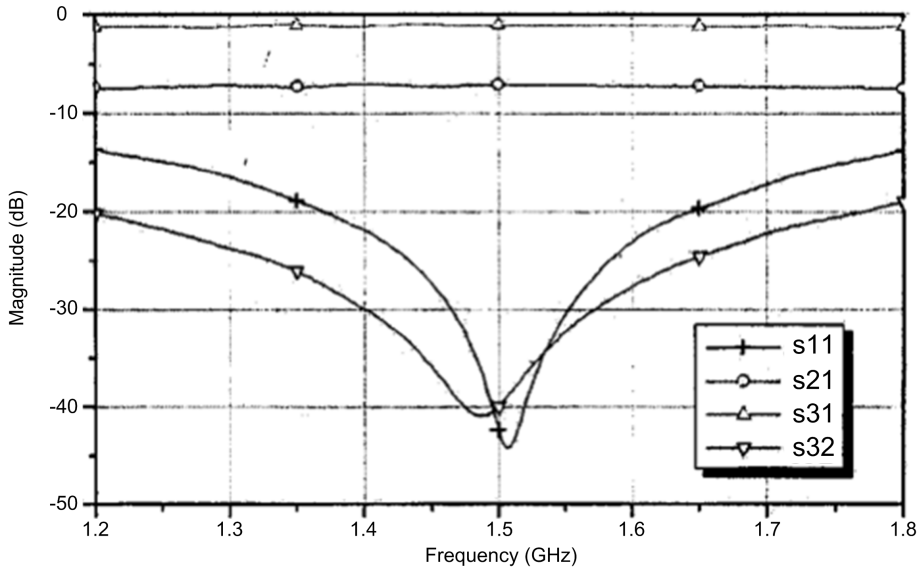

Fig. 76. Transmitted and reflected power levels for Lim's Wilkinson divider.

D. Radial Dipole Antenna Comparisons

This section shows two examples of microstrip-to-co-planar strip line-fed dipole antennas and compares their performances to the performance of the DSPSL-fed radial

dipole antenna presented in this dissertation.

1. Microstrip-to-co-planar Strip Line-fed Circular Dipole

The antenna shown in Fig. 77 consists of two circular antenna components fed by a microstrip-to-co-planar strip line transition [37]. Like DSPSL, co-planar strip line carries two lines that are 180° out of phase. Unlike DSPSL, these two lines are both located on the same side of one substrate.

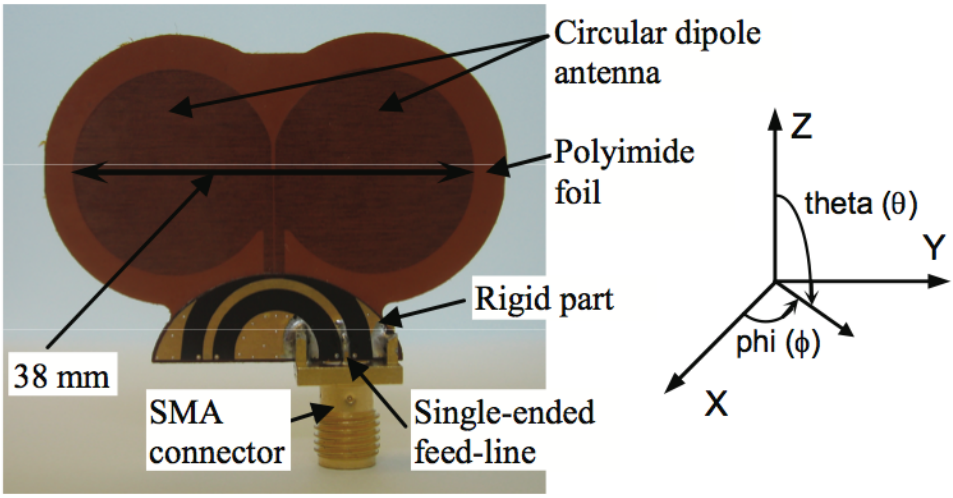

Fig. 77. Karlsson's microstrip-to-strip line-fed circular dipole.

While the DSPSL-fed radial dipole antenna shown in Fig. 33 has a 33% fractional 2:1 VSWR impedance bandwidth and a similar geometry to the co-planar strip line-fed radial dipole shown in Fig. 77, the co-planar strip line-fed radial dipole has a 60%

fractional 2:1 VSWR impedance bandwidth, as shown in Fig. 78.

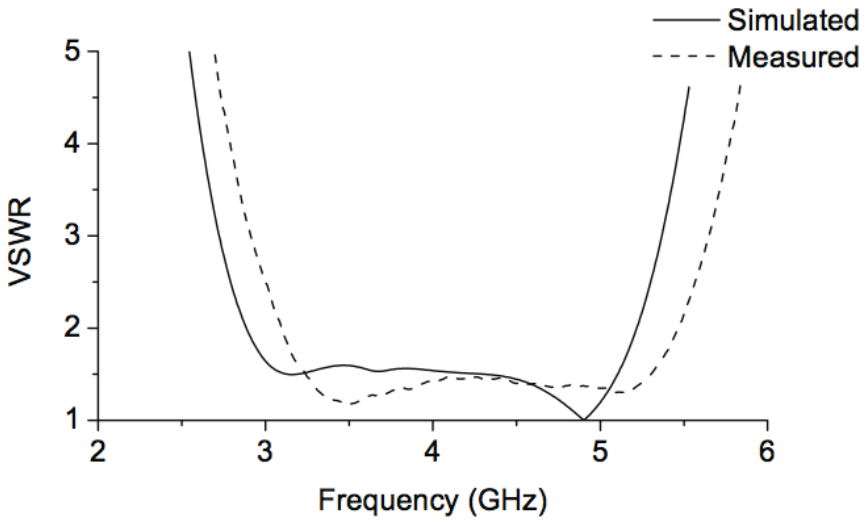

Fig. 78. Measured and simulated VSWR of Karlsson's circular dipole.

The disparity between the bandwidth of the newly designed radial dipole and the co-planar strip line-fed dipole may arise from the fact that the transmission line spacing in the 4x4 DSPSL-fed array limits size of the newly designed radial dipole to fit inside of a 50 mm square while maintaining a center frequency at 3 GHz. The newly designed dipole spans 38 mm across its largest dimensions while the co-planar strip line-fed dipole also spans 38 mm across its largest dimensions. If the co-planar strip-line antenna were scaled for a center frequency of 3 GHz, its largest dimensions would require 50.7 mm of clearance, which would not fit inside the allotted space in the DSPSL 4x4 array. The co-planar strip line-fed radial dipole exhibits the typical

radiation pattern of a dipole antenna across its 2:1 VSWR impedance bandwidth.

2. UWB Microstrip-to-co-planar Strip Line-fed Dipole

Another variation on the co-planar strip line-fed dipole, shown in Fig. 79, exhibits a 2:1 VSWR impedance bandwidth covering the entire FCC allotted UWB frequency range while maintaining a radiation pattern similar to the typical dipole across this entire range [38].

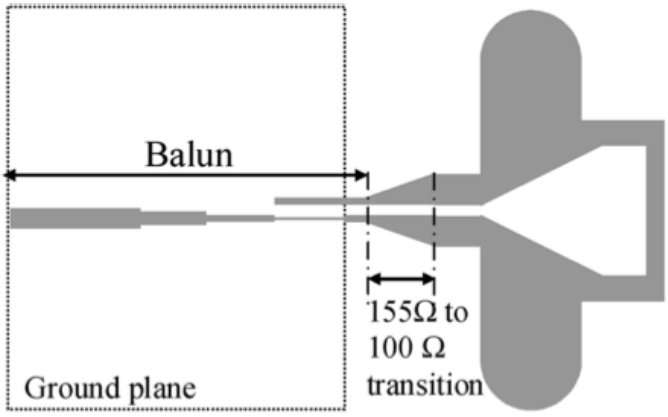

Fig. 79. Low's microstrip-to-strip line-fed dipole.

This antenna's bandwidth far exceeds the bandwidth of the newly designed DSPSL-fed radial dipole. The measured and simulated reflection coefficient for this antenna are shown in Fig. 80. This co-planar strip line-fed dipole uses a shorting bridge between the two dipole arms to increase the antenna's bandwidth, but even without the shorting bridge, the antenna exhibits a 2:1 VSWR impedance bandwidth

covering the range 4.5-12 GHz. Perhaps the tapered impedance matching section between the antenna and the feed line help to give this dipole such a large impedance bandwidth.

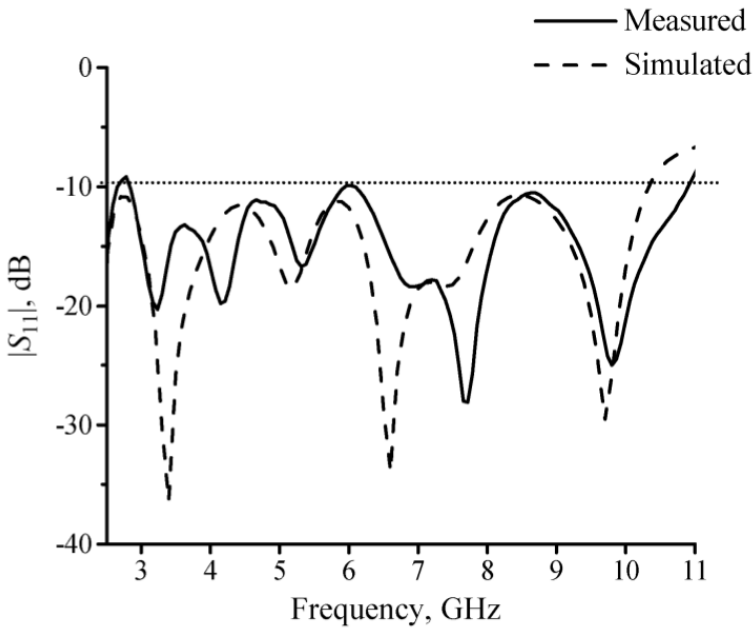

Fig. 80. Measured and simulated S_{11} of Low's dipole.

E. Radial Dipole Antenna Array Comparisons

This section compares three different dipole arrays to the DSPSL-fed 4x4 radial dipole array in order to show how the newly designed array relates to previously designed arrays with respect to operational bandwidth, radiation pattern, and side-lobe level.

1. Linear Four-element Microstrip-to-DSPSL Dipole Array

A four-element DSPSL-fed rectangular dipole array was designed by Evtioushkine in [39]. Although he did not use DSPSL as a transmission line in his array, he created a tapered microstrip-to-DSPSL transition to convert his microstrip line feed network into DSPSL at the input of his antennas, as shown in Fig. 81.

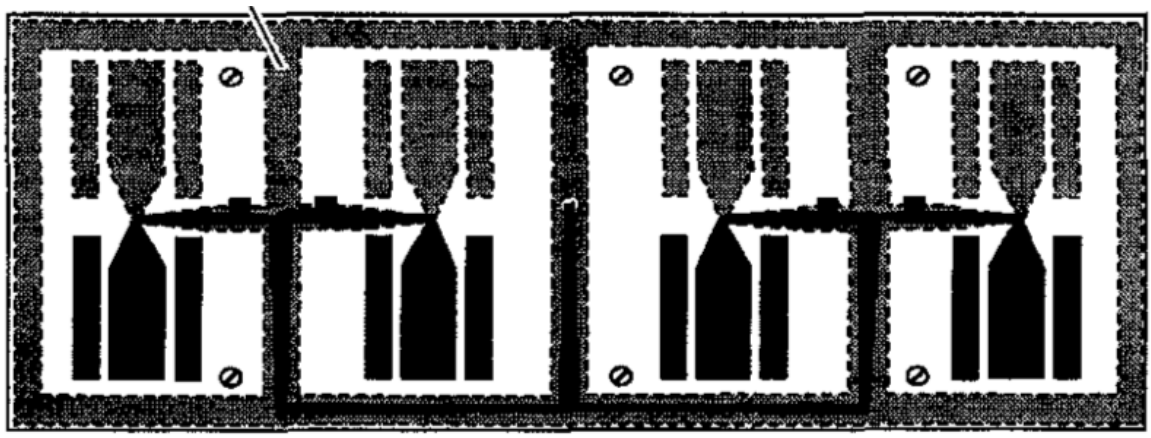

Fig. 81. Evtioushkine's linear four-element microstrip-to-DSPSL dipole array.

The linear four-element dipole array of Fig. 81 has a larger fractional bandwidth than the newly designed 4x4 array, but the newly designed 4x4 dipole array has a lower SLL. The 66% fractional 2:1 VSWR bandwidth of Evtioushkine's array is twice as wide as the 2:1 VSWR bandwidth of the newly designed DSPSL-fed 4x4 radial dipole array. Evtioushkine's array has a SLL of -16 dB along the array's axis, while the newly designed DSPSL array has a -20.6 dB SLL in one axis of the array and a

-23.4 dB SLL in the perpendicular direction.

2. DSPSL-fed Planar Yagi-Uda Array

A different type of DSPSL-fed dipole array is shown in Fig. 82, which uses dipoles of different lengths to create a planar Yagi-Uda style antenna [40]. This array exhibits a 2:1 VSWR bandwidth nearly covering the whole UWB range (3.1-10.6 GHz), and it also radiates uni-directionally with a -18 dB SLL.

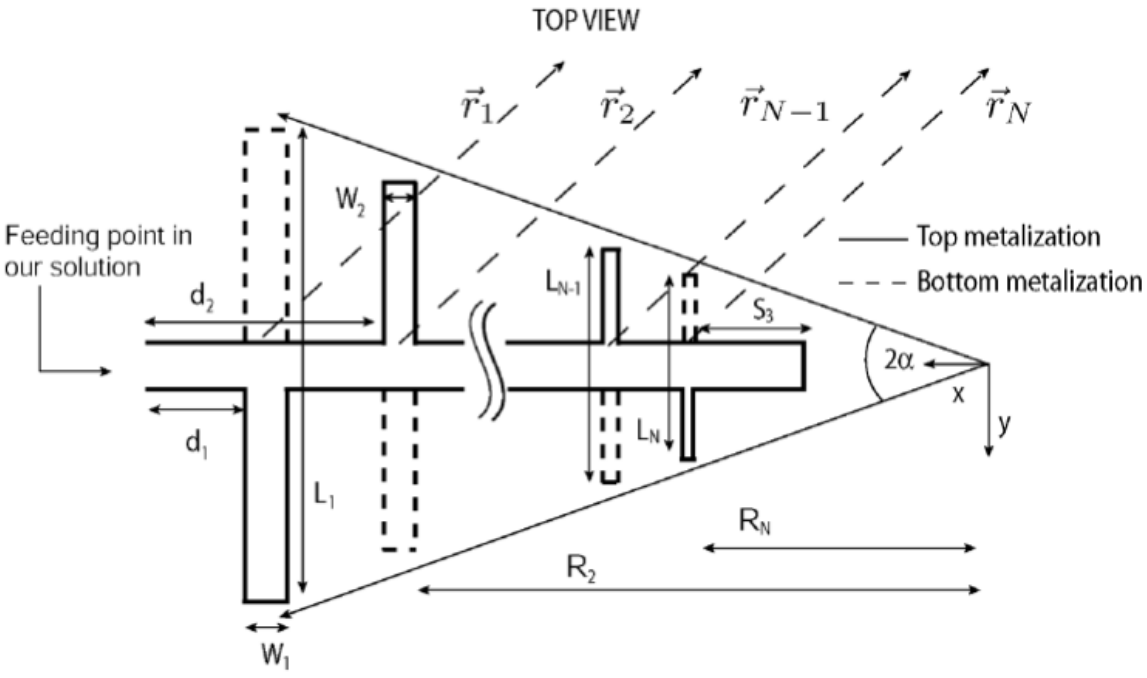

Fig. 82. Merli's DSPSL-fed planar Yagi-Uda array.

The reflected power level versus frequency of this array is shown in Fig. 83. The measured 2:1 VSWR bandwidth extends from approximately 4.2-10.7 GHz. This array is capable of operating at most frequencies in the UWB band, but the fidelity factor comparisons given in [40] suggest that the planar Yagi-Uda array loses approximately 16% of the information that it transmits, which is about twice as high as the amount of information lost by a planar monopole antenna.

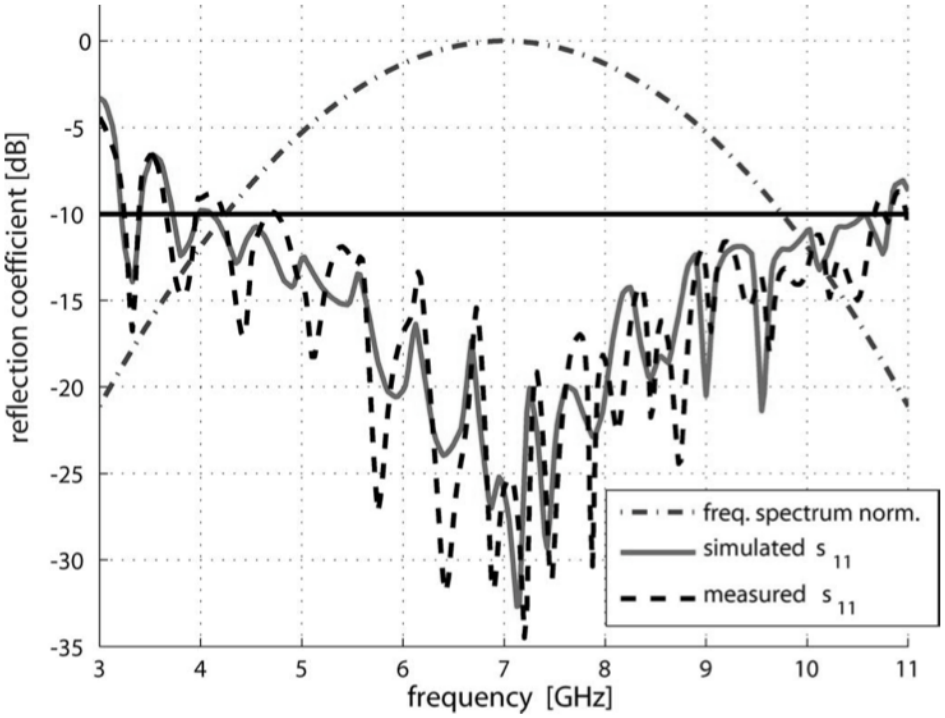

Fig. 83. Measured and simulated reflected power levels for Merli's Yagi-Uda array.

The radiation pattern of this array at 10.3 GHz is shown in Fig. 84. This figure

shows that the array radiates with linear polarization, as is expected from a dipole radiator. It also shows that the side-lobes of the array occur on the back side of the array. These back lobes essentially waste radiated energy from the array since the array radiates uni-direcitonally, and they do not interfere with the main beam's radiation.

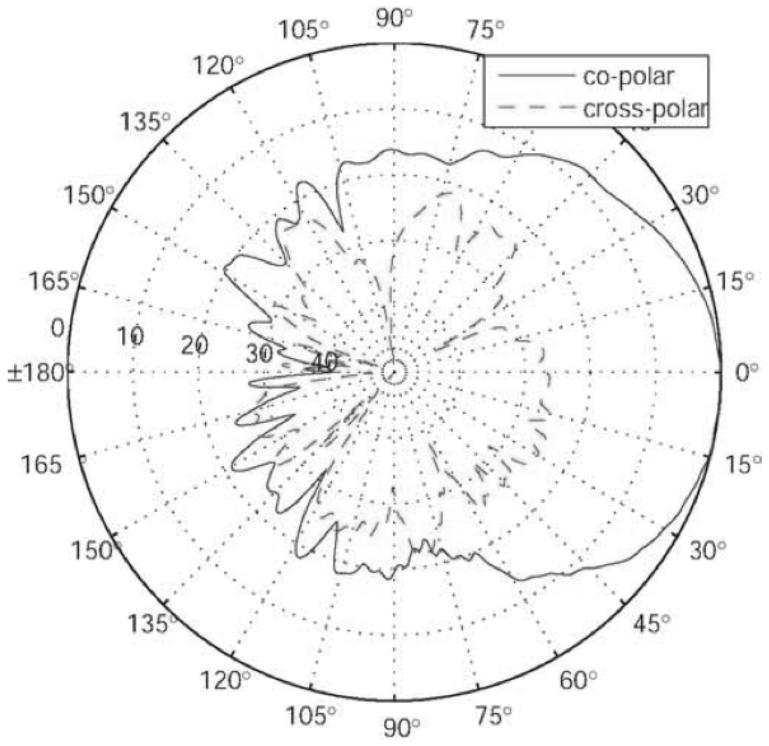

Fig. 84. Co- and cross-polarization radiation measurements for Merli's Yagi-Uda array at 10.3 GHz.

Since the DSPSL-fed 4x4 dipole array radiates bi-directionally, minimal side lobe

levels in both directions are desired to prevent data miscommunications. The minimal SLL of the bi-directional DSPSL-fed 4x4 dipole array occurs only at 3.05 GHz, whereas the uni-directional planar Yagi-Uda array has a minimal SLL throughout its impedance bandwidth.

3. Dual-polarized Dipole Array

A switchable linearly polarized dipole array was designed in [41] that allows the user to choose the direction of the array's polarization based on which dipole antennas receive power. Fig. 85 illustrates this array. Like the newly designed DSPSL-fed array, this array uses an equal distance spacing between several dipole antennas. Unlike the newly designed DSPSL-fed array, this array places the dipole antennas on a triangular grid with a three-dimensional feed network.

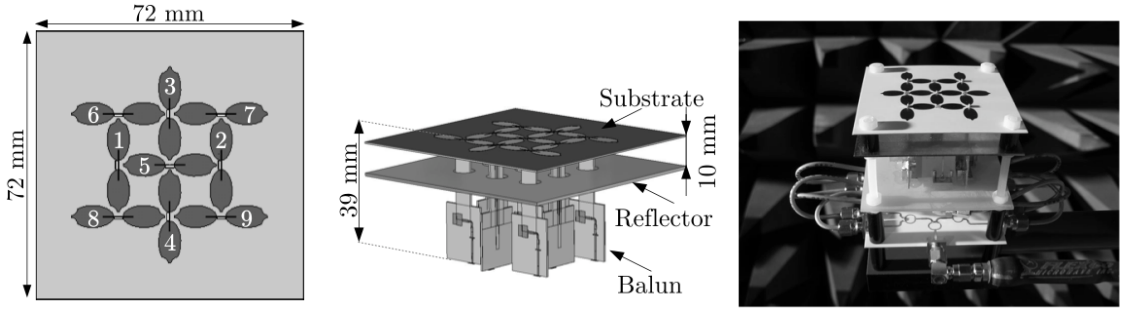

Fig. 85. Hees' dual-polarized dipole array in (a) CST Microwave Studio and (b) realization.

As shown in Fig. 86, this array has a relatively high return loss from 2-9 GHz with frequency intervals of low return loss throughout that range. The reflector shown in Fig. 85(a) is spaced only 10 mm from the antenna array, which is a quarter-wavelength spacing ideal for re-directing backwards traveling radiation at 7.5 GHz. Perhaps this reflector contributes to the high return loss of the antenna between 3-9 GHz by pushing radiated energy back into the antenna elements.

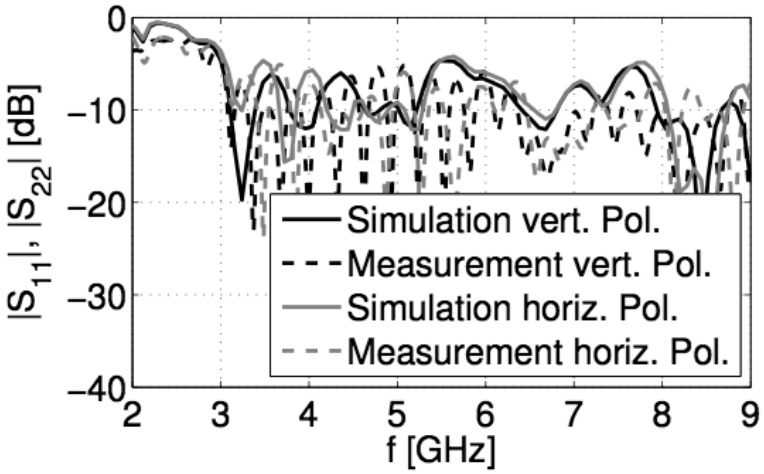

Fig. 86. Measured and simulated reflected power levels for Hees' array in the vertical and horizontal polarization orientations.

Since the SLL of a two-dimensional array varies with its frequency of operation as demonstrated in Figs. 49-50, it may be difficult to maintain a low SLL over the entire UWB range for two-dimensional UWB antenna arrays. While these arrays would provide increased gain, multiple reflections from larger SLLs negatively affect

UWB operation. The gain of the switchable polarization array is shown in Fig. 87 from 2-9 GHz, and the SLL varies from -7 dB to -17 dB over this range.

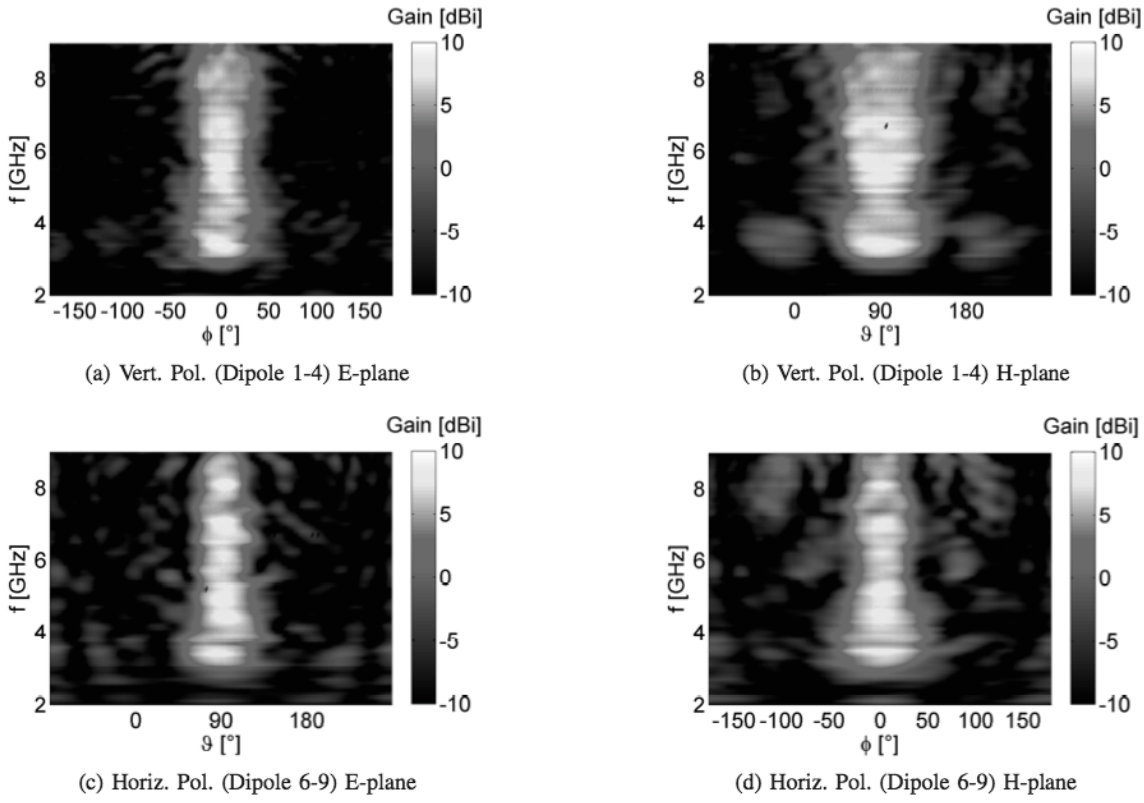

Fig. 87. Measured gain of Hees' dual-polarized dipole array.

F. Circular Monopole Antenna Comparisons

This section compares the newly designed DSPSL-fed circular monopole antenna to two other types of previously designed circular monopole antennas. In addition,

this section also describes an array of circular monopole antennas to predict the characteristics of a hypothetical circular monopole antenna array based on the newly designed antenna and to show that it is possible to array circular monopoles together to create an UWB array.

1. Co-planar Waveguide-fed Circular Monopole

Similar to the newly designed circular monopole antenna, the antenna shown in Fig. 88 feeds a circular metal patch with its high feed line and radiates between that patch and the nearby ground [42]. Unlike the newly designed circular monopole, the co-planar waveguide feed of the antenna shown in Fig. 88 terminates the ground near the circular patch instead of surrounding the patch.

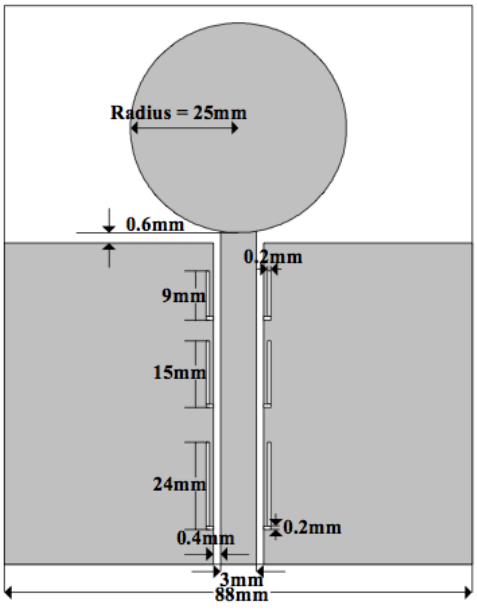

Fig. 88. Yu's co-planar waveguide-fed circular monopole antenna.

Like the newly designed circular monopole, this circular monopole also exhibits an intermittent 2:1 VSWR bandwidth, as displayed in Fig. 89. Between 1-2 GHz, the antenna radiates bi-directionally, but as the frequency increases past 3 GHz, beam squinting occurs in the direction facing away from the co-planar waveguide ground. This phenomenon also occurs for the newly designed circular monopole.

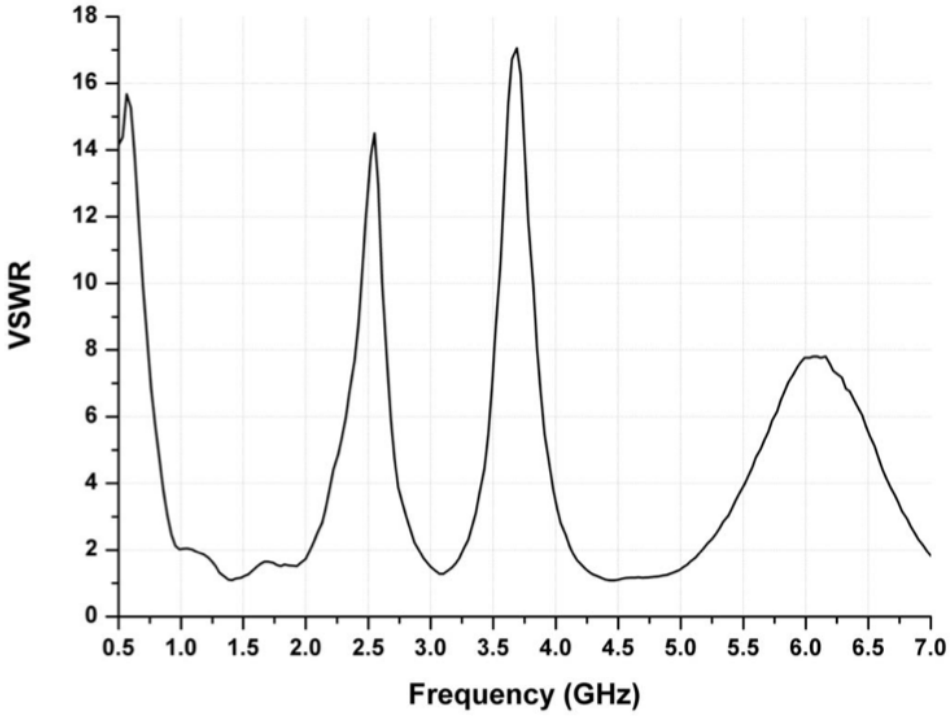

Fig. 89. VSWR of Yu's co-planar waveguide-fed circular monopole antenna.

2. Coaxial Line-fed Circular Monopole Disk

The circular monopole antenna shown in Fig. 90 was fed directly by a coaxial transmission line with a ring attached to the outer shielding of this line [43]. Like the newly designed circular monopole, the ground of this antenna surrounds the center conductor with a radius nearly double that of the circular center conductor.

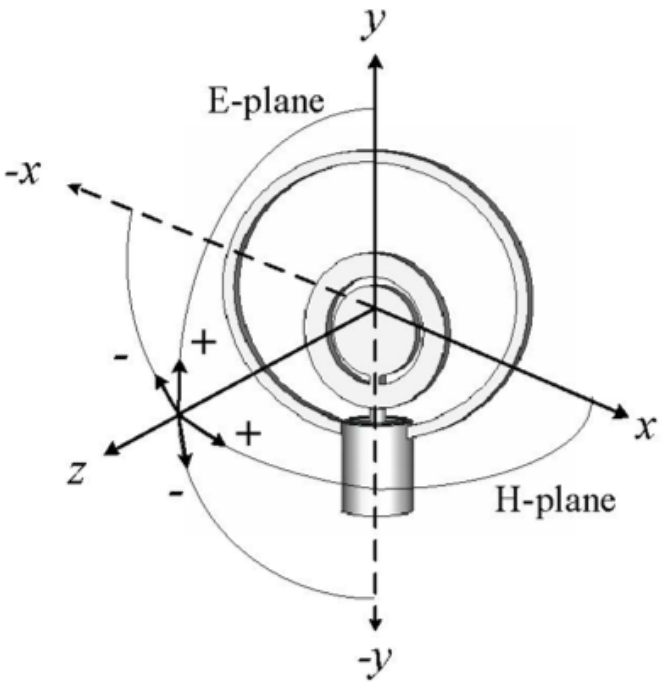

Fig. 90. Chaw's coaxial line-fed circular monopole disk.

A slot was cut into the circular disk in the center of the antenna to suppress WLAN interference at 5.8 GHz, as shown in Fig. 91. Unlike the newly designed

DSPSL-fed circular monopole, this antenna exhibits a lower return loss throughout the UWB range. Similar to the newly designed circular monopole, this antenna also exhibits beam squinting away from the feed direction near 10 GHz and bi-directional radiation below that frequency.

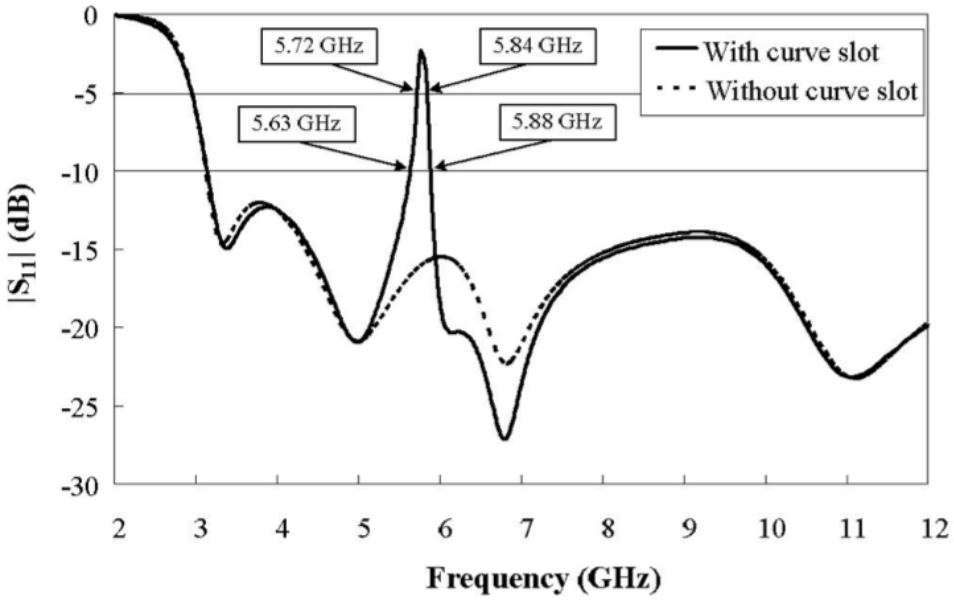

Fig. 91. Reflected power levels for Chaw's circular monopole with and without the curved slot.

3. Microstrip Line-fed Circular Monopole Array

To show that it is possible to array circular monopole antennas together to create an UWB array and to predict the performance of an array of the newly designed circular

monopole antenna, the array created by Ihsan shown in Fig. 92 has been included in this discussion [44]. Ihsan's array exhibits an UWB 2:1 VSWR impedance bandwidth that covers the entire UWB range.

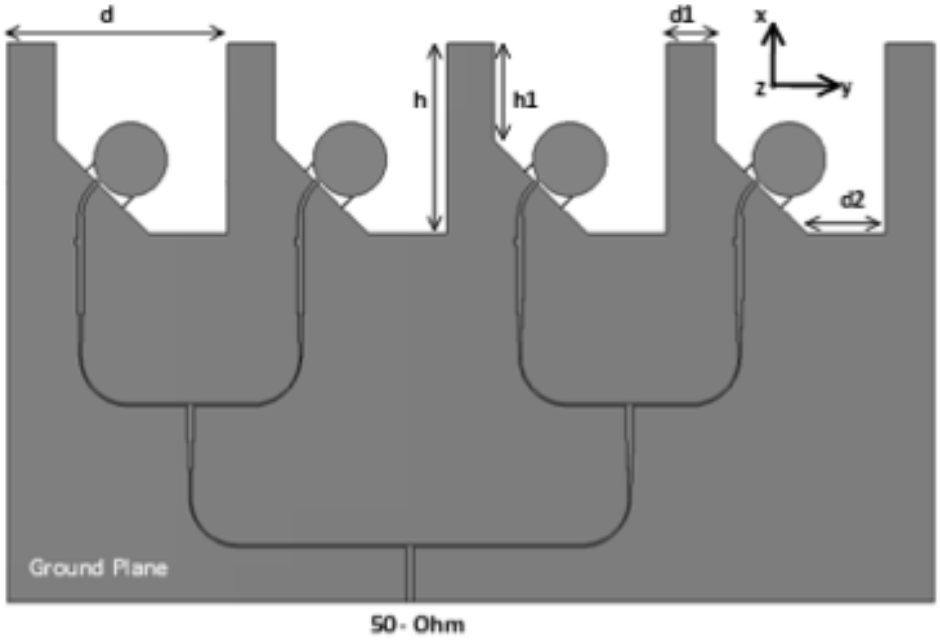

Fig. 92. Ihsan's microstrip line-fed circular monopole array.

This array linearly combines four circular monopole antennas to produce an increased gain usable over the entire UWB band. Instead of shying away from the beam squinting that occurs at higher frequencies, Ihsan purposefully tilted his antennas so that the beam squinting at higher frequencies would occur in the direction of the main beam's radiation. Fig. 93 shows the effect of the beam squinting on the gain of the

array. In this figure, the main beam gain increases and the SLL also increases with frequency due to the predicted beam squinting with increased frequency of operation.

If a phased, steerable array of such antennas could be created that has high gain and low side-lobes at a low frequency and minimal gain with high side-lobes at a high frequency, then the antenna would be suitable for radar target tracking. By finding the target's position at low frequencies with the main beam and switching to the higher frequency monopulse beam to verify the target's position, radar could actively track a target.

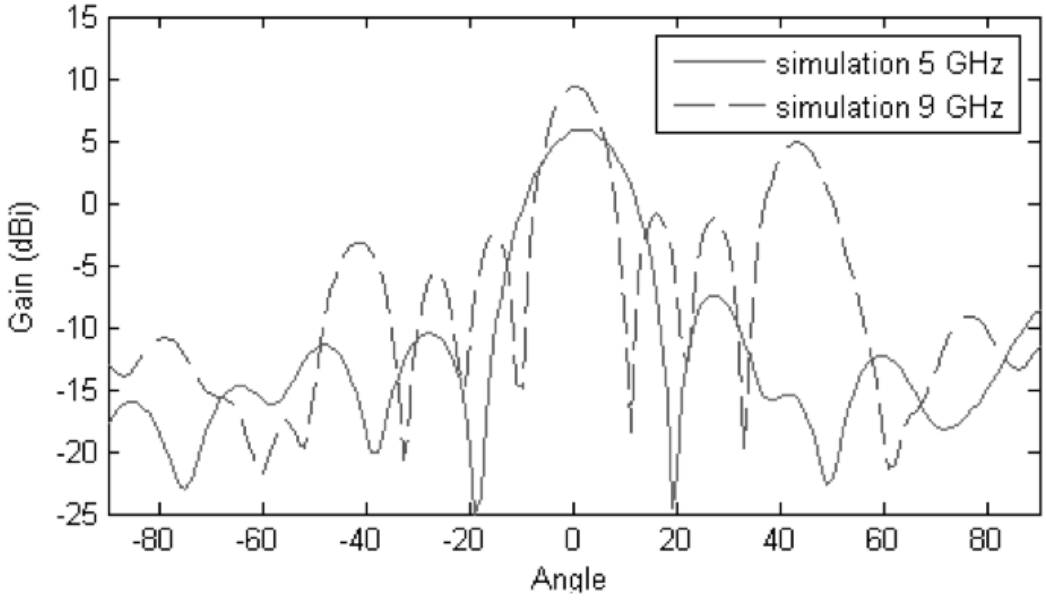

Fig. 93. Simulated gain versus angle ϕ for Ihsan's array at 5 and 9 GHz.

CHAPTER V

SUMMARY AND CONCLUSIONS

This chapter summarizes the novelty of the research presented in this dissertation and its usefulness to other researchers.

A. Summary

The work in this dissertation originated with the design of the PPPC-fed spiral antenna and extended into DSPSLs and other antennas that could be fed by DSPSL. The major concepts that were introduced include the creation of a compact, planar spiral antenna that could be integrated into portable commercial UWB technology, a new design for a low-loss UWB coaxial-to-DSPSL transition, an equal and unequal UWB DSPSL power divider, a DSPSL-fed radial dipole antenna, a two-dimensional array of DSPSL-fed radial dipole antennas that utilize the new DSPSL transition and power dividers, and a DSPSL-fed circular monopole antenna.

B. Conclusions

The parallel-plane perpendicular-current feed for a modified equiangular spiral antenna retains the ultra-wideband impedance and radiation characteristics of the equiangular spiral while minimizing the volume consumed. This minimal volume allows upcoming UWB technology to utilize the PPPC-fed spiral for long or short range communications in remote devices. The novelty of the PPPC feed lies mainly in this answer to the question, "How can an equiangular spiral antenna be fed from the side with a parallel-strip line in order to save space in future portable UWB technology?" Multiple answers to that question do exist [3], and the exploration of those concepts

may reveal important stepping stones for technological advances in the future for UWB technology, even including the application of perpendicular-current feeds to other existing systems.

Since there are no commercially available coaxial-to-DSPSL connectors, it has been necessary for designers to create their own transitions to suit their needs. By designing a low-loss transition from coaxial-to-DSPSL that operates over the entire UWB frequency range, this dissertation prevents designers from having to start from scratch every time they need to feed a DSPSL with a coaxial line. Any time that DSPSL-fed circuits are used, connections to coaxial lines must also be made in order to take measurements on those circuits.

The DSPSL equal and unequal power dividers presented in this dissertation were mainly designed for equal-phase linearly combined antenna arrays, as demonstrated with the DSPSL-fed 4x4 array. However, if the DSPSL dividers were needed for an application requiring high isolation between the dividers' output ports, then 100 Ω resistors could be soldered between the dividers' arms to increase the isolation between the output ports.

With the design of the DSPSL-fed radial dipole also came the two-dimensional DSPSL-fed radial dipole array. The dipole was designed to fit inside of the space limitations provided by the 4x4 array with 3 GHz half-wavelength spacing while providing the maximal bandwidth possible. The radial dipole was expected to have a larger bandwidth than was actually realized, but perhaps the bandwidth of the antenna was limited by the 90° bend used to feed the antenna.

The DSPSL-fed 4x4 radial dipole array demonstrated the new coaxial-to-DSPSL transition as well as both the equal and unequal power dividers. The array also proved that the two-dimensional SLL of the DSPSL-fed array could be improved by using a heavier weighting in the plane containing the dipoles' omni-directional patterns. As

an unexpected result of using several weighting schemes, the impedance bandwidth of the array was found to be the best for the mixed power weighting scheme that also provided the lowest SLL. Unfortunately, the SLL only remains low at 3.05 GHz, so an application utilizing the low SLL of this array cannot simultaneously utilize the array's 2:1 VSWR bandwidth.

REFERENCES

[1] J. Dyson, "The equiangular spiral antenna," *IRE Trans. Antennas and Propagat.*, vol. 7, no. 2, pp. 181-187, Apr. 1959.

[2] D. W. Smith and P. E. Mayes, "Spiral antennas over a ground plane," in *IEEE AP-S Int. Symp.*, vol. 4, Chicago, IL, Jul. 1992, pp. 2093-2096.

[3] G. H. Huff and T. L. Roach, "Stripline-based spiral antennas with integrated feed structure, impedance transformer, and dyson-style balun," in *IEEE AP-S Int. Symp.*, Honolulu, HI, Jun. 2007, pp. 2698-2701.

[4] W. Z. Wu, T. H. Chang, and J. F. Kiang, "Broadband slot spiral antenna with external feed and microstrip-to-slotline transition," in *IEEE AP-S Int. Symp.*, vol. 1, Monterery, CA, Jun. 2004, pp. 767-770.

[5] H. Nakano, Y. Shinma, and J. Yamauchi, "A monofilar spiral antenna and its array above a ground planeformation of a circularly polarized tilted fan beam," *IEEE Trans. Antennas and Propagat.*, vol. 45, no. 10, pp. 1506-1511, Oct. 1997.

[6] S. Zhaohui, L. Meijia, and D. Zhiyong, "An improved design of microstrip Archimedean spiral antenna," in *Int. Conf. on Microwave and Millimeter Wave Tech.*, pp. 1-4, Apr. 2007.

[7] W. H. Tu, M. Y. Li, and K. Chang, "Broadband microstrip-coplanar stripline-fed circularly polarized spiral antenna," in *IEEE AP-S Int. Symp.*, Albuquerque, NM, Jul. 2006, pp. 3669-3672.

[8] S. G. Kim and K. Chang, "Ultrawide-band transitions and new microwave compo-

nents using double-sided parallel-strip lines," *IEEE Trans. Microwave Thry. and Tech.*, vol. 52, no. 9, pp. 2148-2152, Sep. 2004.

[9] C. L. Dolph, "A current distribution for broadside arrays which optimizes the relationship between beam width and side-lobe level," in *Proc. IRE*, vol. 34, no. 6, pp. 335-348, Jun. 1946.

[10] A. N. Payne, "Improved bandwidth and efficiency of short antennas by the use of radials," *HF Radio Sys. Tech.*, no. 493, pp. 210-215, Jun. 2003.

[11] N. Li, J. Huang, Q. Hao, and Z. Feng, "A parallel strip line center-probe fed dipole," in *Asia-Pacific Conf. Proc.*, vol. 4, Suzhou, China, Dec. 2005, pp. 4-7.

[12] N. Li, W. Chen, and Z. Feng, "A switched sector beam planar antenna," in *IEEE AP-S Int. Symp.*, vol. 1A, Washington, D.C., Jul. 2005, pp. 230-233.

[13] C. A. Balanis, *Antenna Theory: Analysis and Design, Third Edition.* Hoboken, NJ: John Wiley & Sons, Inc., 2005, pp. 986-987.

[14] Y. Bahçeci and T. M. Duman, "Combined turbo coding and unitary space-time modulation," *IEEE Trans. Commun.*, vol. 50, no. 8, pp. 1244-1249, Aug. 2002.

[15] Y. Bahçeci, "Trellis- and turbo-coded modulation for multiple antennas over fading channels," MS Thesis, Arizona State University, Aug. 2001.

[16] D. H. Johnson and D. E. Dudgeon, *Array Signal Processing: Concepts and Techniques.* Englewood Cliffs, NJ: Prentice Hall PTR, 1993.

[17] G. Quintero, J. F. Zürcher, A. Skrivervik, "Omnidirectional pulse dispersion of planar circular monopoles," in *IEEE Int. Conf. Ultra-Wideband*,Vancouver, Canada, Sep. 2009, pp. 395-399.

[18] G. Quintero, J. F. Zürcher, A. Skrivervik, "Impact of substrate permittivity on the performance of UWB monopoles," in *3rd Eur. Conf. Ant. Propagat.*, Berlin, Germany, Mar. 2009, pp. 2567-2570.

[19] A. M. Abbosh and M. E. Bialkowski, "Design of UWB planar antenna for microwave imaging systems," in *IEEE Int. Conf. Sig. Process. Comm.*, Dubai, UAE, Nov. 2007, pp. 193-196.

[20] A. M. Abbosh and M. E. Bialkowski, "Design of ultrawideband planar monopole antennas of circular and elliptical shape," *IEEE Trans. Ant. Propagat.*, vol. 56, no. 1, pp.17-23, Jan. 2008.

[21] B. Sanz-Izquierdo, J. C. Batchelor, and M. I. Sobhy, "Compact UWB wearable antenna," in *Loughborough Ant. Propagat. Conf.*, Loughborough, UK, Apr. 2007, pp. 121-124.

[22] W. L. Stutzman and G. A. Thiele, *Antenna Theory and Design*, New York, NY: John Wiley & Sons, Inc., 2nd ed., p. 78, p. 90, pp. 117-118, pp. 251-253, 1998.

[23] D. M. Pozar, *Microwave Engineering*, New York, NY: John Wiley & Sons, Inc., 3rd ed., pp. 244-263, 2005.

[24] H. A. Wheeler, "Transmission-line properties of parallel strips separated by a dielectric sheet," *IEEE Trans. Microwave Thry. and Tech.*, vol. 13, no. 2, pp. 172-185, Mar. 1965.

[25] S.-W. Qu, J.-L. Li, Q. Xue, and C.-H. Chan, "Wideband periodic endfire antenna with bowtie dipoles," *IEEE Ant. Wireless Propagat. Lett.*, vol. 7, pp. 314-317, 2008.

[26] P. L. Carro, R. Gracia, and J. de Mingo, "Parallel-strip-fed antenna designs in ultrawideband applications," in *IEEE Ant. Propagat. Int. Symp.*, Honolulu, HI, Jun. 2007, pp. 1977-1980.

[27] R. King, "Linear arrays: currents, impedances, and fields, I," *IRE Trans. Ant. Propagat.*, vol. 7, no. 5, pp. 440-457, Dec. 1959.

[28] K. Chang, *RF and Microwave Wireless Systems*. New York, NY: John Wiley & Sons, Inc., p. 78, 2000.

[29] J. Volakis and J. Young, "Phase linearization of a broad-band antenna response in time domain," *IEEE Trans. Antennas and Propagat.*, vol. 30, no. 2, pp. 309-313, Mar. 1982.

[30] Aidin Mehdipour, Karim Mohammadpour-Aghdam, M. R. Kashani-Khatib, and Reza Faraji-Dana, "A practical feeder for differential elliptical antennas in ultra wideband applications," *Microwave Opt. Tech. Lett.*, vol. 50, no. 8, pp. 2103-2107, May 2008.

[31] L. Akhoondzadeh-Asl, M. Fardis, A. Abolghasemi, and G. Dadashzadeh, "Frequency and time doman characteristic of a novel notch frequency UWB antenna," *Prog. Electromag. Rsrch., PIER 80*, pp. 337-348, 2008.

[32] B. Ahmadi, "A planar eye shape antenna for ultra-wide band applications," *Prog. Electromag. Rsrch. Lett.*, vol. 11, pp. 31-38, 2009.

[33] D.-H. Kwon, "Effect of antenna gain and group delay variations on pulse-preserving capabilities of ultrawideband antennas," *IEEE Trans. Ant. Propagat.*, vol. 54, no. 8, pp. 2208-2215, Aug. 2006.

[34] D. Lamensdorf and L. Susman, "Baseband-pulse-antenna techniques," *IEEE Ant. Propagat. Mag.*, vol. 36, no. 1, pp. 20-30, Feb. 1994.

[35] S. W. Wong and L. Zhu, "Ultra-wideband power dividers with good isolation and sharp roll-off skirt," in *Asia-Pacific Microwave Conf.*, Hong Kong, China, Dec. 2008, pp. 1-4.

[36] J.-S. Lim et al, "A 4 : 1 unequal wilkinson power divider," *IEEE Microwave and Wireless Comp. Lett.*, vol. 11, no. 3, pp. 124-126, Mar. 2001.

[37] M. Karlsson, J. Östh, A. Serban, and S. Gong, "Circular dipole antennas for lower and upper UWB bands with integrated balun," in *ICUWB*, Vancouver, Canada, Sep. 2009, pp. 658-663.

[38] X. N. Low, Z. N. Chen, and T. S. P. See, "A UWB dipole antenna with enhanced impedance and gain performance," *IEEE Trans. Ant. Propagat.*, vol. 57, no. 10, pp. 2959-2966, Oct. 2009.

[39] G. A. Evtioushkine, J. W. Kim, and K. S. Han, "Very wideband printed dipole antenna array," *Elect. Lett.*, vol. 34, no. 24, pp. 2292-2293, Nov. 1998.

[40] F. Merli, J.-F. Zürcher, A. Freni, and A. K. Skrivervik, "Analysis, design and realization of a novel directive ultrawideband antenna," *IEEE Trans. Ant. Propagat.*, vol. 57, no. 11, pp. 3458-3466, Nov. 2009.

[41] A. Hees and J. Detlefsen, "Ultra broadband dual polarized dipole array with metallic reflector," in *ICUWB*, pp. 744-747, Sep. 2009.

[42] C. Yu, W. Hong, and Z. Kuai, "Multiple stopbands ultra wide band antenna," *Int. Conf. Microwave Millimeter Wave Tech.*, vol. 4, Nanjing, China, Apr. 2008, pp. 1872-1874.

[43] K. Chawanonphithak, C. Phongcharoenpanich, S. Kosulvit, and M. Krairiksh, "5.8 GHz notched UWB bidirectional elliptical ring antenna excited by circular monopole with curved slot," in *Asia-Pacific Microwave Conf.*, Bangkok, Thailand, Dec. 2007, pp. 1-4.

[44] Z. Ihsan and K. Solbach, "Ultra-wideband printed circular monopole antenna array," in *Eur. Radar Conf.*, Rome, Italy, Oct. 2009, pp. 377-380.

APPENDIX A

MATLAB CODE USED

********SpiralDraw.m********

```
% Written By: Travis Eubanks
% This program draws the equiangular spiral's
% outer boundaries.

clear all;

A = 0.5;
R0 = 0.2;
barHeight = 5;
barThickness = 5;
spiralRadius = 22.262;
subsThickness = 0.508;
subsX = 30;
subsY = 30;
subtractor = 0.0147;
tHole1 = 1.4575*pi;
tHole2 = 2.489*pi;
taperThickness = 0.7;
w = 0.2;
```

```
t = 0:3*pi/100:3*pi;

for j = 1:101,

        %Curve 1:
        x1(j) = R0*exp(A*t(j))*cos(t(j));
        y1(j) = R0*exp(A*t(j))*sin(t(j));
        z1(j) = 0;
        %Curve 2:
        x2(j) = (R0+w-subtractor*t(j))*exp(A*t(j))*cos(t(j));
        y2(j) = (R0+w-subtractor*t(j))*exp(A*t(j))*sin(t(j));

        %Curve 3:
        x3(j) = R0*exp(A*t(j))*(-cos(t(j)));
        y3(j) = R0*exp(A*t(j))*(-sin(t(j)));
        %Curve 4:
        x4(j) = (R0+w-subtractor*t(j))*exp(A*t(j))*(-cos(t(j)));
        y4(j) = (R0+w-subtractor*t(j))*exp(A*t(j))*(-sin(t(j)));

end

plot3(x1,y1,z1, 'black', x2,y2,z1, 'black', x3,y3,z1, 'black', x4,y4,z1, 'black' )
view([0,90]);

%Coupling Hole 1:
```

```
%Radius = ((R0*exp(A*tHole1)*sin(tHole1))-(R0+w-subtractor*tHole1)
          %*exp(A*tHole1)*sin(tHole1))/holeDivider

%Xcenter = -R0-w/2
%Ycenter = ((R0*exp(A*tHole1)*sin(tHole1))+(R0+w-subtractor*tHole1)
           %*exp(A*tHole1)*sin(tHole1))/2
%Coupling Hole 2:

%Radius = (R0*exp(A*tHole2)*-sin(tHole2)-(R0+w-subtractor*tHole2)
          %*exp(A*tHole2)*-sin(tHole2))/holeDivider

%Xcenter = -R0-w/2
%Ycenter = (R0*exp(A*tHole2)*-sin(tHole2)+(R0+w-subtractor*tHole2)
           %*exp(A*tHole2)*-sin(tHole2))/2

x1 = x1';
x2 = x2';
x3 = x3';
x4 = x4';
y1 = y1';
y2 = y2';
y3 = y3';
y4 = y4';
```

```
csvwrite('travisX1.xls', x1);
csvwrite('travisX2.xls', x2);
csvwrite('travisX3.xls', x3);
csvwrite('travisX4.xls', x4);
csvwrite('travisY1.xls', y1);
csvwrite('travisY2.xls', y2);
csvwrite('travisY3.xls', y3);
csvwrite('travisY4.xls', y4);
```

********ZandGamma.m********

```
%Written By: Travis Eubanks
%This program finds the characteristic impedance vs. distance and
%the reflection coefficient vs. frequency for a tapered
%parallel-strip transmission line. The taper on the line
%is governed by this equation
%
%w = 0.2+0.0482*y
%
%where w is the line width and y is the length of the line from
%the origin. This line extends 30 mm.

clear all;

er = 2.2; %relative dielectric permittivity
```

```
h = 0.508; %substrate height (m)
%From Wheeler's Paper
Hp = (er+1)/2 + 1/2*(er-1)/(er+1)*(log(pi/2)+1/er*log(4/pi));
%effective dielectric permittivity
ef = (er+1)/2+(er-1)/(2*Hp)*(log(pi/2)+1/er*log(4/pi));
c = 3e8;
sCount = 200; % # of points for space index
fCount = 200; % # of points for frequency index
fstart = 1e9;

f = fstart:(20e9-fstart)/(fCount-1):20e9; % 'count' # of frequency points
B = (2*pi*f/c)/1000; % B in mmˆ-1
y = 0:30/(sCount-1):30; % y in mm

for k = 1:sCount % space index
    %Narrow Parallel-Strip
    %Zn(k) = 377/(sqrt((er+1)/2))*1/pi*(log(4*h/(0.2+(0.0487)*y(k)))
    %+1/8*((0.2+(0.0487)*y(k))/h)ˆ2-1/2*(er-1)/(er+1)*(log(pi/2)
    %+1/er*log(4/pi)));

% The transition region between narrow and wide parallel-strips
% happens at approximately width/height = 0.5 according to Wheeler.
% For the transmission line in this example the cross-over point
% does not occur at all (as seen by the plots of the characteristic
% impedances) for 0.39 ≤ w/h ≤ 3.27.
```

```
    %Wide Parallel-Strip
    Zw(k) = 377*sqrt(1/er)/((0.2+(0.0487)*y(k))/h+0.441
    +(er+1)/(2*pi*er)*(log((0.2+(0.0487)*y(k))/h+0.94)
    +1.451)+(er-1)/(erˆ2)*0.082);
end

%Numerical derivatives of the characteristic impedance arrays
%temp = gradient(Zn,(30/(sCount-1))*1000);
temp2 = gradient(Zw,(30/(sCount-1))*1000);

%Intermediate functions to prepare for integration
for q = 1:fCount %frequency index
    for k = 1:sCount %space index
        %fn(k,q) = temp(k)*exp(-2i*B(q)*y(k));
        fw(k,q) = temp2(k)*exp(-2i*B(q)*y(k));
end

%Integrate over length of parallel-strip transformer (0 to 30 mm)
%Gn(q) = abs(1/2*trapz(y,fn(1:count,q)));
Gw(q) = abs(1/2*trapz(y,fw(1:sCount,q)));
end

plot(y,Zw)
pause
```

```
plot(f,Gw)

% write matrices to save into the matlab/work directory
csvwrite('PStripZo.dat',Zw')
csvwrite('PStripGamma.dat',Gw')
```

********centeredFFT.m********

```
function [X,freq]=centeredFFT(x,Fs)
%this is a custom function that helps in plotting the two-sided spectrum
%x is the signal that is to be transformed
%Fs is the sampling rate

N=length(x);

%this part of the code generates that frequency axis
if mod(N,2)==0
   k=-N/2:N/2-1; % N even
else
   k=-(N-1)/2:(N-1)/2; % N odd
end

T=N/Fs;
freq=k/T; %the frequency axis
```

```
%takes the fft of the signal, and adjusts the amplitude accordingly
X=fft(x);
X=X/max(X); %normalize the data
X=fftshift(X); %shifts the fft data so that it is centered
```

********Fidelity.m********

```
%Fidelity Factor Calculations
%By Travis Eubanks

clear all;

Time = csvread('PPPcSpiralTime.csv'); %time steps
Pulse = csvread('PPPcSpiralPulse.csv'); %Pulse covering 3-12 GHz
Response = csvread('PPPcSpiralResponse.csv'); %output from PPPC fed spiral

%normalize Response for a better looking plot

Response = Response/(max(Response));
Response = Response/(abs(min(Response)));

plot(Time/1e-9, Pulse, 'k', Time/1e-9, Response, '-.k')
xlabel('Time (ns)')
ylabel('Arb. Units')
```

```
legend('Pulse', 'Response')
title('Travis" Spiral Pulse and Response in Time')
axis([0, 2, -1, 1])

St = sqrt(trapz(Time, abs(Pulse).^2));
Sr = sqrt(trapz(Time, abs(Response).^2));

FF = conv(Pulse,Response)*Time(2)/(Sr*St);

FidelityFactor = max(FF)

pause

% Fourier Transform the pulse and response to compare their results

Fs = 1/Time(2); %sampling frequency defined by time interval

[PulseSpectra, Freq]=centeredFFT(Pulse, Fs);
[ResponseSpectra, Freq] = centeredFFT(Response, Fs);
plot(Freq/1e9, abs(PulseSpectra), 'k', Freq/1e9, abs(ResponseSpectra), '-.k')
xlabel('Freq (GHz)')
ylabel('Amplitude')
title('Travis" Spiral Impulse and Response Spectra')
legend('Pulse', 'Response')
axis([1,15,0,1])
```

```
pause

%Narrow-band Pulse and Response
Time = csvread('NarrowBWtime.csv'); %time steps
Pulse = csvread('NarrowBWin.csv'); %Pulse covering 5.95-6.05 GHz
Response = csvread('NarrowBWout.csv'); %output from PPPC fed spiral

%normalize Response for a better looking plot

%Response = Response/(max(Response));
%Response = Response/(abs(min(Response)));

plot(Time/1e-9, Pulse, 'k', Time/1e-9, Response, '-.k')
xlabel('Time (ns)')
ylabel('Arb. Units')
legend('Pulse', 'Response')
title('Travis" Spiral Pulse and Response in Time')
axis([0, 70, -1, 1])

St = sqrt(trapz(Time, abs(Pulse).^2));
Sr = sqrt(trapz(Time, abs(Response).^2));

FF = conv(Pulse,Response)*Time(2)/(Sr*St);
```

```
FidelityFactor = max(FF);

pause

% Fourier Transform the pulse and response to compare their results

Fs 1/Time(2); %sampling frequency defined by time interval

[PulseSpectra, Freq]=centeredFFT(Pulse, Fs);
[ResponseSpectra, Freq] = centeredFFT(Response, Fs);
plot(Freq/1e9, abs(PulseSpectra), 'k', Freq/1e9, abs(ResponseSpectra), '-.k')
xlabel('Freq (GHz)')
ylabel('Amplitude')
title('Travis" Spiral Impulse and Response Spectra')
legend('Pulse', 'Response')
axis([1,15,0,1])
```

VITA

Travis Wayne Eubanks received the B.S. and Ph.D. degrees from Texas A&M University, College Station, Texas in 2007 and 2010, respectively. His research interests include wireless power, ultra-wideband communications, and electrically small tracking devices.

Dr. Eubanks may be reached at the Department of Electrical and Computer Engineering, Texas A&M University, 214 Zachry Engineering Center, TAMU 3128, College Station, Texas 77843-3128. His e-mail is travis.eubanks@gmail.com.

The typist for this dissertation was Travis Wayne Eubanks.